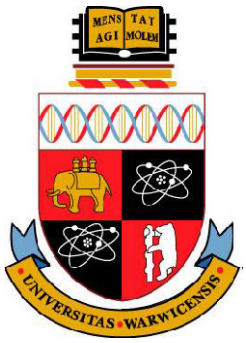

New Methods for the study of Physicochemical Processes Relevant to the Agrochemicals Industry

By Michael Alexander O'Connell

A thesis submitted for the degree of Doctor of Philosophy

Department of Chemistry

University of Warwick

September 2012

Table of Contents

List of Figures

List of Tables

Acknowledgements

Firstly, I would like to thank my supervisor Prof. Pat Unwin and also Prof. Julie Macpherson and Dr Ian Shirley of Syngenta for direction, support and advice throughout. I would also like to thank all members of the Electrochemistry and Interfaces group past and present and further collaborators at Warwick and Syngenta. Finally, I would like to thank everyone at Warwick and beyond who has helped to make life as a PhD student more entertaining and enjoyable.

Declaration

The work contained within this thesis is original and my own except where outlined below. I confirm that this thesis has not been submitted for any degree at another university.

The supported lipid bilayer experiments in Chapter 3 were performed in collaboration with Dr Hayley Powell, the modelling in Chapter 4 was carried out in conjunction with Dr Michael Snowden, based upon his existing model, and the SICM experiments in Chapter 5 were performed in collaboration with Mr Marc Baghdadi

Parts of this thesis have been published or submitted for publication as detailed below:

O'Connell, M. A.; de Cuendias, A.; Gayet, F.; Shirley, I. M.; Mackenzie, S. R.; Haddleton, D. M.; Unwin, P. R., Evanescent Wave Cavity Ring-Down Spectroscopy (EW-CRDS) as a Probe of Macromolecule Adsorption Kinetics at Functionalized Interfaces. *Langmuir* **2012,** *28* (17), 6902-6910;

Powell, H. V.; O'Connell, M. A.; Zhang, M.; Mackenzie, S. R.; Unwin, P. R., Evanescent Wave Cavity Ringdown Spectroscopy (EW-CRDS): A Platform for the Study of Supported Lipid Bilayers. *Analytical Chemistry* **2012**.

O'Connell, M. A.; Snowden, M. E.; Unwin, P. R., A Simple Vertical Microfluidic Cell based upon Migration in a Theta Capillary, *In preparation*

Baghdadi, M.; O'Connell, M. A.; McKelvey, K.; Snowden, M. E.; Unwin, P. R., Measurement of ion fluxes from plant cells via scanning ion conductance microscopy (SICM), *In preparation*

Abbreviations

AC	Alternating Current
AFM	Atomic Force Microscopy
ATR	Attenuated Total Internal Reflection Spectroscopy
CLSM	Confocal Laser Scanning Microscopy
CRDS	Cavity Ring-Down Spectroscopy
DC	Direct Current
DOTAP	1,2-dioleoyl-3-trimethylammonium-propane
EC-SPM	Electrochemical Scanned Probe Microscopy
EW-CRDS	Evanescent Wave Cavity Ring-Down Spectroscopy
FRAP	Fluorescent Recovery After Photobleaching
FRET	Fluorescent Resonance Energy Transfer
IC-SECM	Intermittent Contact - Scanning Electrochemical Microscopy
PGA	Poly-L-Glutamic Acid
PLL	Poly-L-Lysine
PMT	Photomultiplier Tube
QCM-D	Quartz Crystal Microbalance with Dissipation
SECM	Scanning Electrochemical Microscopy
SECCM	Scanning Electrochemical Cell Microscopy
SICM	Scanning Ion Conductance Microscopy
SHG	Second Harmonic Generation
SPM	Scanned Probe Microscopy

SPR	Surface Plasmon resonance
SLB	Supported Lipid Bilayer
SUV	Small Unilamellar Vesicles
TIR	Total internal reflection
TM-AFM	Tapping mode atomic force microscopy
TPPS	5,10,15,20-Tetraphenyl-21H, 23H-porphine-p,p′,p″,p‴-tetrasulfonic acid
UME	Ultra Micro Electrode

Glossary of Symbols

a	electrode radius
A	optical absorbance
A_s	sensor area
c	speed of light
C	concentration
c_j	concentration of species j
D	diffusion coefficient
d	pipette diameter
d_p	penetration depth
δ	diffusion layer thickness
E	potential
ε_0	dielectric constant
ε_r	permittivity of free space
f	frequency
f_0	resonant frequency
F	Faraday's constant
λ	wavelength
h_p	tip-sample separation (height)
η	dynamic viscosity
j	flux
k	kinetic rate constant
k_B	Boltzmann constant

k_i	initial rate constant
k_D	diffusional rate constant
k_T	mass transport rate constant
κ^{-1}	Debye length
L	cavity length
m	mass
μ_q	shear modulus of quartz
n	refractive index
ρ_q	density of quartz
r	radius
R	gas constant
Re	Reynold's number
Sc	Schmidt number
Sh	Sherwood number
θ_c	critical angle
τ_0	background ring-down time
τ	ring-down time
Θ	capillary semi angle
t	central segment thickness
T	absolute temperature
υ	kinematic viscosity

Abstract

This thesis concerns the application of modern analytical techniques for the study of a range of systems relevant to the agrochemicals industry, with a focus on adapting and further developing these technologies to the systems of study. The major systems involved include the study of bioadhesion relevant to plant root cells and their local environment, and the further study of the root cell surface.

Evanescent wave cavity ring-down spectroscopy (EW-CRDS) is the first major technique employed. For these studies a range of mimetic surfaces are designed to represent the plant cell surface and soil environment. These studies are then used to study various chemical functionalities, in the form of functional groups on polymer molecules, for adsorption properties on such surfaces. Kinetic information on the adsorption rates is measured in the form of initial rate constants. These studies are the extended to examine the cell membrane via the use of supported lipid bilayer (SLB) membranes by the combination with an impinging jet flow cell.

Confocal laser scanning microscopy (CLSM) is then used to measure microparticle adsorption rates to functionalised surfaces. These studies then employ two different delivery systems, resulting in the development of a microscale vertical flow cell on the scale of individual plant cells. Understanding of the characteristics of this flow system are enhanced by the use of finite element modelling to examine the movement of the particles and flow rates.

Finally, a range of electrochemical scanned probe microscopy (EC-SPM) techniques are used to study the root cell surface and local environment, with a focus on assessment of each for such applications. Scanning ion conductance microscopy (SICM) is found to be the most applicable and initial work on flux imaging is performed.

Chapter 1. Introduction

This thesis concerns the application and further development of modern analytical chemical techniques to study processes relevant to the agrochemical industry, *i.e.* for physical and chemical processes involving plants and their environments. A particular focus is that of bioadhesion; measurement of rates of binding of species to plant matter, including those in competition with the local (soil) environment. In the context of this project, one major driver is the principle of 'targeted delivery', *i.e.* the design of a delivery system that is mobile through the local environment but binds to the biological matter, in this case the root system of the *Zea mays* plant. To such ends, model systems are developed and combined with modern analytical techniques to study relevant materials through the use of biomimetics. This is later expanded to include biological samples and their structure and activity is probed further. The range of techniques used encompasses evanescent wave cavity ring-down spectroscopy (EW-CRDS) to study relatively fast adsorption kinetics of functionalised macromolecules to a range of soil and cellular mimetic surfaces, confocal laser scanning microscopy (CLSM) techniques coupled with novel delivery systems to probe microparticle adsorption rates to mimetic and biological samples, followed by thorough investigation of root cell surface structure and activity via novel electrochemical scanned probe microscopy (EC-SPM) techniques.

1.1 Plant root systems and their local environments

When examining processes relevant to plant root systems, two large areas of scientific study must be taken into account, those of plant biology and soil science, and also the exchange between the two environments. Biological adhesion in the combined environment is an important aspect of this project, and an understanding of it is vital in designing model systems to study adsorption rates using physicochemical analytical techniques. As such, brief discussion of the major components of the plant and soil environment is included.

The targeting of systems to adhere to the root but not soil environment is clearly not trivial; one must create a carrier system to both move an 'active ingredient', referred to as an AI, to the root surface and adhere once it reaches it. One can simplify the study of this by examining individual components separately; Figure 1.1 shows a schematic of the entire system incorporating the delivery system with encapsulated AI within a polymer particle and soil mobile/root adhesive modifier.

The modifier can be simply a surface functionality or further chemically-grafted molecules. For this, polymeric molecules are particularly useful due to the repeat units exhibiting multiple functional groups, thus enhancing the effect of changing chemistry. Also, the physical length of these molecules is beneficial, as the chains are generally flexible allowing the polymer molecule to orient itself on a surface, thus creating a 'hairy' particle.

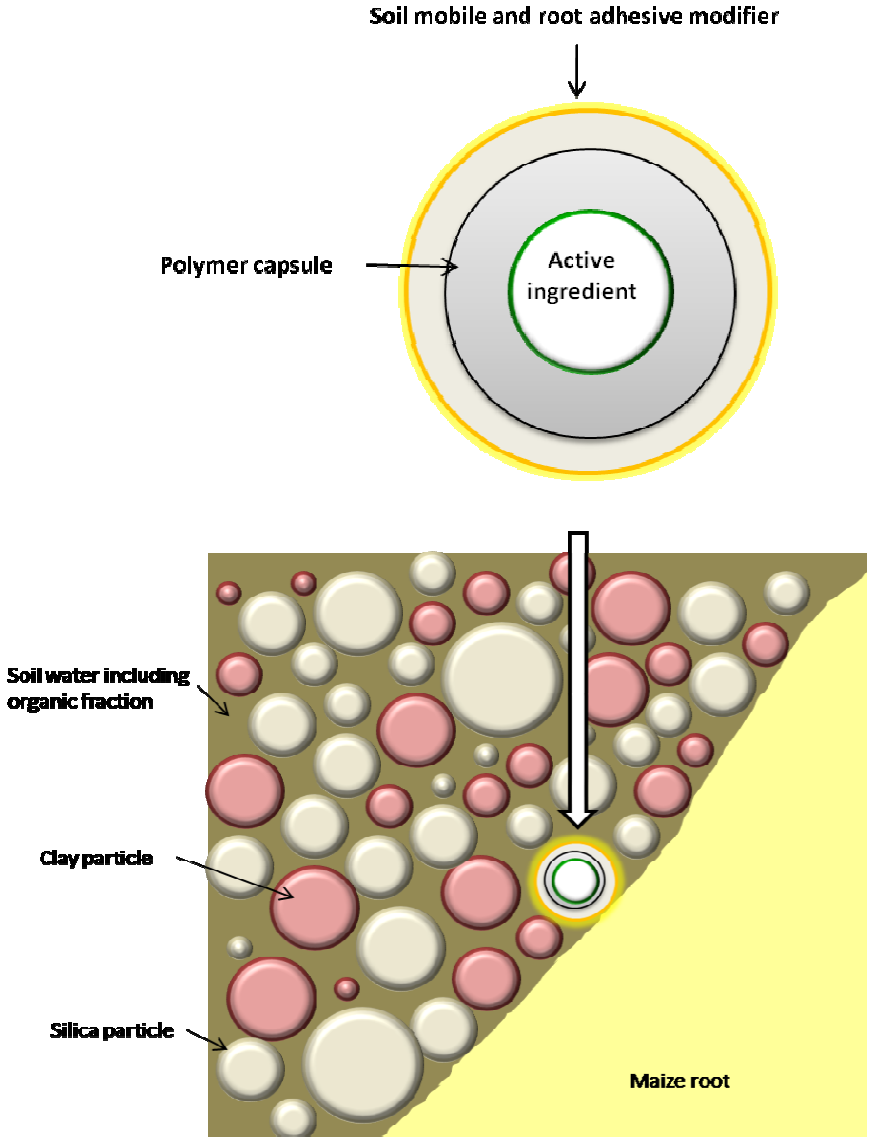

Figure 1.1. Schematic of the targeted delivery system and the soil/root environment. A carrier particle is designed to encapsulate an active ingredient and is modified to enhance soil mobility and root adhesion. This particle must be able to travel through the soil system, comprised of sand and clay particles, as well as soil water containing humic and fulvic acids.

The soil itself is a complex mixture of components which can be grouped into inorganic and organic fractions.[1] The composition of a particular soil varies

greatly but inorganic fractions are grouped - according to size; with sand being between 2 mm and 50 µm, silt being 50 µm and 2 µm and clay being less than 2 µm.[2] The chemical composition of this fraction is a combination of silica and metal oxide silicates, such as alumina silicates, magnesium oxide silicates and iron oxide silicates[3]. Proportions and crystal structures of each vary with soil type. The organic fraction is made up of humic and fulvic acids[4], complex mixtures of aromatic and aliphatic carboxylic acids, as well as decaying plant matter. The organic acids are generally dissolved in the soil water fraction, along with a variety of other ions.

1.1.1 Plant and root cell structure

The plant root itself is a complex organ comprising of a variety of cell types. Figure 1.2 shows a simplified schematic of the whole root system. The cell types of particular interest are those on the outer surface, associated mainly with biological adhesion and the uptake of nutrients from the soil, which are the root hair and root cap cells. These are specialised cell types; the root cap is the main growth area whereas the root hair cell system comprises of a large number of long, thin hair-like cells which provide a large surface area for uptake and adhesion.

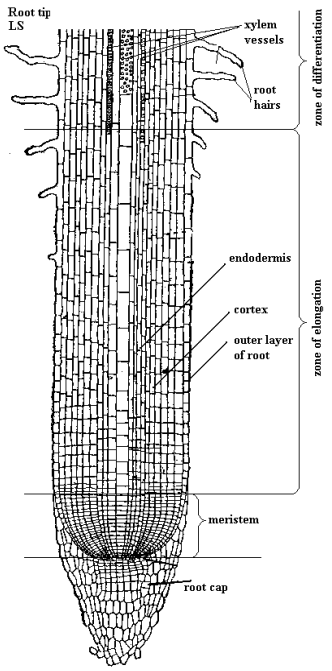

Figure 1.2. Simplified cellular diagram of a plant root.[5] The sites of particular interest here are the specialised root cells on the outer surface of the root. The two main types are the root cap cell, the site of new growth, and the root hair cell, the site of highest uptake and representing the majority of the surface area of the root.

The plant cell itself has many similarities to animal cells but contains a number of extra features. In common with most cells, plant cells have a lipid bilayer cell membrane and contain basic features such as a cytoplasm, nucleus and various organelles. However, additional features give the plant cells their structure; these are an internal sap-filled vacuole and, vital for the studies herein, the outer cell wall which surrounds the cell membrane and is in direct contact with the external environment. This is comprised primarily of cellulose, a polymer of β- linked D-glucose (see Figure 1.3), as well as other carbohydrates

(mainly hemicelluloses and pectin) and small amounts of glycoproteins.[5] (See Figure 1.4)

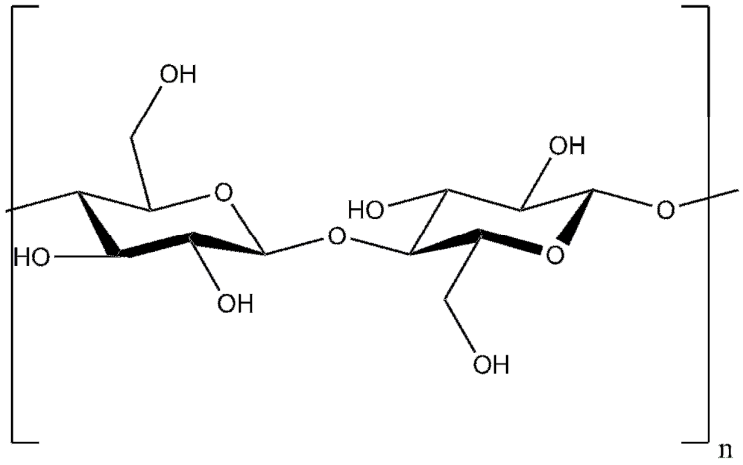

Figure 1.3. The structure of cellulose.

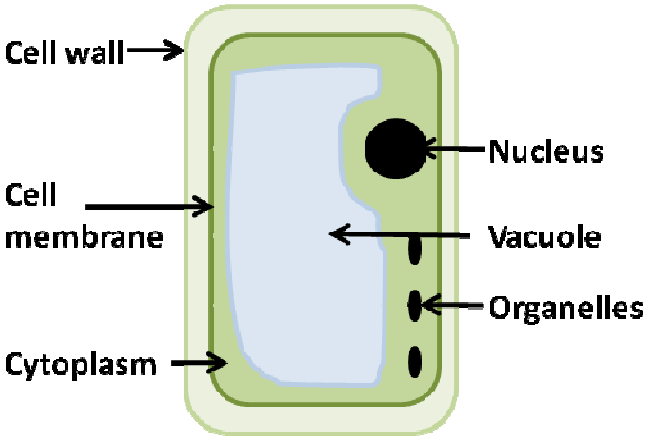

Figure 1.4. A simplified cartoon of a typical plant cell. The cell shares several components with all cells (*eg* cell membrane, cytoplasm, nucleus) but also has plant cell-specific features, *ie* the vacuole and, importantly, the cellulosic cell wall.

As mentioned above, the root hair cells (see Figure 1.5) are vital to uptake and adhesion functions of the plant root, largely due to their geometry. Despite being only ~ 10 µm in diameter, they can extend to mm length scales; this structure allowing a dense packing and a huge increase in the surface area exposed to the soil environment. The surface of these cells is, therefore a major area of study in this thesis.

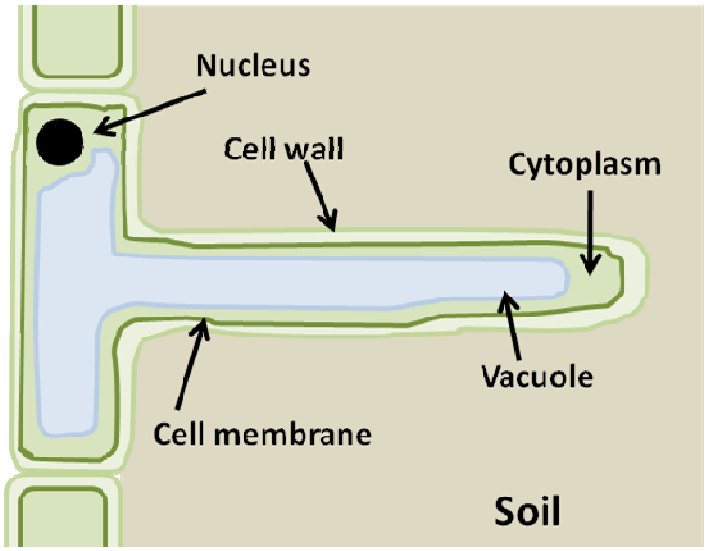

Figure 1.5. A simplified cartoon of a typical root hair cell. This type of cell exhibits a protruding hair into the plants immediate environment and can extend up to a few millimetres. These provide the principle uptake and adhesion surface of the plant root system.

1.2 Techniques for study of surface adsorption

A broad range of techniques are available for the study of surface adsorption which have various advantages and disadvantages with respect to sensitivity, temporal and spatial resolution, ease of data analysis and versatility. This section briefly examines some common techniques and discusses in more detail the evanescent wave-cavity ring-down spectroscopy technique employed to study reasonably fast adsorption kinetics to mimetic surfaces.

1.2.1 Commonly used surface adsorption techniques

The quartz crystal microbalance (QCM) technique works by measuring changes in resonant frequency with respect to changes in adsorbed mass. Though there are many variations[6] of the technique; a common set up entails a quartz crystal sensor sandwiched between two metal electrodes. The crystal is caused to oscillate at its resonant frequency by the application of an alternating electric field between the two electrodes. As the resonant frequency is affected by the mass of the crystal, any addition to this, in the form of surface adsorption, causes a change in resonant frequency. Typical mass sensitivities for commercial instruments are in the ng cm^{-2} range and can be calculated directly from the change in frequency using the Sauerbrey equation[7]

$$\Delta f = \frac{-2 f_0 \Delta m}{A\sqrt{\rho_q \mu_q}} \qquad (1.1)$$

where Δf is the change in resonant frequency, Δm is the adsorbed mass, f_0 is the resonant frequency of the sensor, A is the sensor area, ρ_q is the density of quartz and μ_q is the shear modulus of quartz.

This, however, assumes a perfectly rigid adsorbed layer which is clearly a limitation as many adsorbed layers are non-rigid. A common way is to measure extra properties, generally the dissipation (QCM-D). In practice, this involves switching off the alternating voltage and measuring the decay in oscillations. This, however, introduces the problem of employing more complicated viscoelastic models.[8-10]

A range of optical techniques can also be used. Ellipsometry is a particularly widely-used technique for measuring thin film thicknesses[11,12] and also for dynamic processes.[13] This technique employs polarised light beams reflected off a sample as a function of wavelength, with the change in polarisation monitored. Data obtained from these types of measurements also needs to be modelled which complicates analysis, and also requires well-defined, optically homogenous layers. A similar, but simpler, method is optical reflectometry,[14] as well as a range of other techniques such as second harmonic generation, sum frequency generation and Brewster angle reflectivity.[15-21]

A number of optical techniques employ the evanescent waves formed when light undergoes total internal reflection (TIR). This effect is particularly suited to measuring surface adsorption as the penetration depth of the evanescent field is only of the order of the wavelength of the electromagnetic radiation used, so for visible light that of hundreds of nm. TIR occurs when light incident on the

interface between two media of differing refractive indices exceeds a critical angle, defined by equation 1.2

$$\theta_c = \sin^{-1}\left(\frac{n_1}{n_2}\right) \tag{1.2}$$

where θ_c is the critical angle, and n_1 and n_2 are the refractive indices of the two media (shown schematically in Figure 1.6).

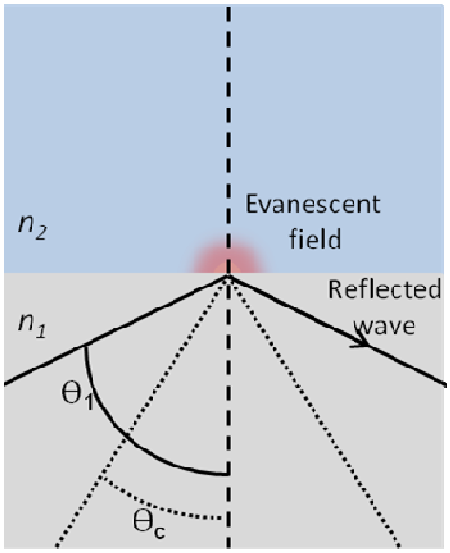

Figure 1.6. Schematic of the evanescent field produced when light undergoes total internal reflection (TIR). TIR occurs when the angle of incident light exceeds the critical angle, θ_c, of the interface between the two media. Incident light below this critical angle will be partially transmitted (refracted).

Incident light below this critical angle is refracted. TIR spectroscopy techniques then work in a similar manner to conventional absorbance spectroscopy, *i.e.* light absorbed from the evanescent field results in a decrease in intensity of measured (totally reflected) light and optical absorbance is calculated via the Beer-Lambert Law. As the reduction in light intensity by a surface-bound species from a single pass is likely very small, a number of methods exist to improve sensitivity. Of these, two are fairly common; attenuated total internal reflection spectroscopy (ATR)[22] employs multiple points of TIR, whereas surface plasmon resonance (SPR)[22-24] uses the excitation of surface plasmons in a thin metal film (generally a monolayer or nanoparticles of Au or Ag). In this case, transmitted light is more sensitive to the angle of incidence, as the SPR angle is dependent on the refractive index of the immediate environment of the metal film. One can either measure the reflectivity as a function of angle, or the reflectivity as a function of time, which can be related to absorbance.

1.2.2 Cavity ring-down spectroscopy

Cavity ring-down spectroscopy (CRDS), first developed by O'Keefe *et al*.[25] and originally used in the gas phase, has been extended to study many systems and is the subject of several reviews.[26-30] The use of an optical cavity (resonator) in absorption spectroscopy is advantageous, as the path length of the light is increased massively, which in turn greatly increases the sensitivity of the technique. The CRDS technique essentially floods the optical cavity with light until a plateau is reached, once the optical cavity is stable the light source is

extinguished and the exponential decay in light intensity (due to losses associated to the mirrors used) is measured. This decay is characterised by the background ring-down time, τ_0, ie the time taken for the light intensity to fall to e^{-1}. τ_0 is defined by losses in the system via equation 1.3

$$\tau_0 = \frac{L}{c(1-R)} \qquad (1.3)$$

where L is the cavity length, R relates to the mirror reflectivity and c is the speed of light. The addition of an absorbing species into the cavity will add to the total optical losses and result in a new ring-down time, τ. From this the optical absorbance, A, can be calculated by

$$A = \log_{10} e \frac{L}{c}\left[\frac{1}{\tau} - \frac{1}{\tau_0}\right] \qquad (1.4)$$

where the $\log_{10}(e)$ is a conversion factor to the conventional logarithmic scale used to define absorbance.

1.2.3 Evanescent wave-cavity ring-down spectroscopy (EW-CRDS)

The CRDS technique has been used to study the condensed phase using a number of different approaches. The solution has been placed directly inside the cavity in contact with the mirrors,[31,32] the mirrors have been coated with the species of interest[33] and a cell has been inserted at the Brewster angle.[34-36] However, the addition of a TIR element makes EW-CRDS a particularly useful

variant. First developed by Pipino *et al*.,[17] EW-CRDS is emerging as a key technique for the study of kinetic processes at solid-liquid interfaces.[18,19] EW-CRDS combines the high sensitivity which arises from the multiple passes within a high-finesse optical cavity, with the high spatial resolution resulting from evanescent fields.[20]

A number of cavity geometries are possible, as reviewed recently.[37] The studies herein use a ring cavity, essentially a simple configuration designed to use a broadband, single wavelength diode laser and anti-reflective coated mirrors. The broadband laser (bandwidth ~ 1 nm) excites multiple modes within the cavity, precluding the need to scan the cavity, which simpifies beam alignment. The need for an antireflective coating prevents any polarisation-dependent measurement, however the prisms used are readily available and relatively inexpensive. Where polariation-dependent measurements are required the folded-cavity variant of EW-CRDS is often used. These two important geometries are shown schematically in Figure 1.7.

The set up used for this project consists of a laser beam pulsed into an optical cavity incorporating a right-angled fused silica prism.[38] The point of TIR is formed on the top surface of the prism. If a cell is placed on top of this then a solution can be added allowing the interface between the prism surface and solution to be probed. Equipment required is fairly simple; a diode laser (generally at 405 nm), photomultiplier tube (PMT), commercially available mirrors, an anti-reflective coated right-angled silica prism, an oscilloscope and oscilloscope data acquisition card connected to a PC. This configuration has been

used for several studies[39-41] and the use of a right-angled fused silica prism has also been described by other groups.[42-44]

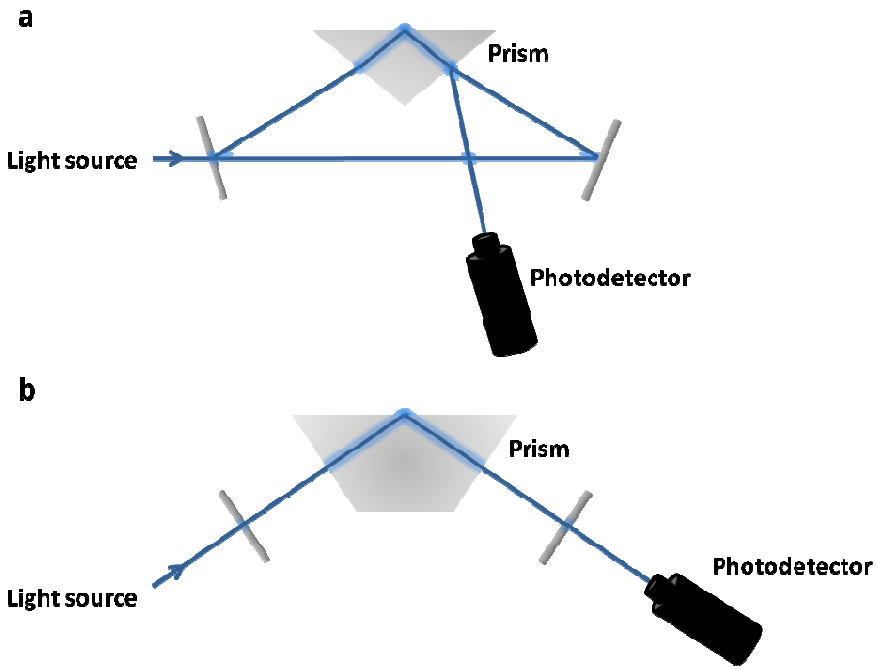

Figure 1.7. Two common cavity geometries. A) the ring cavity and b) the folded cavity. The ring cavity requires an antireflective coating on the prism. As the laser beam does not enter the prism perpendicular to prism surface, an antireflective coating is required, precluding employment in polarisation sensitive experiments. The folded cavity overcomes this at the cost of more complicated alignment and (generally) lower ringdown times.

With this method the calculation of surface adsorption from the absorbance is simple. The optical absorbance measured from equation 1.5 can be related to the surface concentration by equation 1.6 using the extinction coeffiecient of the absorbing species measured by UV-vis spectroscopy and calculated by the Beer-Lambert Law,

$$\Gamma = \frac{A}{\varepsilon} \tag{1.5}$$

$$A = \varepsilon c l \tag{1.6}$$

where Γ is the surface concentration, A is the optical absorbance, ε is the extinction coefficient (molar absorption coefficient), c is the concentration and l is the path length.

There is also some small absorbance due to optically absorbing species in bulk. In addition to studying the interface, the evanescent wave will also penetrate a short distance into the solution as described by equation 1.7,

$$d_p = \frac{\lambda}{2\pi\sqrt{n_1^2 \sin^2\theta - n_2^2}} \tag{1.7}$$

where d_p is the penetration depth, λ is the wavelength of the laser, n_1 and n_2 are the refractive indices of the prism and the solution and θ is the angle of incidence of light path with respect to the prism surface. Such bulk absorbances can, however, generally be removed as an instantaneous change in absorbance when solution is added.

Past studies have used a range of cavity geometries to monitor various processes at the solid/liquid interface including interactions of dye molecules with silica[45-47] and other organic molecules.[44,48] EW-CRDS and related techniques[49] are highly-sensitive tools for studying changes at interfaces with sufficiently fast temporal resolution to study reasonably fast kinetics as exemplified by a recent review of applications.[37]

Although applications at liquid/air interfaces have been reported,[37] most EW-CRDS studies to date have focused on silica surfaces; for example, Fan *et al.* used the adsorption of crystal violet cations to determine the relative populations of two different types of silanol groups at the silica surface.[50] Initial EW-CRDS studies focused on the adsorption of small molecules on silica, with exemplar investigations of crystal violet,[47] Nile blue,[46] methylene blue,[42] $[Ru(bpy)_3]^{2+}$ [40] and rhodamine B.[51] However, more recently, the technique has been applied to more diverse problems, such as electrochemically induced desorption kinetics of silver nanoparticles,[39] polyaniline nanoparticle formation and growth[52] and also bioanalytical applications.[53-55]

1.3 Optical microscopy techniques

In addition to spectroscopic techniques, microscopy can also be used to monitor surface adsorption of certain species, with the added benefit of the ability to visualise the nature of the adsorbed layer, though generally with lower sensitivity and temporal resolution. Multiple analytical techniques employ electromagnetic radiation as a means to image a surface, the simplest being visible light. Beyond basic light microscopy, fluorescent emission provides a highly useful tool, giving greater contrast compared to standard brightfield and darkfield techniques and is particularly favoured in the life sciences.

1.3.1 Fluorescent microscopy techniques

Fluorescent light techniques rely on fluorescently active materials, generally referred to as fluorophores, to provide a measurable light signal. One advantage of this is that different fluorophores are excited by, and emit, light at distinct wavelengths, related to the energy levels at the ground and excited electrionic states of the fluorophore. Control of both incident and measured wavelengths allow specific (and multiple) fluorophores to be monitored individually. A broad range of fluorescence-based techniques are routinely used such as fluorescent recovery after photobleaching (FRAP) to measure diffusion and fluorescent resonance energy transfer (FRET), lifetime and polarisation-dependent techniques to measure molecular properties.[56-59]

The simplest configuration is a widefield (epi)fluorescence mode, where a combination of dichroic mirrors and filters, coupled with an incoherent white light source, allow control of wavelength ranges for both excitation and emission, and light intensity can be measured using simple sensors such as charge coupled devices (CCDs), *i.e.* cameras. The drawbacks with this configuration are partly the lack of control over wavelength of light, but largely due to the large amounts of out of focus light measured, due to fluorescent emission above and below the focal plane. These drawbacks can be improved by coupling light from laser sources with confocal microscopy.

1.3.2 Confocal laser scanning microscopy (CLSM)

Confocal laser scanning microscopy (CLSM)[60-62] utilises laser excitation sources (commonly Argon ion and Helium Neon, amongst others), motor-controlled scanning mirrors and optical pinholes to construct three-dimensional fluorescence images through samples. A simplified configuration for a typical CLSM system is shown in Figure 1.8. Essentially, a pixel by pixel image is recorded and reconstructed by graphical software. The pinholes serve to ensure only light in the focal plane falls on the detector, which is generally a photomultiplier tube (PMT) due to the small intensities of light related to each pixel, giving a far sharper image than conventional widefield techniques.

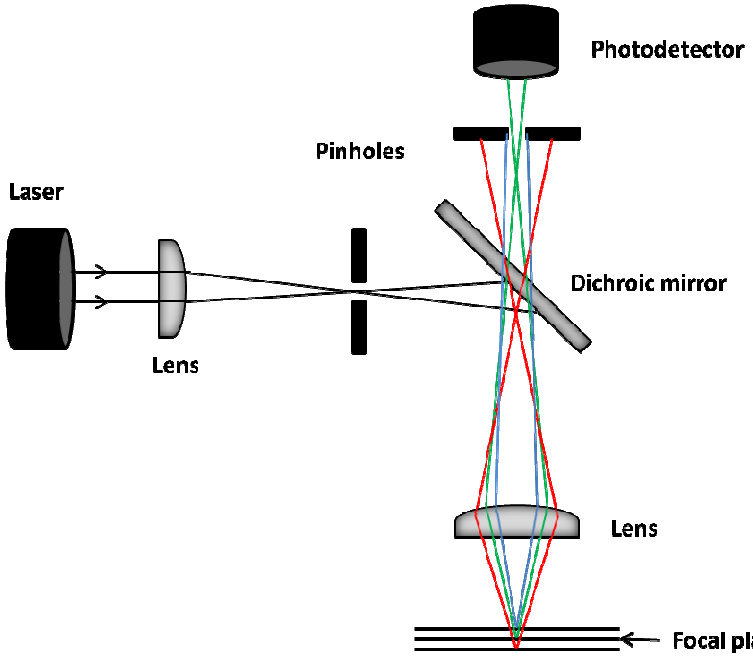

Figure 1.8. Simplified schematic of a confocal laser scanning microscope (CLSM). Here, the use of pinholes allow the measurement of light in a single focal plane, shown in green.

Modern systems can now be equipped with tunable lasers, beam splitters and rapid scanning systems offering further improvements. As an optical technique, lateral resolution is to the order of the diffraction limit of visible light, *ie* ~200 nm. The ability to visualise (and spatially resolve) surface and internal features, coupled with measurement of light intensities, make CLSM and related techniques a highly versatile tool for optical tracking of dynamic processes.[59,63-68]

1.4 Scanned probe microscopy

Another major family of techniques used for surface analysis are those of scanned probe microscopy (SPM). The principle is simple, a probe, able to measure a property of interest, is scanned across a surface and an image is constructed of said property in the *x*,*y* dimensions. Properties commonly measured include topography, mechanical probe-sample interaction forces and electrical or electrochemical properties. The earliest example was the scanning tunnelling microscope (STM),[69] able to probe tunnelling currents between a metal tip and conducting surface, after which a host of other technologies have developed.

In the simplest modes of operation, SPMs can be scanned at a constant height. More commonly however, a feedback mechanism is used to maintain a constant probe-sample interaction (often separation or force) whilst measuring further properties independently of this. Examples of this are discussed in the following section. Finally, accuracy of the scanning system itself is paramount,

and is generally achieved using piezoelectronic-based scanners with modern digital software control.

Electrochemical SPM (EC-SPM) techniques provide a useful means to measure localised activity, uptake and electrical conductivity properties and are discussed in the following section. Firstly, however, the most common form of SPM is discussed.

1.4.1 Atomic force microscopy (AFM)

Atomic force microscopy (AFM)[70-73] is the most commonly used SPM technique in surface analysis and provides a useful benchmark with which to compare emerging techniques. Here, the primary measured quantity is generally the surface topography, measured using probe-surface interaction force as the feedback parameter. This interaction force is generally measured as a repulsive force between a static, force-sensitive probe or as a damping of oscillation from a resonating probe. The probe in question extends downwards from a near-to horizontal cantilever; this cantilever is generally reflective and a reflected laser beam incident on a split photodiode is used as a means to measure its position, which can be calibrated to the force sensitivity of each cantilever. A typical 'sample scanning' configuration is shown in Figure 1.9.

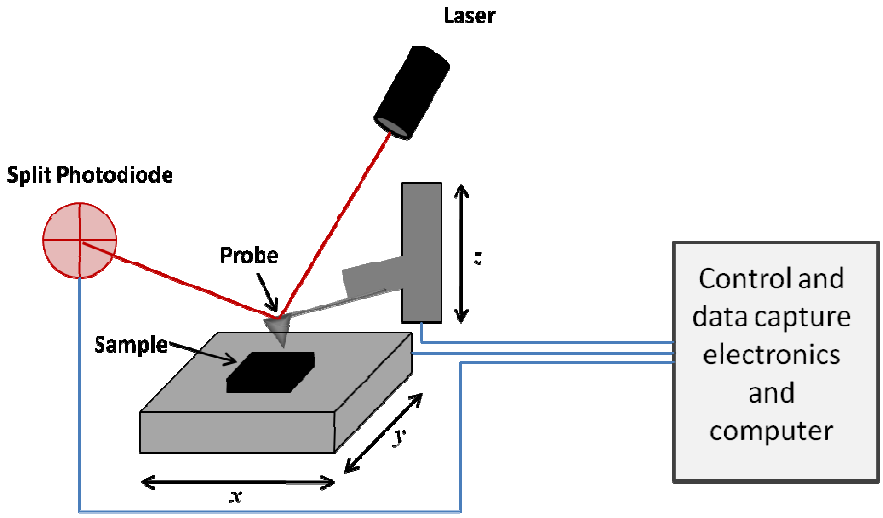

Figure 1.9. A simplified schematic of a 'sample scanning' AFM configuration. The scanning set up is common to many types of SPM. In AFM specifically, the feedback mechanism is based upon a laser reflected off the cantilever and measured by a split photodiode detector.

This configuration can then be used to measure a host of secondary properties. For example, coating a probe with a metal, and contacting to current-measuring equipment while applying a bias between a tip and (semi-)conducting sample, provides a means to measure localised conductivity (conducting, C-AFM).[74] Further electrostatic and magnetic properties can similarly be measured. The resolution of AFM is largely controlled by the dimensions of the probe apex, which is generally between 1 and 100 nm, depending on material, coating *etc*.

1.4.2 Scanning electrochemical microscopy (SECM)

The scanning electrochemical microscope (SECM), as introduced by the Bard group,[75,76] represents the simplest form of EC-SPM. In the most common amperometric configuration, a solid electrode tip is scanned across a surface. The tip potential is set to study a particular electrochemical reaction (*i.e.* reduce or oxidise a given species). This is a well established electrochemical technique and is the subject of several reviews.[77-81] In general, a well-defined electrode is used, allowing quantification of diffusion rates and kinetics. A common configuration consists of an insulating layer surrounding a disk electrode that is large enough to assume hemispherical diffusion to the electrode. The steady-state current of this configuration held far from a surface is defined by equation 1.8

$$i_{\infty} = 4naFdc \qquad (1.8)$$

where n is the number of electrons transferred per chemical reaction, a is the electrode radius, F is Faraday's constant, d is the diffusion coefficient of the electrochemical mediator and c is the bulk concentration. The number 4 here relates to the assumption of an infinite insulating plane around the electrode resulting in purely hemispherical diffusion of mediator to the electrode. This current can be affected by a number of factors. The simplest are 'feedback' modes, which refers to either the approach to an insulating surface, causing a blocking of the (ideally hemispherical) diffusion of the redox-active species to the electrode and therefore a reduction in current (negative feedback, shown in Figure 1.10) or the approach to a conducting surface, resulting in an increase in current, due to regeneration of the mediator at the surface. The use of the term

'feedback' here can be confusing as this is rarely actually used as a feedback setpoint, and purely refers to an interaction with a surface.

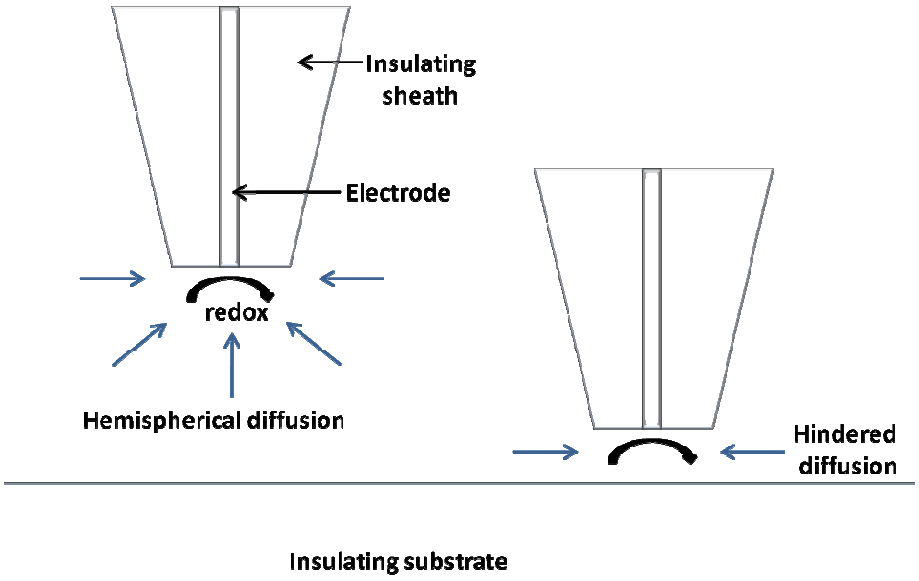

Figure 1.10. The basic principle of an SECM probe, where an electrode in bulk solution is subject to steady-state hemispherical diffusion of a mediator to a disk electrode in an infinite insulating sheath. When this electrode approaches an insulating (inert) surface this diffusion is hindered, thus reducing the Faradaic current measured. This is known as 'negative feedback'.

The other major mode is generation-collection. Here the electrode approaches a surface generating a redox active species (eg another electrode, though also biological systems or porous surfaces are possible). This mode has the advantage of measuring specific reactions locally. This technique is reasonably common for biological measurements due to the ability to measure localised biological activity in a non-destructive manner which is the subject of several dedicated reviews.[80-83]

However, SECM alone lacks an independent mode of feedback, meaning it is impossible to control tip-sample separation while measuring localised activity. Several developments have been employed to overcome this, though none have been generally adopted, as will be discussed later in this chapter.

1.4.3 Scanning ion conductance microscopy (SICM)

The scanning ion conductance microscope (SICM),[84-86] though not strictly speaking an electrochemical technique, is closely associated due to the ability to measure ion currents, and therefore also allowing the detection of (electrochemically inert) ionic species. The principle is also simple; the probe employed is a solution-filled pipette containing a (quasi)reference electrode and measured against a further reference electrode in bulk. Here, a migration current between the two electrodes is measured (see Figure 1.11).

Electrical resistance is largely controlled by the pipette dimensions, especially the aperture size. Topography can be faithfully measured via an increase in resistance as the pipette nears a surface, provided that the ionic concentration (and, therefore, conductivity of the solution) is constant. Likewise, local changes in ionic concentration can be measured, though care must be taken to distinguish this from topography. Like SECM, this technique has also been used for various biological measurements.[85-91]

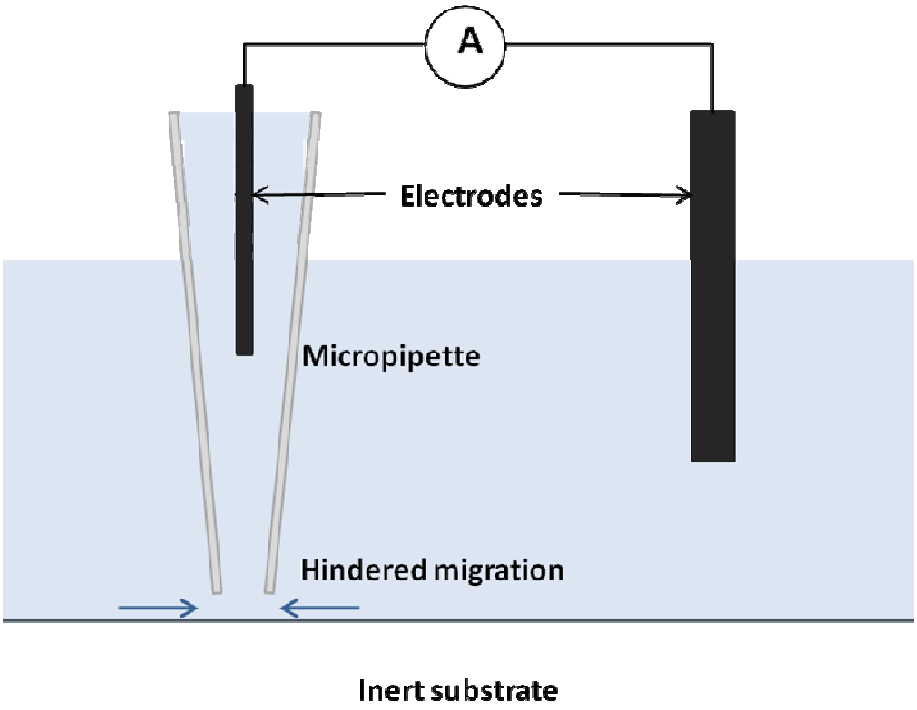

Figure 1.11. Schematic of the SICM set up, where a solution-filled pipette contains a quasi-reference counter electrode which measures a migration (ion) current between the pipette and a further quasi-reference counter electrode in bulk. As the pipette approaches a surface this migration is hindered, producing a drop in the measured ion current.

1.4.4 Hybrid SECM techniques

As mentioned earlier, the major drawback to SECM measurements is the inability to deconvolute surface topography and activity. Several systems are in place to overcome this, though generally such systems have, so far, not been widely adopted outside their groups of origin. Combined SECM-AFM[92-95] is the main exception to this; this method is particularly attractive as it combines the precise force control and topography measurement of AFM with the activity

measurement of SECM. Much work has gone into the batch fabrication of appropriate probes for this technique.[96-100] Further approaches include shear force-SECM,[101-103] alternating current (ac)-SECM[104-106] and intermittent contact (IC)-SECM,[107,108] which generally employ standard SECM probes (solid electrodes 25 μm and below) with additional measurements made by tuning forks, lock-in amplifiers or strain gauge sensors.

The other major development is miniaturisation of the probes. Thus, initial measurements made with 25 μm diameter tip electrodes are being superseded by nanoelectrodes.[109-111] At this scale, a close control of tip-sample separation becomes increasingly important as electrode sensing ranges drastically decrease. A promising approach for this is combined SECM-SICM.[112-114] Here, a dual barrelled 'theta' pipette is commonly used where one barrel is filled with a conducting material (generally carbon) to make a solid SECM probe and the other barrel is solution-filled and a reference electrode inserted to make an SICM barrel. Pipettes can easily be made to sub-micron sizes and are relatively inexpensive to make.

1.4.5. Scanning electrochemical cell microscopy (SECCM) and related techniques

An alternative approach is to work in a defined droplet formed between a pipette and surface, thus defining a 'cell' area and removing the need to immerse a sample in continuous media. Scanning micropipette contact method (SMCM)[115] represents an early configuration of this approach, using a micron-

sized micropipette to record localized electrochemical measurements in a droplet size approximately equal to that of the pipette geometry. Exchanging a single-barreled pipette for a dual channel 'theta' pipette, termed scanning electrochemical cell microscopy (SECCM, shown in Figure 1.12),[116] far increases the potential of this approach; the dual channel design allowing migration of species through the droplet cell *i.e.* with the two barrels acting as an inlet and outlet for the cell. The migratory flux between the barrels and to the surface has been modelled,[117] thus allowing a high level of control. Positional feedback is also based upon this migration current allowing control of the meniscus height on both conducting and insulating surfaces.

So far this approach has been used on electrochemically-active systems[118-123] giving both a spatially-resolved electrode area and good control of mass transport rates to the surface. There is, however, broad scope for utility in non-Faradaic processes *eg.* study of localized adsorption kinetics and controlled delivery to, and patterning of, surfaces and interfaces. Creation of probes is a simple, inexpensive and flexible process. As a non-contact technique, the range of samples applicable to this technique is potentially broad, and pipette sizes can be tailored from tens of nanometers to tens of microns. Furthermore, when necessary, the entire probe apex can be immersed in small droplets of solution and still maintain a high level of positional control.

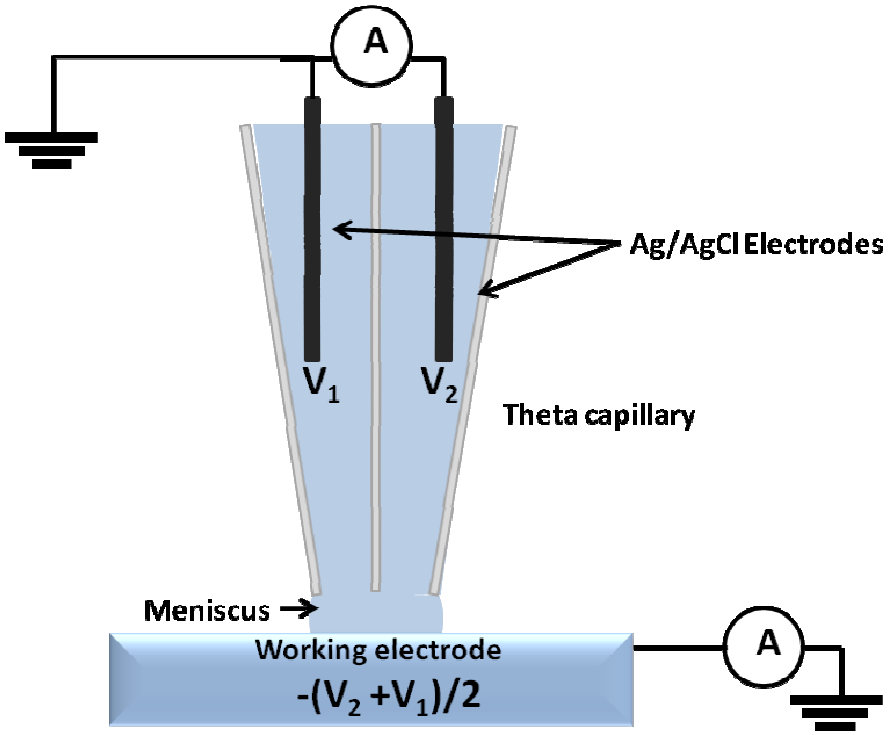

Figure 1.12. The SECCM set up where the positional feedback is based on the alternating current component of the migration current (between barrels) when undergoing vertical oscillation. The electrode surface is biased as the inverse of the average of the two barrel potentials (applied to quasi-reference electrodes contained in each barrel), and the surface (Faradiac) current measured with respect to ground.

1.4.6 SPM based microfluidic cells

A recent addition to the applications of scanned probe microscopies (SPMs) has been the introduction of vertically-mounted microfluidic probes to provide a well-defined and spatially-resolved flux of species to a surface without the need to immerse the entire sample in solution. Traditional approaches for defined surface modification include inkjet printing, well-established for depositing liquids on surfaces,[124] but involves the drying of droplets with related

artifacts. Many approaches have also been used for surface modification in continuous media. Dip pen nanolithography,[125] for example, is an atomic force microscopy (AFM) based approach for patterning on the nanometer-scale. Further techniques involve local electrochemical control using SECM and capillary-based systems utilising micro- and nano-pipets, primarily SICM. This allows controlled electromigration as a means to deliver charged species to a surface of interest, and has been demonstrated using DNA and proteins[126] and for local delivery of fluorescent molecular probes to cells.[127]

In recent years, new technologies have been developed, three major example are 'fountain pen',[128] combined microfluidic/SECM 'push-pull'[129] and vertical microfluidic probes.[130] The potential uses of these types of localized microfluidic cells is broad encompassing, for example, delivery, patterning and analysis of surfaces and interfaces.

1.5 Aims of thesis

The aims of this thesis involve the application and assessment of new analytical techniques for characterisation of plant root surfaces and the study of bioadhesion of potential active ingredient delivery systems to these surfaces. The following chapters demonstrate the use of modern spectroscopic and microscopic techniques to study both mimetic and live cell systems. The major parts of this thesis can be summarised as follows:

(A) Chapter 3 concerns the development of models for the study of adsorption kinetics of functionalised macromolecules to plant root and soil surfaces. The platform used for these studies is evanescent wave-cavity ring-down spectroscopy (EW-CRDS), a sensitive technique for the study of the solid/liquid interface. Mimetic surfaces are created at this interface and initial adsorption kinetics of functionalised macromolecules elucidated. These studies are then extended to consider the study of cell membrane models using the same technique.

(B) Chapter 4 concerns the application of modern optical microscopy, confocal laser scanning microscopy (CLSM), to measure adsorption rates of charged particles to the same mimetic surfaces. Flow devices based upon scanning electrochemical cell microscopy (SECCM) probes are then developed for study at controlled mass-transport rates and the ability to control delivery to individual root hair cells. The versatility of such devices is then demonstrated.

(C) Chapter 5 concerns the application and further development of electrochemical scanned probe microscopy (EC-SPM) to the study of the root cell surface. The techniques used are intermittent contact-scanning electrochemical microscopy (IC-SECM), scanning electrochemical cell microscopy (SECCM) and scanning ion conductance microscopy (SICM). These studies are used to show localised activity and ion concentrations at the live cell surfaces and are evaluated for their suitability to such studies.

1.6 References

(1) Tan, K. H. *Principles of Soil Chemistry*; Marcel Dekker, 1998.

(2) Osmond, D. A. *Micropedology. Soils and Fertiliser,* **1958**, *21*, 1.

(3) Mackenzie, R. C. *Soil Components*; Springer-Verlag: New York, 1975.

(4) *Humus Chemistry. Genesis, Composition, Reactions*; 2nd ed.; Stevenson, F. J., Ed.; Wiley and Sons: New York, 1994.

(5) D.Mauseth, J. *Botany: An introduction to plant biology*; Jones and Bartlett, 2003.

(6) Cavic, B. A.; Hayward, G. L.; Thompson, M. *Analyst* **1999**, *124*, 1405.

(7) Sauerbrey, G. *Z. Phys.* **1959**, *155*, 206.

(8) Bandey, H. L.; Hillman, A. R.; Brown, M. J.; Martin, S. J. *Faraday Discussions* **1997**, *107*, 105.

(9) Bandey, H. L.; Martin, S. J.; Cernosek, R. W.; Hillman, A. R. *Analytical Chemistry* **1999**, *71*, 2205.

(10) Martin, S. J.; Bandey, H. L.; Cernosek, R. W.; Hillman, A. R.; Brown, M. J. *Analytical Chemistry* **2000**, *72*, 141.

(11) Gottesfeld, S. *Electroanalytical Chemistry* **1989**, *15*, 143.

(12) Theeten, J. B.; Aspnes, D. E. *Annual Review of Materials Science* **1981**, *11*, 97.

(13) Richter, R. P.; Brisson, A. R. *Biophysical Journal* **2005**, *88*, 3422.

(14) Welin, S.; Elwing, H.; Arwin, H.; Lundstrom, I.; Wikstrom, M. *Analytica Chimica Acta* **1984**, *163*, 263.

(15) Awan, M. A.; Dimonie, V. L.; Filippov, L. K.; El-Aasser, M. S. *Langmuir* **1997**, *13*, 130.

(16) Bain, C. D. *Current Opinion in Colloid & Interface Science* **1998**, *3*, 287.

(17) Chen, Z.; Shen, Y. R.; Somorjai, G. A. *Annual Review of Physical Chemistry* **2002**, *53*, 437.

(18) Noskov, B. A.; Akentiev, A. V.; Grigoriev, D. O.; Loglio, G.; Miller, R. *Journal of Colloid and Interface Science* **2005**, *282*, 38.

(19) Vidal, F.; Tadjeddine, A. *Reports on Progress in Physics* **2005**, *68*, 1095.

(20) Walter, H.; Harrats, C.; Muller-Buschbaum, P.; Jerome, R.; Stamm, M. *Langmuir* **1999**, *15*, 1260.

(21) Fu, Z. G.; Santore, M. M. *Colloids and Surfaces a-Physicochemical and Engineering Aspects* **1998**, *135*, 63.

(22) Milosevic, M. *Applied Spectroscopy Reviews* **2004**, *39*, 365.

(23) Homola, J.; Koudela, I.; Yee, S. S. *Sensors and Actuators B-Chemical* **1999**, *54*, 16.

(24) Homola, J.; Yee, S. S.; Gauglitz, G. *Sensors and Actuators B-Chemical* **1999**, *54*, 3.

(25) O'Keefe, A.; Deacon, D. A. G. *Review of Scientific Instruments* **1988**, *59*, 2544.

(26) Vallance, C. *New Journal of Chemistry* **2005**, *29*, 867.

(27) Scherer, J. J.; Paul, J. B.; Okeefe, A.; Saykally, R. J. *Chemical Reviews* **1997**, *97*, 25.

(28) Wheeler, M. D.; Newman, S. M.; Orr-Ewing, A. J.; Ashfold, M. N. R. *Journal of the Chemical Society-Faraday Transactions* **1998**, *94*, 337.

(29) Berden, G.; Peeters, R.; Meijer, G. *International Reviews in Physical Chemistry* **2000**, *19*, 565.

(30) *Cavity-Ringdown Spectroscopy: An Ultrotrace-Absorption Measurement Technique*; 1 ed.; Busch, K. W.; Busch, M. A., Eds.; American Chemical Society, Washington, DC, 1999.

(31) Hallock, A. J.; Berman, E. S. F.; Zare, R. N. *Analytical Chemistry* **2002**, *74*, 1741.

(32) Hallock, A. J.; Berman, E. S. F.; Zare, R. N. *Journal of the American Chemical Society* **2003**, *125*, 1158.

(33) Kleine, D.; Lauterbach, J.; Kleinermanns, K.; Hering, P. *Applied Physics B-Lasers and Optics* **2001**, *72*, 249.

(34) Alexander, A. J. *Chemical Physics Letters* **2004**, *393*, 138.

(35) Snyder, K. L.; Zare, R. N. *Analytical Chemistry* **2003**, *75*, 3086.

(36) Xu, S. C.; Sha, G. H.; Xie, J. C. *Review of Scientific Instruments* **2002**, *73*, 255.

(37) Schnippering, M.; Neil, S. R. T.; Mackenzie, S. R.; Unwin, P. R. *Chemical Society Reviews* **2011**, *40*, 207.

(38) Mazurenka, M.; Wilkins, L.; Macpherson, J. V.; Unwin, P. R.; Mackenzie, S. R. *Analytical Chemistry* **2006**, *78*, 6833.

(39) Schnippering, M.; Powell, H. V.; Zhang, M. Q.; Macpherson, J. V.; Unwin, P. R.; Mazurenka, M.; Mackenzie, S. R. *Journal of Physical Chemistry C* **2008**, *112*, 15274.

(40) Powell, H. V.; Schnippering, M.; Mazurenka, M.; Macpherson, J. V.; Mackenzie, S. R.; Unwin, P. R. *Langmuir* **2009**, *25*, 248.

(41) Mazurenka, M.; Hamilton, S. M.; Unwin, P. R.; Mackenzie, S. R. *Journal of Physical Chemistry C* **2008**, *112*, 6462.

(42) Li, F. P.; Zare, R. N. *Journal of Physical Chemistry B* **2005**, *109*, 3330.

(43) Hannon, T. E.; Chah, S. W.; Zare, R. N. *Journal of Physical Chemistry B* **2005**, *109*, 7435.

(44) Fan, H. F.; Hung, C. Y.; Lin, K. C. *Analytical Chemistry* **2006**, *78*, 3583.

(45) Fisk, J. D.; Batten, R.; Jones, G.; O'Reilly, J. P.; Shaw, A. M. *Journal of Physical Chemistry B* **2005**, *109*, 14475.

(46) O'Reilly, J. P.; Butts, C. P.; I'Anson, I. A.; Shaw, A. M. *Journal of the American Chemical Society* **2005**, *127*, 1632.

(47) Shaw, A. M.; Hannon, T. E.; Li, F. P.; Zare, R. N. *Journal of Physical Chemistry B* **2003**, *107*, 7070.

(48) Everest, M. A.; Black, V. M.; Haehlen, A. S.; Haveman, G. A.; Kliewer, C. J.; Neill, H. A. *Journal of Physical Chemistry B* **2006**, *110*, 19461.

(49) Schnippering, M.; Unwin, P. R.; Hult, J.; Laurila, T.; Kaminski, C. F.; Langridge, J. M.; Jones, R. L.; Mazurenka, M.; Mackenzie, S. R. *Electrochemistry Communications* **2008**, *10*, 1827.

(50) Fan, H. F.; Li, F. P.; Zare, R. N.; Lin, K. C. *Analytical Chemistry* **2007**, *79*, 3654.

(51) Chen, M.-S.; Fan, H.-F.; Lin, K.-C. *Analytical Chemistry* **2010**, *82*, 868.

(52) Schnippering, M.; Powell, H. V.; Mackenzie, S. R.; Unwin, P. R. *The Journal of Physical Chemistry C* **2009**, *113*, 20221.

(53) Martin, W. B.; Mirov, S.; Martyshkin, D.; Venugopalan, R.; Shaw, A. M. *Journal of Biomedical Optics* **2005**, *10*.

(54) Wang, X. F.; Hinz, M.; Vogelsang, M.; Welsch, T.; Kaufmann, D.; Jones, H. *Chemical Physics Letters* **2008**, *467*, 9.

(55) Powell, H. V.; Schnippering, M.; Cheung, M.; Macpherson, J. V.; Mackenzie, S. R.; Stavros, V. G.; Unwin, P. R. *ChemPhysChem* **2010**, *11*, 2985.

(56) Chen, Y.; Lagerholm, B. C.; Yang, B.; Jacobson, K. *Methods* **2006**, *39*, 147.

(57) Ciruela, F. *Current Opinion in Biotechnology* **2008**, *19*, 338.

(58) Petrasek, Z.; Eckert, H.-J.; Kemnitz, K. *Photosynthesis Research* **2009**, *102*, 157.

(59) Levitt, J. A.; Matthews, D. R.; Ameer-Beg, S. M.; Suhling, K. *Current Opinion in Biotechnology* **2009**, *20*, 28.

(60) Webb, R. H. *Reports on Progress in Physics* **1996**, *59*, 427.

(61) Jalbert, I.; Stapleton, F.; Papas, E.; Sweeney, D. F.; Coroneo, M. *British Journal of Ophthalmology* **2003**, *87*, 225.

(62) Dickinson, M. E.; Bearman, G.; Tille, S.; Lansford, R.; Fraser, S. E. *Biotechniques* **2001**, *31*, 1272.

(63) Bolte, S.; Cordelieres, F. P. *Journal of Microscopy-Oxford* **2006**, *224*, 213.

(64) Kenworthy, A. K. *Methods* **2001**, *24*, 289.

(65) Michalet, X.; Weiss, S.; Jager, M. *Chemical Reviews* **2006**, *106*, 1785.

(66) Moerner, W. E.; Fromm, D. P. *Review of Scientific Instruments* **2003**, *74*, 3597.

(67) Stephens, D. J.; Allan, V. J. *Science* **2003**, *300*, 82.

(68) Suhling, K.; French, P. M. W.; Phillips, D. *Photochemical & Photobiological Sciences* **2005**, *4*, 13.

(69) Binnig, G.; Rohrer, H. *Helvetica Physica Acta* **1982**, *55*, 726.

(70) Binnig, G.; Quate, C. F.; Gerber, C. *Physical Review Letters* **1986**, *56*, 930.

(71) Butt, H. J.; Cappella, B.; Kappl, M. *Surface Science Reports* **2005**, *59*, 1.

(72) Giessibl, F. J. *Reviews of Modern Physics* **2003**, *75*, 949.

(73) Garcia, R.; Perez, R. *Surface Science Reports* **2002**, *47*, 197.

(74) Kelley, T. W.; Granstrom, E. L.; Frisbie, C. D. *Advanced Materials* **1999**, *11*, 261.

(75) Bard, A. J.; Fan, F. R. F.; Kwak, J.; Lev, O. *Analytical Chemistry* **1989**, *61*, 132.

(76) Kwak, J.; Bard, A. J. *Analytical Chemistry* **1989**, *61*, 1221.

(77) Amemiya, S.; Bard, A. J.; Fan, F.-R. F.; Mirkin, M. V.; Unwin, P. R. In *Annual Review of Analytical Chemistry* 2008; Vol. 1, p 95.

(78) Mirkin, M. V.; Horrocks, B. R. *Analytica Chimica Acta* **2000**, *406*, 119.

(79) Sun, P.; Laforge, F. O.; Mirkin, M. V. *Physical Chemistry Chemical Physics* **2007**, *9*, 802.

(80) Amemiya, S.; Guo, J.; Xiong, H.; Gross, D. A. *Analytical and Bioanalytical Chemistry* **2006**, *386*, 458.

(81) Edwards, M. A.; Martin, S.; Whitworth, A. L.; Macpherson, J. V.; Unwin, P. R. *Physiological Measurement* **2006**, *27*, R63.

(82) Roberts, W. S.; Lonsdale, D. J.; Griffiths, J.; Higson, S. P. J. *Biosensors & Bioelectronics* **2007**, *23*, 301.

(83) Stoica, L.; Neugebauer, S.; Schuhmann, W. In *Biosensing for the 21st Century*; Renneberg, R. L. F., Ed. 2008; Vol. 109, p 455.

(84) Hansma, P. K.; Drake, B.; Marti, O.; Gould, S. A. C.; Prater, C. B. *Science* **1989**, *243*, 641.

(85) Anariba, F.; Anh, J. H.; Jung, G.-E.; Cho, N.-J.; Cho, S.-J. *Modern Physics Letters B* **2012**, *26*.

(86) Miragoli, M.; Moshkov, A.; Novak, P.; Shevchuk, A.; Nikolaev, V. O.; El-Hamamsy, I.; Potter, C. M. F.; Wright, P.; Kadir, S. H. S. A.; Lyon, A. R.; Mitchell, J. A.; Chester, A. H.; Klenerman, D.; Lab, M. J.; Korchev, Y. E.; Harding, S. E.; Gorelik, J. *Journal of the Royal Society Interface* **2011**, *8*, 913.

(87) Gorelik, J.; Zhang, Y. J.; Shevchuk, A. I.; Frolenkov, G. I.; Sanchez, D.; Lab, M. J.; Vodyanoy, I.; Edwards, C. R. W.; Klenerman, D.; Korchev, Y. E. *Molecular and Cellular Endocrinology* **2004**, *217*, 101.

(88) Korchev, Y. E.; Gorelik, J.; Lab, M. J.; Sviderskaya, E. V.; Johnston, C. L.; Coombes, C. R.; Vodyanoy, I.; Edwards, C. R. W. *Biophysical Journal* **2000**, *78*, 451.

(89) Korchev, Y. E.; Milovanovic, M.; Bashford, C. L.; Bennett, D. C.; Sviderskaya, E. V.; Vodyanoy, I.; Lab, M. J. *Journal of Microscopy-Oxford* **1997**, *188*, 17.

(90) Mann, S. A.; Hoffmann, G.; Hengstenberg, A.; Schuhmann, W.; Dietzel, I. D. *Journal of Neuroscience Methods* **2002**, *116*, 113.

(91) Zhang, Y. J.; Gorelik, J.; Sanchez, D.; Shevchuk, A.; Lab, M.; Vodyanoy, I.; Klenerman, D.; Edwards, C.; Korchev, Y. *Kidney International* **2005**, *68*, 1071.

(92) Dobson, P. S.; Weaver, J. M. R.; Holder, M. N.; Unwin, P. R.; Macpherson, J. V. *Analytical Chemistry* **2005**, *77*, 424.

(93) Jones, C. E.; Unwin, P. R.; Macpherson, J. V. *ChemPhysChem* **2003**, *4*, 139.

(94) Macpherson, J. V.; Unwin, P. R. *Analytical Chemistry* **2000**, *72*, 276.

(95) Macpherson, J. V.; Unwin, P. R. *Analytical Chemistry* **2001**, *73*, 550.

(96) Akiyama, T.; Gullo, M. R.; de Rooij, N. F.; Tonin, A.; Hidber, H. R.; Frederix, P.; Engel, A.; Staufer, U. *Japanese Journal of Applied Physics Part 1-Regular Papers Short Notes & Review Papers* **2004**, *43*, 3865.

(97) Frederix, P. L. T. M.; Bosshart, P. D.; Akiyama, T.; Chami, M.; Gullo, M. R.; Blackstock, J. J.; Dooleweerdt, K.; de Rooij, N. F.; Staufer, U.; Engel, A. *Nanotechnology* **2008**, *19*.

(98) Gullo, M. R.; Frederix, P. L. T. M.; Akiyama, T.; Engel, A.; deRooij, N. F.; Staufer, U. *Analytical Chemistry* **2006**, *78*, 5436.

(99) Shin, H.; Hesketh, P. J.; Mizaikoff, B.; Kranz, C. *Analytical Chemistry* **2007**, *79*, 4769.

(100) Shin, H.; Hesketh, P. J.; Mizaikofff, B.; Kranz, C. *Sensors and Actuators B-Chemical* **2008**, *134*, 488.

(101) Hengstenberg, A.; Kranz, C.; Schuhmann, W. *Chemistry-a European Journal* **2000**, *6*, 1547.

(102) Katemann, B. B.; Schulte, A.; Schuhmann, W. *Chemistry-a European Journal* **2003**, *9*, 2025.

(103) Lee, Y.; Ding, Z. F.; Bard, A. J. *Analytical Chemistry* **2002**, *74*, 3634.

(104) Etienne, M.; Schulte, A.; Schuhmann, W. *Electrochemistry Communications* **2004**, *6*, 288.

(105) Katemann, B. B.; Inchauspe, C. G.; Castro, P. A.; Schulte, A.; Calvo, E. J.; Schuhmann, W. *Electrochimica Acta* **2003**, *48*, 1115.

(106) Katemann, B. B.; Schulte, A.; Calvo, E. J.; Koudelka-Hep, M.; Schuhmann, W. *Electrochemistry Communications* **2002**, *4*, 134.

(107) McKelvey, K.; Edwards, M. A.; Unwin, P. R. *Analytical Chemistry* **2010**, *82*, 6334.

(108) McKelvey, K.; Snowden, M. E.; Peruffo, M.; Unwin, P. R. *Analytical Chemistry* **2011**, *83*, 6447.

(109) Elsamadisi, P.; Wang, Y. X.; Velmurugan, J.; Mirkin, M. V. *Analytical Chemistry* **2011**, *83*, 671.

(110) Katemann, B. B.; Schulte, A.; Schuhmann, W. *Electroanalysis* **2004**, *16*, 60.

(111) Sun, P.; Mirkin, M. V. *Analytical Chemistry* **2006**, *78*, 6526.

(112) Comstock, D. J.; Elam, J. W.; Pellin, M. J.; Hersam, M. C. *Analytical Chemistry* **2010**, *82*, 1270.

(113) Morris, C. A.; Chen, C.-C.; Baker, L. A. *The Analyst* **2012**, *137*, 2933.

(114) Takahashi, Y.; Shevchuk, A. I.; Novak, P.; Murakami, Y.; Shiku, H.; Korchev, Y. E.; Matsue, T. *Journal of the American Chemical Society* **2010**, *132*, 10118.

(115) Williams, C. G.; Edwards, M. A.; Colley, A. L.; Macpherson, J. V.; Unwin, P. R. *Analytical Chemistry* **2009**, *81*, 2486.

(116) Ebejer, N.; Schnippering, M.; Colburn, A. W.; Edwards, M. A.; Unwin, P. R. *Analytical Chemistry* **2010**, *82*, 9141.

(117) Snowden, M. E.; Guell, A. G.; Lai, S. C. S.; McKelvey, K.; Ebejer, N.; O'Connell, M. A.; Colburn, A. W.; Unwin, P. R. *Analytical Chemistry* **2012**.

(118) Lai, S. C. S.; Dudin, P. V.; Macpherson, J. V.; Unwin, P. R. *Journal of the American Chemical Society* **2011**, *133*, 10744.

(119) Guell, A. G.; Ebejer, N.; Snowden, M. E.; Macpherson, J. V.; Unwin, P. R. *Journal of the American Chemical Society* **2012**, *134*, 7258.

(120) Guell, A. G.; Ebejer, N.; Snowden, M. E.; McKelvey, K.; Macpherson, J. V.; Unwin, P. R. *Proceedings of the National Academy of Sciences of the United States of America* **2012**, *109*, 11487.

(121) Lai, S. C. S.; Patel, A. N.; McKelvey, K.; Unwin, P. R. *Angewandte Chemie-International Edition* **2012**, *51*, 5405.

(122) Miller, T. S.; Ebejer, N.; Gueell, A. G.; Macpherson, J. V.; Unwin, P. R. *Chemical Communications* **2012**, *48*, 7435.

(123) Patten, H. V.; Meadows, K. E.; Hutton, L. A.; Iacobini, J. G.; Battistel, D.; McKelvey, K.; Colburn, A. W.; Newton, M. E.; Macpherson, J. V.; Unwin, P. R. *Angewandte Chemie-International Edition* **2012**, *51*, 7002.

(124) Le, H. P. *J. Imaging Sci. Technol.* **1998**, *42*, 49.

(125) Piner, R. D.; Zhu, J.; Xu, F.; Hong, S. H.; Mirkin, C. A. *Science* **1999**, *283*, 661.

(126) Bruckbauer, A.; Ying, L.; Rothery, A. M.; Zhou, D.; Shevchuk, A. I.; Abell, C.; Korchev, Y. E.; Klenerman, D. *Journal of the American Chemical Society* **2002**, *124*, 8810.

(127) Bruckbauer, A.; James, P.; Zhou, D.; Yoon, J. W.; Excell, D.; Korchev, Y.; Jones, R.; Klenerman, D. *Biophysical Journal* **2007**, *93*, 3120.

(128) Cortes-Salazar, F.; Lesch, A.; Momotenko, D.; Busnel, J. M.; Wittstock, G.; Girault, H. H. *Anal. Methods* **2010**, *2*, 817.

(129) Momotenko, D.; Cortes-Salazar, F.; Lesch, A.; Wittstock, G.; Girault, H. H. *Analytical Chemistry* **2011**, *83*, 5275.

(130) Kaigala, G. V.; Lovchik, R. D.; Drechsler, U.; Delamarche, E. *Langmuir* **2011**, *27*, 5686.

Chapter 2. Experimental

This chapter concerns primarily the techniques and instrumentation used in this thesis. In addition, the materials and experimental details for each study are described in the relevant individual chapters. Both the EW-CRDS and EC-SPM equipment were built and designed in house and, therefore, unique to this group. As such, they are described in detail. Further to this, other experimental configurations are described (CLSM and AFM), as well as details of combined flow and delivery systems.

2.1. EW-CRDS Instrumentation

For EW-CRDS experiments a single configuration was used as previously developed in house.[1-3] A single laser excitation source was used and chromophores chosen to absorb at the appropriate wavelength. This configuration is described in detail below.

2.1.1 EW-CRDS apparatus

The EW-CRD spectrometer (shown schematically in Figure 2.1) was operated in ring-cavity geometry as described in detail elsewhere.[1,4] The cavity comprised two high-reflectance mirrors (R = 99.997% at 405

nm (Los Gatos Research)) and an intra-cavity right-angled fused silica prism (anti-reflective coated, R <0.5%, λ = 350-532 nm for normal incidence (CVI Melles Griot). Light pulses (~10 µs) were injected into the cavity using a TTL modulated diode laser (405 nm, 50 mW maximum output, Power Technology Inc.). The light intensity circulating within the cavity was measured via the reflection from the incident prism surface using a photomultiplier tube (Electron Tubes, 9781B). To make a ring-down measurement, the light source was rapidly extinguished (t_{fall} < 2 ns) and the PMT signal recorded using a 12-bit 400 MS/s oscilloscope card (Gage CS12400). The ring-down time was calculated in real time using the fast Fourier transform method[2] implemented within LabVIEW.

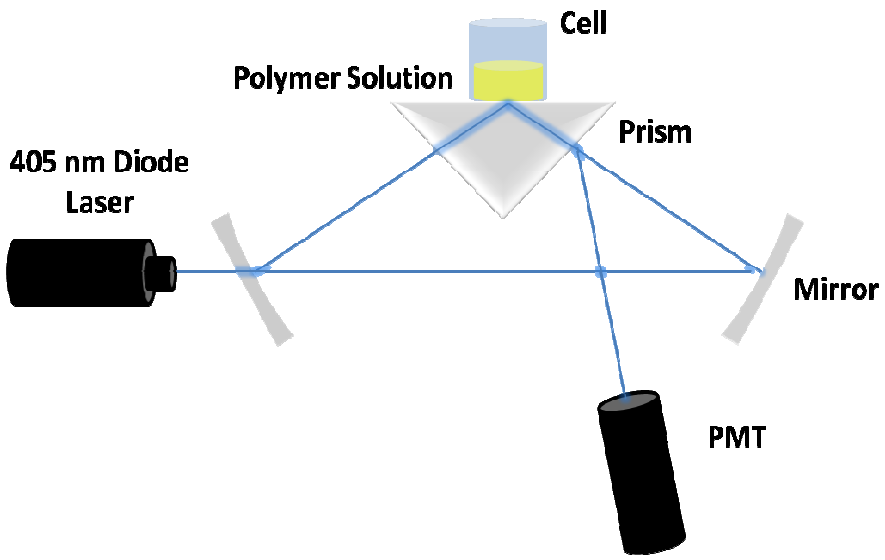

Figure 2.1. Schematic representation of the EW-CRDS set-up used for adsorption experiments. PMT indicates photomultiplier tube.

A cell body was mounted on the hypotenuse of the prism and filled with chromophore solution to create a solution/surface interface. The prism was wetted slightly prior to experiments to (a) allow optimization of the ring-down time and (b) ensure any adsorbed layers were fully hydrated. The characteristic ring-down time was measured as a function of time immediately after addition of the solution used. Data obtained (the characteristic ring-down time, τ, as a function of time) were smoothed using 50-point adjacent averaging. The optical absorbance was calculated from the ring-down time as described in detail in section 1.2.2. The surface coverage due to adsorption was calculated by dividing the optical absorbance by the extinction coefficient (molecular absorption coefficient) derived from UV-VIS spectroscopy (Lambda 25 UV Visible Spectrometer, Perkin-Elmer Instruments).

Between each experiment the prism was wiped with methanol, treated with oxygen plasma for 3 minutes at 100 W (Emitech, K1050X) and wiped again with methanol. This resulted in the prism being returned to a clean state, as confirmed periodically by recording the background ring-down time, τ_0, for a clean prism surface.

2.1.2 Combination of EW-CRDS with flow set up

Similarly, the EW-CRDS set-up could be combined with a flow cell (see Figure 2.2). This was necessary for the supported lipid bilayer (SLB) (a model for the cell membrane) measurements. Here a simple vertical

impinging jet radial flow cell was used with nozzle inner radius of 1 mm. The nozzle-prism separation was chosen to be 500 ± 100 µm, giving well defined hydrodynamics,[5] and ensuring that the nozzle did not penetrate the evanescent field (extending into the solution < 1 µm) from the quartz prism surface.

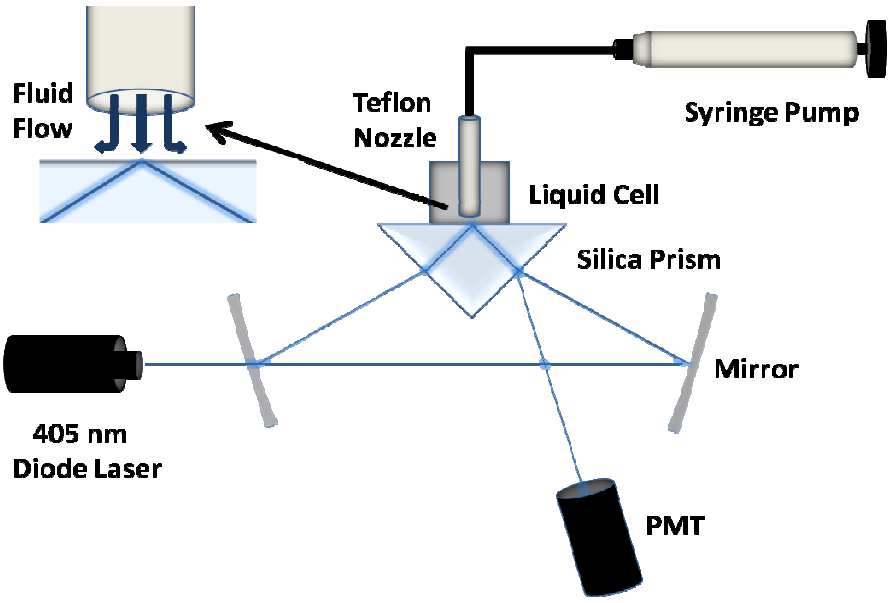

Figure 2.2. Schematic of the EW-CRDS apparatus with integrated impinging jet flow system for washing and exchange of solution. PMT indicates photomultiplier tube.

2.2 Confocal laser scanning microscopy (CLSM) apparatus

Experiments were performed using a laser scanning confocal microscope (Leica TCS SP5 X, Leica Microsystems) equipped with a tunable white light laser (WLL) on an inverted microscope stand (DMI 6000, Leica Microsystems). The tunable white light laser allowed excitation at 1 nm intervals from 470-670 nm. In addition to this, Argon laser excitation wavelengths were available at 458, 470, 488, 496 and 514 nm and a diode laser at 405 nm. This gave very broad scope for use of different fluorophores (dyes). For high resolution measurements such as particle visualisation, a 40x magnification oil immersion lens or 63x magnification oil immersion lens were used. The pinhole was adjusted to view only the surface plane and voltage to the photomultiplier tube (PMT) was optimized to provide a strong signal for each particle without saturating the detector.

For measurement of kinetics, mass transport rates were enhanced using an impinging jet flow system comprising of a Teflon pipe (inner diameter 2 mm, length 5 mm) at a separation of 500 μm from the polymer-coated surface, similar to that used for EW-CRDS experiments (Chapter 2.1.2). Flow rates were varied from 1 ml min^{-1} to 4 ml min^{-1}, under which conditions we assume fully-developed laminar flow.

2.3 Atomic force microscopy

A variety of AFMs were used in this thesis, namely a Multimode V AFM with Nanoscope V controller, Bioscope Catalyst AFM Nanoscope V controller and Enviroscope AFM Nanoscope IV controller (all Bruker-Nano). This allowed a broad range of samples and techniques to be used. In general, the Multimode V was used for ambient experiments and the Catalyst and Enviroscope used for fluid experiments. For these, a selection of silicon (*eg* RFESP-type, Bruker Probes) and silicon nitride (*eg* SNL-type and DNP-type, Bruker Probes) probes were used and instruments were operated in various modes such as contact, Tapping (dynamic) and ScanAsyst modes.

2.4 Electrochemical scanning probe microscopy (EC-SPM) equipment

Multiple EC-SPM configurations were used for this thesis and development continued throughout. These can be grouped into two main classes; existing instrumentation and newer equipment designed and built during this project, as part of a much larger project within the group. As

such, the main components of the newer equipment is described, especially as these are generally used for most experiments in this project.

2.4.1 Hardware and control

The EC-SPM apparatus contained several key parts; a piezoelectric scanning system, various current (or voltage) measuring apparatus and a combination of hardware and software controlled signal processing, control and data acquisition systems. The general set up is shown in Figure 2.3 with (a) a standard SPM and (b) a SPM mounted on an inverted optical microscope.

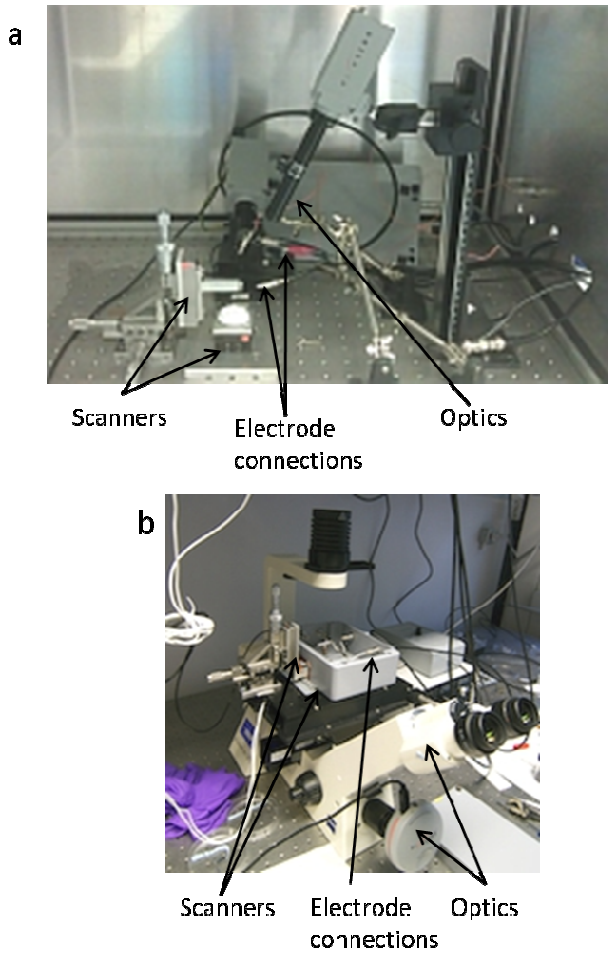

Figure 2.3. The general EC-SPM set up with (a) a standard home built SPM and (b) a SPM mounted on an inverted optical microscope.

2.4.1.1 Scanning systems

Scanning systems were based on piezoelectric actuators ('piezos') controlling movement in the *x,y,z* directions. The major configuration was a 'sample scanning' configuration, *i.e.* the sample was mounted on an *x,y* piezo stage (either Mad City Labs Nano-Bio 300 or Physik Instrumente P-621/P-622.CL) and the probe height controlled via a decoupled *z* piezo

(Physik Instrumente P-753 LISA). The scanning ranges varied from 100 to 300 µm in *x,y* directions and 38 to 100 µm in *z*. The decoupling of the axes served to reduce crosstalk (non-linearities) between the axes and also to allow increased dynamic performance (*ie* oscillation frequency and amplitude) for the *z* piezo.

A simpler configuration (albeit with reduced performance in terms of resolution and dynamic performance) used a 3-axis piezoelectric actuator (Nanocube P-611.3S, Physik Instrumente) attached to the probe. This configuration was used for the combined CLSM/EC-SPM experiments where scanning performance was of less importance.

2.4.1.2 Electrical measurement

Electrical measurements and potential control were performed by a variety of custom-made devices built in house (designed and built by Dr Alex Colburn). These included high sensitivity current-to-voltage amplifiers ('current followers') with sensitivities typically between 1 nA/V to 1 pA/V (Figure 2.4). Higher gain versions allowed measurement of small currents (~ 1 pA) at up to 10 kHz. Also used were floated 'potentiostats', capable of biasing two electrodes independently against ground (Figure 2.5). Combinations of these would allow for multiple electronic configurations, enabling the range of electrochemical measurements required.

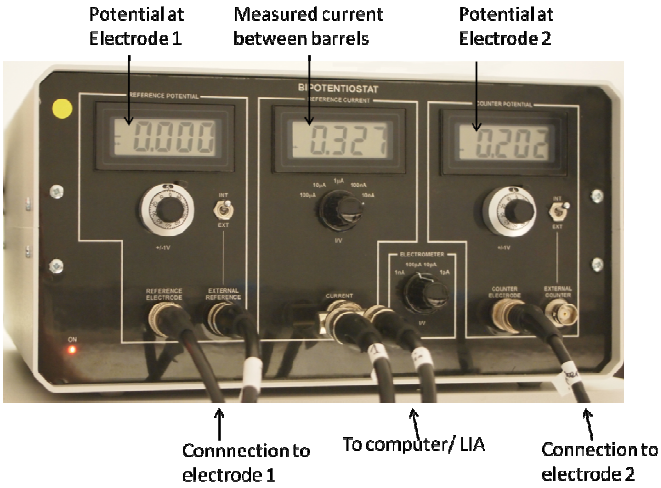

Figure 2.4. A home-built floated bipotentiostat.

Figure 2.5 A home-built high sensitivity current follower.

2.4.1.3 Signal processing, control and data acquisition

The major apparatus used consisted of a commercial digital lock-in amplifier (Stanford Research Systems SR810 or SR830) for measurement of oscillation amplitudes, frequency and phase and a PC equipped with a field programmable gate array (FPGA) card (PCIe-7852R, National

Instruments) and home-written Labview software. The FPGA chip was primarily used for fast data acquisition and processing via a home-built interfacing terminal converting multiple BNC terminals to a single SCSI-type cable. The data acquired via the FPGA card was collected using a PC-based Labview interface, which also served to control applied voltages to both piezos and electrodes. The software had been written to allow maximum flexibility in terms of positional and electrochemical control.

2.4.2 Probe fabrication

The majority of probes used were based on glass (borosilicate or quartz) pulled to various sizes, followed by modification to perform the function of interest.

2.4.2.1 SECCM probe fabrication

Dual barrel borosilicate glass theta capillaries (Harvard Apparatus, UK) were pulled to sizes ranging from 1-20 μm using a laser pipet puller (Model P-2000, Sutter Instruments). In order to form a stable meniscus the outer walls of the pipettes were made hydrophobic using dimethyldichlorosilane. Both barrels were then filled with the solution of interest (~50 μL per barrel) and chlorodised silver wires (Ag/AgCl) were inserted into each barrel to serve as quasi-reference counter electrodes (QRCE).

2.4.2.2 SICM probe fabrication

Single barrelled glass capillaries (borosilicate or quartz, Harvard Apparatus, UK) were pulled to sizes ranging from 0.1-1 µm in a similar manner to above. The single barrel was then filled with the solution of interest and a Ag/AgCl QRCE.

2.5 References

(1) Mazurenka, M.; Hamilton, S. M.; Unwin, P. R.; Mackenzie, S. R. *Journal of Physical Chemistry C* **2008**, *112*, 6462.

(2) Mazurenka, M.; Wada, R.; Shillings, A. J. L.; Butler, T. J. A.; Beames, J. M.; Orr-Ewing, A. J. *Applied Physics B-Lasers and Optics* **2005**, *81*, 135.

(3) Mazurenka, M.; Wilkins, L.; Macpherson, J. V.; Unwin, P. R.; Mackenzie, S. R. *Analytical Chemistry* **2006**, *78*, 6833.

(4) Schnippering, M.; Powell, H. V.; Mackenzie, S. R.; Unwin, P. R. *The Journal of Physical Chemistry C* **2009**, *113*, 20221.

(5) Bitziou, E.; Rudd, N. C.; Edwards, M. A.; Unwin, P. R. *Analytical Chemistry* **2006**, *78*, 1435.

Chapter 3. Evanescent wave-cavity ring-down spectroscopy (EW-CRDS) as a probe of adsorption kinetics at functionalised mimetic interfaces

This chapter contains two key parts; the design and study of root cell surface and soil models and also the extension of the EW-CRDS technique to study supported lipid bilayers (SLBs), a commonly-used model for the cell membrane.

Firstly, this chapter employs evanescent wave cavity ring-down spectroscopy (EW-CRDS) to study the interfacial adsorption kinetics of coumarin-tagged macromolecules onto a range of planar surfaces, functionalised as models of the plant root/soil interface. Three tagged synthetic polymers with different functionalities are examined as possible root adhesives: polyacrylic acid (PAA), poly(3-sulfopropylmethacrylate, potassium salt) (PSPMA) and a mannose-modified glycopolymer.

Silica is chosen as a model surface for the inorganic fraction of the soil, poly-L-glutamic acid for the organic fraction of the soil and cellulose for the plant cell wall surface. The studies on silica are also performed with varying bulk pH, to manipulate the protonation level of the surface.

Adsorption transients at the silica/water interface are found to be characteristic for each polymer and kinetics are deduced from the initial rates. Complementary atomic force microscopy (AFM) imaging has been used for additional surface characterisation of adsorbed layers and functionalised interfaces to allow adsorption rates to be interpreted more fully. Adsorption rates for PSPMA and the glycopolymer are seen to be highly surface sensitive, with significantly higher rates on cellulose-modified surfaces, whereas PAA shows a much smaller rate dependence on the nature of the adsorption surface.

Secondly, EW-CRDS is advocated as a new approach for monitoring the formation of supported lipid bilayers (SLBs) on quartz substrates *in situ* and for the study of molecular adsorption kinetics at the resulting modified biomimetic surface. This approach is illustrated using SLBs of 1,2-dioleoyl-3-trimethylammonium-propane (DOTAP). Complementary atomic force microscopy (AFM) measurements confirm the formation of bilayers on quartz. The subsequent interaction of the anionic porphyrin, 5,10,15,20-tetraphenyl-21H, 23H-porphine-p,p′,p″,p‴-tetrasulfonic acid tetrasodium hydrate (TPPS) with the cationic bilayer-modified silica surface is studied using EW-CRDS combined with an impinging-jet to deliver analyte to the surface in a well-defined manner. The adsorption of TPPS to the bilayer is found to be kinetically controlled and the adsorption rate constant is found to be $1.7\ (\pm\ 0.6) \times 10^{-4}$ cm s^{-1} in a first-order surface process describing adsorption. These proof-of-concept

studies provide a platform for the investigation of molecular processes at biomembranes using EW-CRDS, including the adsorption of ions, peptides and proteins.

3.1 Introduction

Understanding adsorption processes of both synthetic and biological macromolecules at interfaces is important for a great number of technologies and the development of new materials, spanning coatings, methods for colloid stabilisation, reinforced plastics and surfaces which are relevant to, or encourage, bioadhesion, amongst a wide range of possibilities.[1-4] Fundamental studies of the adsorption of macromolecules, both in their free form and in micro- and nano-structures, are valuable for elucidating particular polymer properties which influence the mobility, adhesion and ordering in polymer-adsorbed layers.[5] A large variety of surface sensitive experimental techniques are currently used for such studies, as discussed in Chapter 1.

Here, evanescent wave cavity ring-down spectroscopy (EW-CRDS) is demonstrated as a powerful approach to study the adsorption kinetics of polymers from bulk solution onto planar surfaces. The studies herein are the first on macromolecule adsorption and, furthermore, demonstrate

further that the range of surfaces amenable to study can be diversified readily by chemical modification of the quartz prism.

The silica surface and silica/aqueous interface is much studied as it is common to many materials such as glasses, sands and oxidised silicon, and as such has been well-characterised. In the context of this study, this provides a useful model for the inorganic fraction of soil. Recent EW-CRDS studies[6-8] have evaluated the complex surface chemistry of planar silica in detail using the crystal violet cation adsorption as a probe. As first reported by Ong *et al.*,[9] the silica surface exhibits two distinct types of silanol group; an isolated type with a pK_a value of 4.9 and a surface population of *ca.* 19% and a vicinal type with a pK_a value of 8.5 and surface population of *ca.* 81%. The term 'isolated' here refers to silanol groups unable to form hydrogen bonds with neighbouring groups either directly or via bridging water molecules. The overall density of silanol groups on the silica surface is known to be ~4.9×10^{14} cm^{-2} giving ~9.3×10^{13} cm^{-2} isolated groups which can be further subdivided into type I and type II groups (based on degree of isolation) with respective densities of ~1.05×10^{13} cm^{-2} and ~8.2×10^{13} cm^{-2}.[10] This knowledge of the surface chemistry and the ability to manipulate this by alteration of the solution pH makes silica an insightful surface to study the adsorption of complex macromolecules.

A further powerful feature of the EW-CRDS technique is the ease with which the silica surface can be modified with a variety of thin films

and nanostructured materials such as polyelectrolyte films and bilayers.[11-13] Indeed, the scope for functionalizing the prism surface is broad and encompasses any species that can be deposited onto silica (or subsequently onto layers previously adhered to the silica surface) provided it does not significantly affect the ring-down time. Herein, we expand adsorption studies to our mimetic chemical surfaces which are also of broad interest to other fields. As mentioned above, cellulose is chosen as the model cell wall surface and deposition of regenerated thin films of cellulose for scientific studies are proving increasingly popular.[14] Chemically, cellulose is a linear polymer of *β-D*-glucopyranose with a large number of hydroxyl groups present (three per repeat unit) and provides an adhesion surface of great interest due to the presence in plant cell walls and the many industrial (cellulosic) derivatives.[15] Thin films of cellulose provide an interesting model substrate for studying adhesion characteristics to the wide range of cellulosic materials: these can be made by either spin-coating via solvent systems or cellulosic derivatives followed by regeneration,[16] or Langmuir-Blodgett (Schaefer) deposition of a derivative followed by regeneration.[17] The Langmuir-Blodgett transfer here is generally found to give a smoother film especially in very thin films (<20 nm).[14] These films are also found to be highly optically transparent, allowing sensitive optical measurements to be performed through them.

An interesting counterpoint to this cellulose functionalisation and the silica surface chemistry is provided by an acidic functionality which

can be formed trivially by the adsorption of high molecular weight polyelectrolytes,[11] in this case in the form of poly-L-glutamic acid (PGA). This provides the mimetic surface for the organic fraction of soil, which in nature is comprised of humic and fulvic acids; complex mixtures of aliphatic and aromatic carboxylic acids.

The focus herein is the use of EW-CRDS to study the adsorption of three tagged polymers with different functional groups to this range of surfaces. EW-CRDS is demonstrated as an insightful and versatile tool to elucidate the adsorption kinetics of macromolecules as a function of bulk pH on silica, and subsequently on modified surfaces. Characteristic adsorption transients are recorded for each polymer and kinetic data (rate constants) are extracted for the initial part of the adsorption process.

Polymers exhibiting carboxylic acid, sulfonate and sugar (mannose) functionalities were chosen for study in the form of poly(acrylic acid), poly(3-sulfopropylmethacrylate) and a mannose-modified glycopolymer, respectively. A single coumarin tag (incorporated as the initiator) served as an optical probe for each macromolecule, ensuring reasonable optical absorbance at the wavelength used (405 nm) in our EW-CRDS set up. The repeat units show, respectively, a single carboxylic acid side group, a sulfonate salt side group and a mannose side group. In considering the adsorption of these molecules to surfaces multiple binding routes are possible: the carboxylic acid chain gives a highly linear polyelectrolyte-type chain with minimal steric effects whereas the sulfonate group is larger

and on a longer side chain. The glycopolymer displays the bulkiest modification with the multiple hydroxyl groups on the mannose ring facilitating multiple hydrogen bonding opportunities. Both the sulfonate and glycopolymer will be little affected by bulk pH, whereas the PAA will become increasingly protonated at low pH. The studies herein allow an assessment of the impact on kinetics and extent of adsorption of the functionalities displayed by the macromolecules considered.

In the second part of this chapter, the possibility of using EW-CRDS to study the formation of, and subsequent adsorption to, supported lipid bilayer membranes (SLBs) is examined. The first demonstration of a planar phospholipid bilayer by Mueller *et al.* in 1962,[18] since then biomembrane mimics have received considerable attention for fundamental studies of biophysical processes. Solid-supported lipid bilayers (SLBs) are particularly attractive, as they constitute a robust platform, to which various techniques can be applied. SLBs have consequently been used extensively as models for cellular membranes.[19,20] This inner cell membrane provides a second surface of interest to the cell wall, particularly if uptake to the cell is considered. The focus herein is on SLBs formed using cationic phospholipids,[21] which have received considerable attention due to their applicability to a range of processes.[22-25] The methodology should, however, be widely applicable to many types of SLBs.

Popular methods used to form SLBs include the vesicle fusion method (VFM),[26] Langmuir-Blodgett and Langmuir-Schaefer techniques[27,28] and, to a lesser extent, spin coating[29,30] and air bubble collapse.[31] The principle behind the VFM is that, under appropriate conditions, small unilamellar vesicles (SUVs) of phospholipids in solution adsorb to a solid substrate and subsequently rupture (either instantly or once a critical surface coverage has been achieved) to form a bilayer on the substrate. Quartz crystal microbalance with dissipation (QCM-D) is a particularly well-established technique to follow the kinetics of SLB formation via the VFM.[32-39] Surface plasmon resonance (SPR),[33,37] atomic force microscopy (AFM), [35,36,40] attenuated total reflectance infrared spectroscopy,[41] ellipsometry[36] and fluorescence[37] have also been used to follow the formation of SLBs. However, the use of a single technique to both characterize the formation of SLBs and measure adsorption to the resulting surface is largely limited to QCM-D systems combined with flow modules. Even so, fast adsorption rates are not generally monitored via QCM-D; even with ellipsometry only mass-transport controlled adsorption has been monitored on a more rapid timescale.[42] Quantification of rapid binding kinetics of biologically-relevant species to SLBs is an important aspect of SLB research. The ability to unambiguously prove SLB formation and measure rapid and sensitive adsorption kinetics of biologically-relevant species to this surface *in situ* represents an ideal experimental configuration for SLB studies. We show that this is indeed the case and, significantly, that the EW-CRDS signature during SLB

formation on quartz is highly characteristic. Furthermore, once the SLB is formed, the same set-up can be used quickly and easily to follow physicochemical processes at the SLB, as demonstrated through studies of the binding kinetics of the anionic porphyrin TPPS to the SLB. The approach described herein is thus potentially broad in scope for studying SLB processes.

3.2 Experimental

3.2.1 Synthesis

Polyacrylic acid (PAA, **(I)**), poly(3-sulfopropylmethacrylate, potassium salt) (PSPMA, **(II)**) and mannose-modified glycopolymer **(III)** were provided by Dr Anne de Cuendias. The structures of the resulting polymers are shown in Figure 3.1 and physical properties are summarised in Table 3.1. Molecular weights used for adsorption experiments were calculated by integration of the proton NMR peaks.

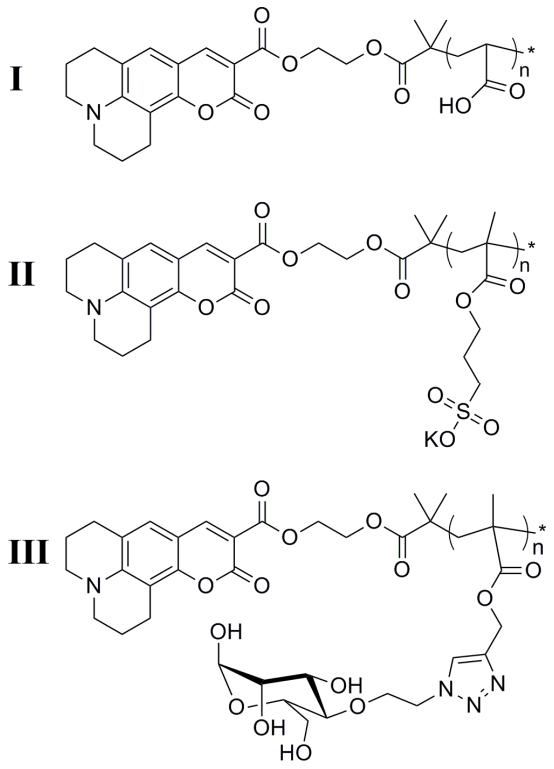

Figure 3.1. Structures of the coumarin-tagged synthetic polymers used in adsorption experiments.

Table 3.1. Physical characteristics of the polymers used in this study.

Polymer	M_n / g mol^{-1} (from NMR)	Degree of Polymerization	Extinction coefficient @ 405 nm / dm^3 mol^{-1} cm^{-1}
I, PAA	8100	105	4730
II, PSPMA	14000	54	539
III, mannose-modified glycopolymer	22200	58	10350

3.2.2 Chemicals

Acetic acid, sodium acetate, sodium monophosphate, sodium diphosphate, sodium borate and boric acid used for buffer preparation were bought from Sigma-Aldrich. Poly-L-lysine (PLL, MW 30,000-70,000), poly-L-glutamic acid (PGA, MW 50,000-100,000) and cellulose used for surface modification were also purchased from Sigma-Aldrich. All solvents used for cleaning of the prism surface were used at the highest purity available.

1,2-dioleoyl-3-trimethylammonium-propane (DOTAP) was purchased as the chloride salt from Avanti Polar Lipids and stock solutions were prepared and stored in chloroform at -20º C. 5,10,15,20-tetraphenyl-21*H*, 23*H*-porphine-*p*,*p*′,*p*″,*p*‴-tetrasulfonic acid tetrasodium hydrate (TPPS, shown in Figure 3.2) was purchased from Sigma-Aldrich and solutions were prepared immediately prior to experiments. All experiments were performed in a buffer solution (Buffer A) consisting of 150 mM NaCl (Fisher Scientific), 10 mM HEPES (Fluka), 2 mM NaN_3 (Sigma), 2 mM EDTA (Aldrich) and adjusted to pH 7.4 using NaOH (Sigma-Aldrich). Ultrapure water was obtained from a Milli-Q plus 185 system from Millipore (resistivity of 18.2 MΩ cm at 25ºC).

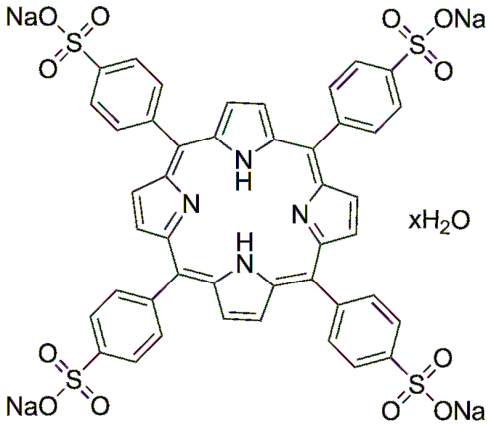

Figure 3.2. Structure of TPPS.

3.2.3 EW-CRDS apparatus and adsorption experiments

The EW-CRD spectrometer is described fully in Chapter 2.1. A cell body was mounted on the hypotenuse of the prism and filled with polymer solution to create a solution/surface interface. The prism was wetted slightly prior to experiments to (a) allow optimization of the ring-down time and (b) ensure any adsorbed layers were fully hydrated. The characteristic ring-down time was measured as a function of time immediately after addition of the solution used. Data obtained (the characteristic ring-down time, τ, as a function of time) were smoothed by using 50-point adjacent averaging.

3.2.4 EW-CRDS polymer adsorption experiments

Extinction coefficients (molecular absorption coefficient) were derived from UV-VIS spectroscopy (Lambda 25 UV Visible Spectrometer, Perkin-Elmer Instruments). Between each experiment the prism was wiped with methanol, treated with oxygen plasma for 3 minutes at 100 W (Emitech, K1050X) and wiped again with methanol. This resulted in the prism being returned to a clean state, as confirmed periodically by recording the background ring-down time, τ_0, for a clean prism surface. Solutions were buffered at pH 4.8, 7.0 and 9.0 using solutions of acetic acid/sodium acetate, sodium monophosphate/sodium diphosphate or sodium borate/boric acid respectively all at 10 mM concentration. All aqueous solutions were made using Milli-Q grade purified water (Millipore Corporation).

3.2.5 PGA surface functionalisation

Poly-L-lysine (PLL) solution (1 mg/ml) was drop-coated onto the top surface of the silica prism and left to adsorb for 20 minutes. The surface was then rinsed with ultra pure water (Millipore) and dried under a stream of N_2. Poly-L-glutamic acid (PGA) solution (1 mg/ml) was then drop-coated onto the PLL-modified surface and left to adsorb for 20 minutes, rinsed with ultra pure water and dried under a stream of N_2. A typical AFM image of a resulting surface is shown in Figure 3.3 (b) with

the initial quartz surface (a) shown for comparison. This modification resulted in a small reduction in τ_0 of typically 20 ns compared to the bare silica surface (~320 ns).

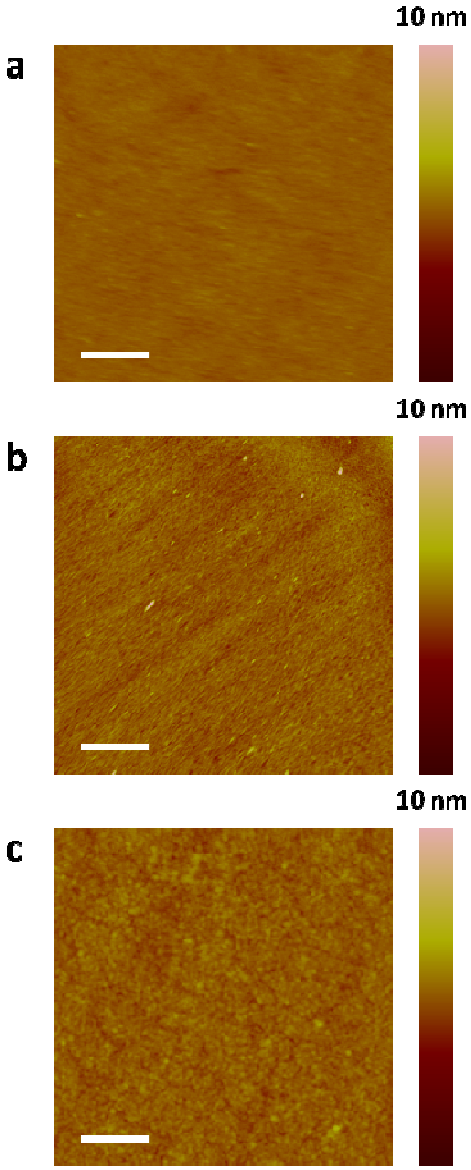

Figure 3.3. TM-AFM images showing (a) the bare silica surface, (b) PLL/PGA bilayer and (c) regenerated cellulose thin film deposited onto silica surfaces. Scale bars denote 1 µm for (a) and (b), and 200 nm for (c).

3.2.6 Cellulose surface functionalisation

Trimethylsilyl cellulose (TMSC) was synthesized by the method described by Schaub *et al.*[17] The silica prism surface was made hydrophobic by drop-coating with dichlorodimethylsilane and washing with copious amounts of propan-2-ol (IPA). TMSC was then dissolved in chloroform (0.5 mg/ml) and the solution deposited dropwise onto the water surface of a Langmuir trough (NIMA Techology). The monolayer was compressed to typically 25 mN cm^{-2} and layers transferred to the hydrophobic prism surface via the Langmuir-Schaefer technique. The TMSC multilayers were then converted back into cellulose by exposure to concentrated HCl fumes for 30 s. The regeneration of cellulose was deemed to be complete following a change in the hydrophobicity of the surface, shown by the change in the static contact angle of water with the surface from ~70-75˚ for TMSC to ~30-35˚ after regeneration which is in good keeping with literature values.[16,43] Figure 3.3 (c) shows the cellulose-modified surface comprising of 5 layers of cellulose which was found to give complete surface coverage whilst maintaining measurable ringdown times (*ie* > 50 ns). This surface produced a larger reduction in τ_0 of typically ~100 ns leading to a small increase in noise levels on subsequent measurements. Nevertheless, as we show herein, convincing adsorption measurements could subsequently still be made readily.

3.2.7 AFM of polymer films and layers

AFM imaging was undertaken using a Bruker Multimode V AFM equipped with Nanoscope V controller operated in tapping mode (TM-AFM) using standard silicon tapping mode tips (RFESP or RTESP type, Bruker Probes). Polymer solutions and surface modifications (PLL/PGA and cellulose) were deposited onto highly polished polycrystalline quartz substrates (Hoffman Materials) which had been treated with oxygen plasma and wiped with methanol using identical conditions as for the silica prism (*vide supra*).

3.2.8 SUV preparation

Part of the stock solutions of DOTAP was dried in a nitrogen stream and vacuum desiccated for at least 4 hours to remove the chloroform. The lipids were then resuspended in buffer A to a concentration of 0.1 mg mL^{-1}, sonicated for 2 minutes to ensure complete resuspension, freeze-thawed five times, before finally being extruded through 100 nm polycarbonate membranes (GC Technology). SUV solutions were used within 4 hours of preparation.

3.2.9 Monitoring SLB formation using EW-CRDS

The EW-CRDS set-up and impinging jet system used is shown schematically in Figure 2.2 and is described in detail in Chapter 2.2. The background ring-down time, τ_0, was recorded with buffer in the cell. The buffer was removed and the EW-CRDS signal recorded as a function of time as 500 µl of SUV solution was dropped into the cell using a plastic pipette. The resulting SLB formed from the DOTAP solution was rinsed using the impinging jet set-up. The nozzle-prism separation was chosen to be 500 ± 100 µm, giving well defined hydrodynamics,[44] and ensuring that the nozzle did not penetrate the evanescent field (extending into the solution < 1µm) from the quartz prism. 10 mL of buffer A was flowed over the SLB at a rate of 0.5 mL min^{-1} using a syringe pump to ensure complete removal of the SUVs in solution and to check the stability of the SLB (via the EW-CRDS response) under these flow conditions. Between experiments the prism surface was cleaned by exposure to oxygen plasma at 100 W for 3 minutes followed by wiping with methanol, ensuring t_0 returned to the initial value.

3.2.10 AFM of DOTAP SLB formed on quartz

Single crystal quartz wafers (Hoffman Materials, Inc.) were cleaned by sonicating in acetone for 5 minutes, rinsing with isopropanol, followed by exposure to oxygen plasma at 100 W for 3 minutes. 100 µl of 0.1 mg

mL^{-1} DOTAP SUV solution was pipetted on top and left to adsorb for 15 minutes. The surface was then washed using 3 mL of buffer A and kept under solution for tapping mode-atomic force microscopy (TM-AFM) imaging. Topographical images of the surface were obtained using a Bruker Enviroscope AFM at a resolution of 512 by 512 pixels at 0.5 Hz, using the 'short thin' and 'short thick' cantilevers of NP-type silicon nitride probes with k (nominal) of 0.32 and 0.58 Nm^{-1} respectively and f_0 of 40-75 kHz. Actual imaging frequencies used in solution represent approximately one third of the stated value of f_0. For deliberate disruption of SLB experiments, contact mode (CM-AFM) was used by applying a force greater than for standard imaging, of typically 100-150 nN.

3.2.11 EW-CRDS of TPPS on SiO_2 and SLB-modified SiO_2

The background ring-down time with just 500 µl buffer A in the cell was measured initially. Then, to determine if TPPS adsorbed to the silica surface, the EW-CRDS signal was recorded as 500 µl of 10 µM TPPS in buffer A was pipetted directly onto the prism surface. Finally, the EW-CRDS signal was recorded as TPPS solution (concentrations: 0.5 µM, 1 µM, 2 µM, 3 µM, 4 µM and 5 µM) in buffer A was flowed over SLB-modified prisms using the impinging jet cell. A fresh SLB was used for each measurement. The flow rate was 0.5 mL min^{-1} and the nozzle-prism separation was 500 µm.

3.2.12 QCM-D of DOTAP Adsorption at SiO_2

QCM-D measurements were made using a Q-Sense E4 QCM-D with a Q-Sense Flow Module. SiO_2 coated AT-cut quartz crystals (f_0 = 4.95 MHz, Q-Sense) were cleaned by flowing 10 mg mL^{-1} sodium dodecyl sulfate (Fluka) over the surface for 20 minutes, followed by ultrapure H_2O (Millipore) for 1 hour, both at 0.2 mL min^{-1}. They were then dried in a stream of nitrogen before being exposed to oxygen plasma for 3 minutes at 100 W (Emitech, K1050X). Once mounted in the flow module, buffer was flowed over the sensor crystal at 10 µl min^{-1} until a stable baseline was achieved. The change in frequency and dissipation were recorded as SUV solution was flowed over the sensor crystal at 10 µl min^{-1}. After the signal had stabilised, the bilayer was rinsed by flowing buffer over the crystal surface at 10 µl min^{-1}. All solutions were sonicated for 2 mins prior to introduction to the QCM-D to remove air bubbles.

3.3 Results and Discussion

3.3.1 UV-visible absorption spectroscopy of functionalised polymer molecules

Figure 3.4 shows the UV-Vis spectra used to determine the extinction coefficient at 405 nm for each macromolecule used in EW-

CRDS adsorption experiments. Note here the significantly higher concentration necessary for **(II)** (1 mM) compared to **(I)** and **(III)** (50 μM) to provide a measurable spectrum. The polymerization has clearly affected the coumarin peak (λ_{abs} max @ 443 nm in its native form) strongly for **(I)** and (particularly) **(II)**. However, the optical absorption at the wavelengths measured here is fairly broad, and is easily sufficient for EW-CRDS measurements using a 405 nm diode laser.

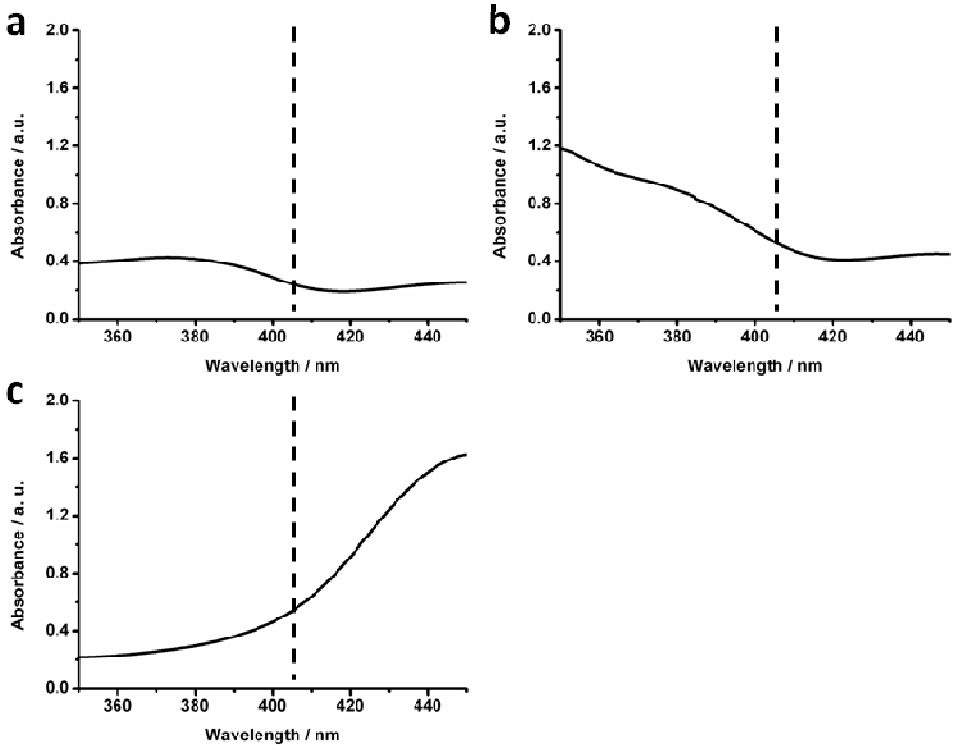

Figure 3.4. UV-vis spectra of (a) (I) at 50 μM, (b) (II) at 1 mM and (c) (III) at 50 μM. Note the considerably higher concentration of (II). EW-CRDS measurements are made at 405 nm (indicated by dashed line).

3.3.2 Polymer adsorption experiments on silica

EW-CRDS was first considered on the silica substrate and adsorption was monitored over a time period of one hour. The adsorption *vs*. time behavior of each polymer on silica was found to be characteristic. The EW-CRDS transient in Figure 3.5 (a) (i) shows a relatively rapid initial rate of adsorption of 1 mM **(I)** at pH 7.0 onto silica which slows with time to give a limiting surface concentration (after ~2500 s) of ~5.0 x 10^{-10} mol cm^{-2}. Note that this surface concentration, and all subsequent macromolecule surface concentrations, are defined in terms of tag concentration, *i.e.* that of an individual macromolecule, which contains a single tag with molecular weight based on M_n (from NMR). The shape of this transient appears to reflect simple adsorption behaviour with vacant surface binding sites being occupied until a limiting value is reached, although the surface concentration is undoubtedly high if considering a single monolayer.

The high number density of molecules at equilibrium could indicate close packing of macromolecules; this would be facilitated by the low steric demands of the PAA chain and the acidic groups forming a vertical polyelectrolyte brush, which is reasonable considering PAA is a weak polyelectrolyte (pk_a ~4.5) which is essentially totally deprotonated at pH 7.0 and the molecule studied has a fairly low M_n (of 8100 g mol^{-1}). The corresponding TM-AFM image of the adsorbed layer deposited under identical conditions (Figure 3.5 (a) (ii)) shows an apparently smooth layer

with a low coverage of additional small particles on the surface. The particles visible are likely due to a small degree of aggregation of molecules which may partially explain the high (calculated) surface concentration of molecules. These observations (and those for subsequent macromolecules and surfaces) are discussed further in the kinetics section.

In stark contrast, polymer **(II)** again at pH 7.0 shows approximately linear adsorption over the time period studied (Figure 3.5 (b) (i)), meaning the observed initial rate of adsorption on silica is maintained at a constant value over a much longer timescale. Coincidentally, the surface coverage at 1 hour (~5.5 x 10^{-10} mol cm^{-2}) is of a similar order to that of **(I)**, but there is no indication of an equilibrium being established. As there is no suggestion of preferential binding to particular sites on this surface, it can be assumed that the polymer has no preference for the silica surface and that multilayer adsorption occurs. AFM analysis of the adsorbed layer (Figure 3.5 (b) (ii)) supports this, showing a continuous, smooth film with no indication of particles or aggregates on the surface.

Investigations of **(III)** were limited mainly by its lower (molar) solubility (due to its higher molecular mass). As such, concentrations an order of magnitude lower compared to **(I)** and **(II)** were used, *i.e.* 0.01 – 0.1 mM compared to 0.1 – 1 mM. The adsorption transient on Figure 3.5 (c) (i) shows an initially fast, but rapidly slowing, adsorption rate where equilibrium surface coverage is not reached after one hour. At all concentrations studied, **(III)** had not reached equilibrium surface coverage

within this timescale, including for the same concentration as **(I)** (0.1 mM) which would indicate the binding mechanism is either different, or on a much longer characteristic timescale, to that of **(I)**. It is also clear from AFM analysis of the adsorbed layer (Figure 3.5 (c) (ii)) that a large number of particles are present on the surface in contrast to **(I)** and **(II)**.

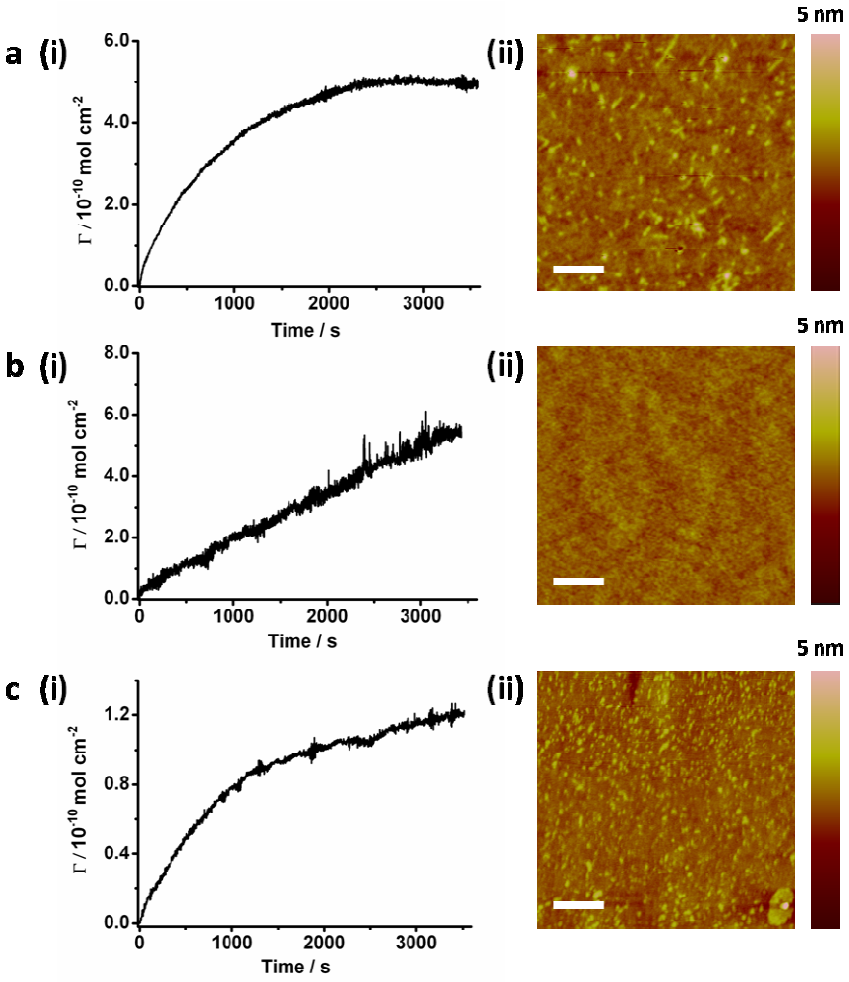

Figure 3.5. Typical EW-CRDS surface concentration, *Γ*, *vs*. time plots at pH 7.0 with TM-AFM characterization of the resulting surface. (a) (i) I at 1 mM concentration, (b) (i) II at 1 mM concentration and (c) (i) III at 0.1 mM concentration. (a) (ii), (b) (ii) and (c) (ii) show the structure of the adsorbed layer. Scale bars denote 200 nm.

3.3.3 Adsorption transients on PGA and cellulose

Turning to cellulose and PGA, again at pH 7.0, **(I)** shows similar adsorption *vs.* time behaviour (Figure 3.6 (a)) to silica for both additional surfaces, except that on cellulose an apparent surface equilibrium has not been reached after the one hour timescale. The equilibrium surface coverage for 1 mM bulk concentration (**I**) at pH 7.0 for both PGA and silica is similar at around 5.0 x 10^{-10} mol cm^{-2} whereas surface coverage for cellulose is a little higher (~7.0 x 10^{-10} mol cm^{-2}) and rising. Evidently the higher number of surface binding sites on cellulose compared to silica is a major factor (given the similar extent of adsorption).

Again in stark contrast, it is clear from Figure 3.6 (b) that the adsorption behavior of **(II)** is highly dependent on the surface, with a significant difference between PGA and cellulose, and the comparison on silica (Figure 3.5 (b)). Adsorption on PGA shows a linear surface coverage *vs*. time plot, as for the silica surface, but with a lower rate (~2.0 x 10^{-10} mol cm^{-2} after 1 hour), whereas the cellulose surface results in an initial fast adsorption step followed by linear adsorption *vs*. time behavior but also much more rapid adsorption (~1.3 x 10^{-9} mol cm^{-2} after 1 hour).

The adsorption *vs*. time behaviour for **(III)** on each surface followed the trend of rapid initial, but slowing, adsorption. However, it is clear that PGA significantly inhibited surface adsorption (by an order of magnitude), when surface concentrations after 1 hour are considered, compared to silica and cellulose (~1.5 x 10^{-11} mol cm^{-2} for PGA compared

to ~1.2 x 10^{-10} mol cm^{-2} for silica and ~1.3 x 10^{-10} mol cm^{-2} for cellulose, respectively).

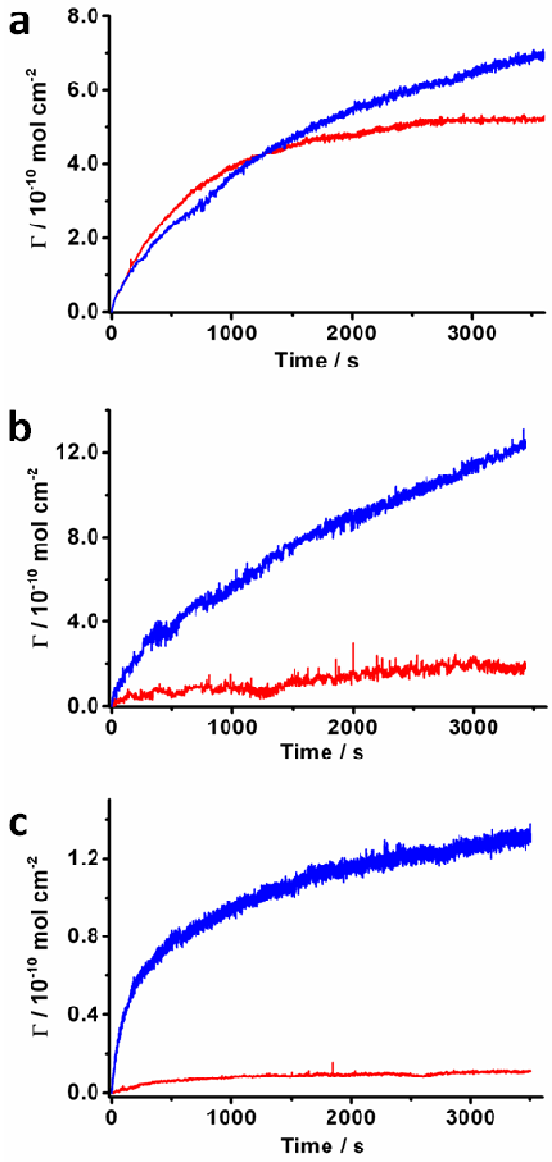

Figure 3.6. Typical EW-CRDS surface concentration, *Γ*, vs. time plots at pH 7.0 for PGA and cellulose for (a) I at 1 mM concentration, (b) II at 1 mM concentration and (c) III at 0.1 mM concentration. The transient obtained for PGA is shown in shown in red and cellulose in blue.

3.3.4 Reversibility

Desorption was also investigated with simple experiments to determine if the adsorption of each polymer to each surface was reversible. Adsorption was deemed to be reversible if, after removal of the polymer solution and introduction of buffer, the ringdown time returned (close) to its original value. The change was generally seen to be instantaneous due to the mechanical washing effect and therefore no attempt was made to measure desorption rates. For consistency the buffer was changed 3 times and a return to within 10% of the original τ is deemed (reasonably) to be reversible. Irreversible adsorption was characterised by no significant change in τ on washing. Observations, which were found to be consistent across pH and concentration ranges, are summarised in Table 3.2.

Table 3.2. Observations of reversiblity based on washing of prism surface post-experiment.

Polymer	Silica	PGA	Cellulose
I	Reversible	Reversible	Reversible
II	Reversible	Reversible	Non-Reversible
III	Non-Reversible	Non-Reversible	Non-Reversible

Significantly, (**I**) was found to bind reversibly to all surfaces and (**III**) irreversibly to all surfaces, but (**II**) varied with surface; binding was reversible on silica and PGA, but irreversible on cellulose to which it adsorbed both more rapidly and in a non-linear fashion (*vide supra*). The

reversible binding of **(I)** provides further evidence that a surface equilibrium is reached, whereas for **(III)** this is clearly not the case despite a (superficially) similar adsorption *vs.* time shape. Evidently, the sugar functionality promotes stronger surface binding. **(II)** provides an intermediate case; it is only irreversible on the hydroxyl-rich sugar polymer cellulose. However, the similarly negatively-charged PAA **(I)** is reversible on this surface, with the ester linkage on the sulfonate side chain on **(II)** evidently providing sufficient H-bonding with cellulose to cause irreversible adsorption.

3.3.5 Evaluation of adsorption kinetics

Data such as these in Figures 3.5 and 3.6 allow the initial adsorption rate k_i, *ie* for $t < 100$ s, to be deduced. Focusing on this timescale is interesting because it reveals the adsorption kinetics on a fresh surface. Given the concentration used and timescale for adsorption, it is reasonable to assume the process is surface controlled, *i.e.* there are no diffusional effects. For first-order interfacial kinetics the following rate law thus holds:

$$\left[\frac{d\Gamma}{dt}\right]_{t=0} = k_i c \qquad (3.1)$$

where k_i is an initial rate constant with units of cm s^{-1}. The initial part of each adsorption *vs.* time transient at a series of different concentrations, are

thus fitted linearly to extract the initial adsorption rate, which are then plotted against bulk concentration to elucidate k_i.

3.3.6 Effect of bulk pH on adsorption kinetics to silica

Rate constants were determined from plots of initial adsorption rate *vs*. bulk concentration (Figure 3.7). pH values of 4.8, 7.0 and 9.0 were chosen to manipulate surface protonation levels (silanol groups with pK_a values of 4.9 and 8.5).[36] The linear fits of these plots indicate the assumption of first-order kinetics is reasonable. Rates for all kinetic experiments are summarized in Table 3.3 and plotted in Figure 3.8. The initial rate constants for **(I)** (Figure 3.7 (a)) show a systematic increase in binding rates in the order pH 4.8 < 7.0 < 9.0. The higher pH value promotes a faster adsorption rate especially when the silica surface is completely deprotonated (pH 9.0). Naively, this might have been expected to lead to electrostatic repulsion between the surface and polymer molecules, suggesting that the intermolecular forces dominate the adsorption process on silica, with electrostatic repulsion between polymer chains driving polyelectrolyte brush formation, which eventually reaches equilibrium surface coverage.

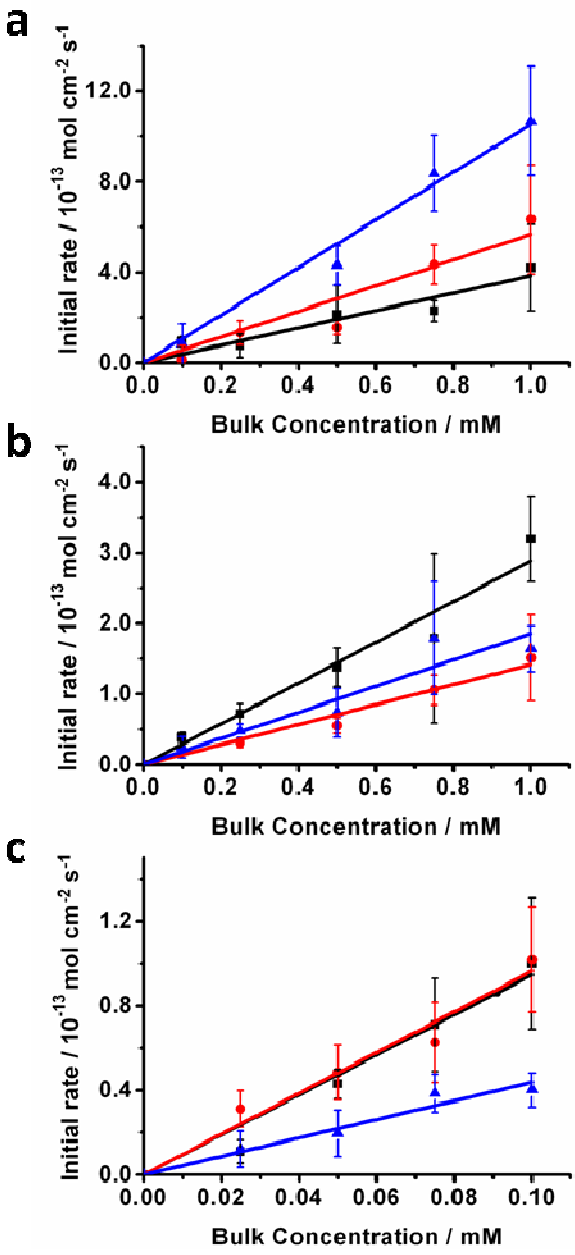

Figure 3.7. Kinetic plots of initial rate *vs*. bulk concentration for (a) I, (b) II and (c) III. The initial rate constant, k_i, is equal to the gradient of the linear fit. pH 4.8 is denoted in black, pH 7.0 in red and pH 9.0 in blue.

at much longer timescales. Conversely, at pH 4.8 **(I)** (as a weak acid of pk_a ~4.5) will become partially protonated, thus reducing electrostatic repulsion (by lowering the charge density) between molecules and hindering (slightly) brush formation.

The initial adsorption kinetics for **(II)** (Figure 3.7 (b)) show a small change in adsorption rates in the order pH 4.8 > 9.0 > 7.0. These rates are all considerably lower than for **(I)** under the same conditions, highlighting that this polymer adsorbs more slowly at the silica surface at short timescales, as was evident when studying adsorption *vs*. time behavior over a longer time period (*vide supra*). The slightly higher binding at pH 4.8 is perhaps driven by less negative charge on the silica surface reducing electrostatic repulsion between the silica and sulfonate salt.

Initial adsorption kinetics for (**III**) (Figure 3.7 (c)) were very similar for pH 4.8 and 7.0 but around half that at pH 9.0. The mannose modifier on this polymer provides multiple hydrogen bonding opportunities and, coupled with the fact it is at the end of a comparatively long, bulky side chain, provides a likely binding route. This correlates with the decreased binding rate at pH 9.0 as the surface exhibits the highest degree of deprotonation and therefore the fewest hydrogen bonding sites. It is noted here that no drastic changes in initial adsorption rates were brought about by manipulating the chemistry of the silica surface for any of the macromolecules studied, with the largest variation of rate with pH around two times.

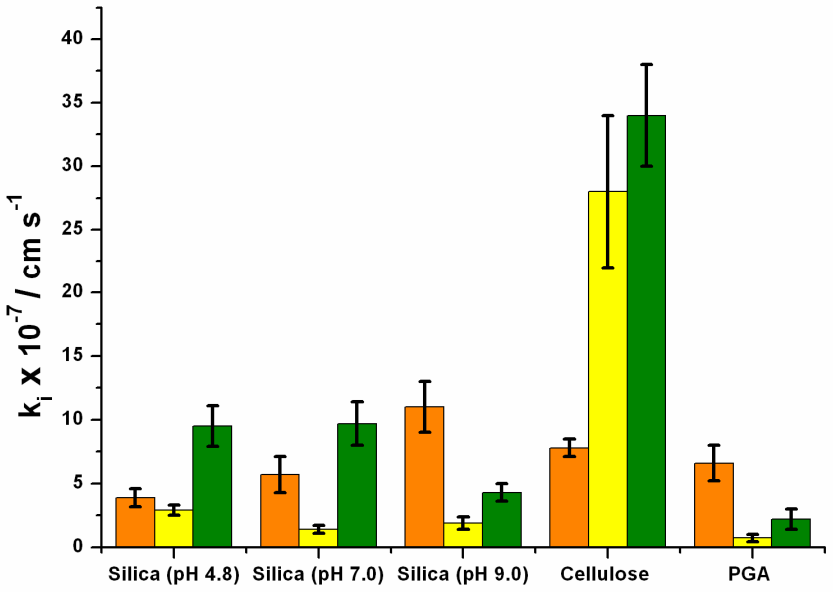

Figure 3.8. Summary of initial rate constants, k_i, for all of the surface chemistries studied. I is shown in orange, II in yellow and III in green.

Table 3.3. Summary of initial rate constants, k_i, for all of the surface chemistries studied.

	PAA (I)	**PSPMA (II)**	**Mannose-modified glycopolymer (III)**
Silica (pH 4.8)	3.9± 0.7 x 10^{-7}	2.9 ± 0.4 x 10^{-7}	9.5 ± 1.6 x 10^{-7}
Silica (pH 7.0)	5.7 ± 1.4 x 10^{-7}	1.4 ± 0.3 x 10^{-7}	9.7± 1.7 x 10^{-7}
Silica (pH 9.0)	1.1 ± 0.2 x 10^{-6}	1.9 ± 0.5 x 10^{-7}	4.3 ± 0.7 x 10^{-7}
Cellulose (pH 7.0)	7.8 ± 0.7 x 10^{-7}	2.8 ± 0.6 x 10^{-6}	3.4 ± 0.4 x 10^{-6}
PGA (pH 7.0)	6.6 ± 1.4 x 10^{-7}	7.3 ± 2.8 x 10^{-8}	2.2 ± 0.8 x 10^{-7}

3.3.7 Adsorption kinetics on modified surfaces at pH 7.0

Figure 3.9 shows kinetic plots used to calculate k_i for PGA and cellulose surfaces in the same manner as in Figure 3.7. The values are again summarized in Table 3 and Figure 3.8. The initial kinetics for **(I)** (Figure 3.9 (a)) at pH 7.0 show a marginally faster rate for cellulose compared to PGA. The effect of surface chemical functionalisation on the adsorption rate of **(I)** is clearly minor, which is consistent with the effect of manipulating bulk pH on silica (*vide supra*). The surface chemistries studied in this work clearly have little effect on the adsorption of **(I)** (PAA). Both the initial rates of adsorption and longer term studies give reasonably similar results across all surfaces and the conclusions made from the effect of manipulating silica surface chemistry hold for these further surfaces.

Figure 3.9 (b) shows the effect on surface functionalisation on the adsorption rate of (**II**). Here, the effect of surface chemistry on the initial rate is dramatic. The initial rate constant for adsorption to cellulose at pH 7.0 shows a large increase compared to the silica reference (*vide supra*). Conversely the PGA surface displays a significantly lower adsorption rate. These initial binding rates vary by a factor of 40 which is in stark contrast to **(I)**. The lower rate on PGA can be explained by electrostatic repulsion between the negatively-charged surface and sulfonate group on the polymer with virtually no binding sites available, whereas the hydrogen bonding between the polymer and cellulose massively increases this rate.

In comparison to these the manipulation of silica surface chemistry has relatively little effect, though the most protonated surface (at pH 4.8) does give the fastest rate of adsorption.

The initial adsorption rates of (**III**) (Figure 3.9 (c)) show a similar, though less drastic, trend as (**II**), with a clear increase in adsorption rate to cellulose and a decrease to PGA. The increase in adsorption rate to cellulose can again be reasonably considered to be due to increased hydrogen bonding, especially due to the multiple hydroxyl groups on the mannose-pendant group. The deprotonated PGA surface will prevent this hydrogen bond formation and thus decrease surface adsorption, which is consistent with the data in Figure 3.7 (c) where the lowest adsorption rate is for pH 9.0.

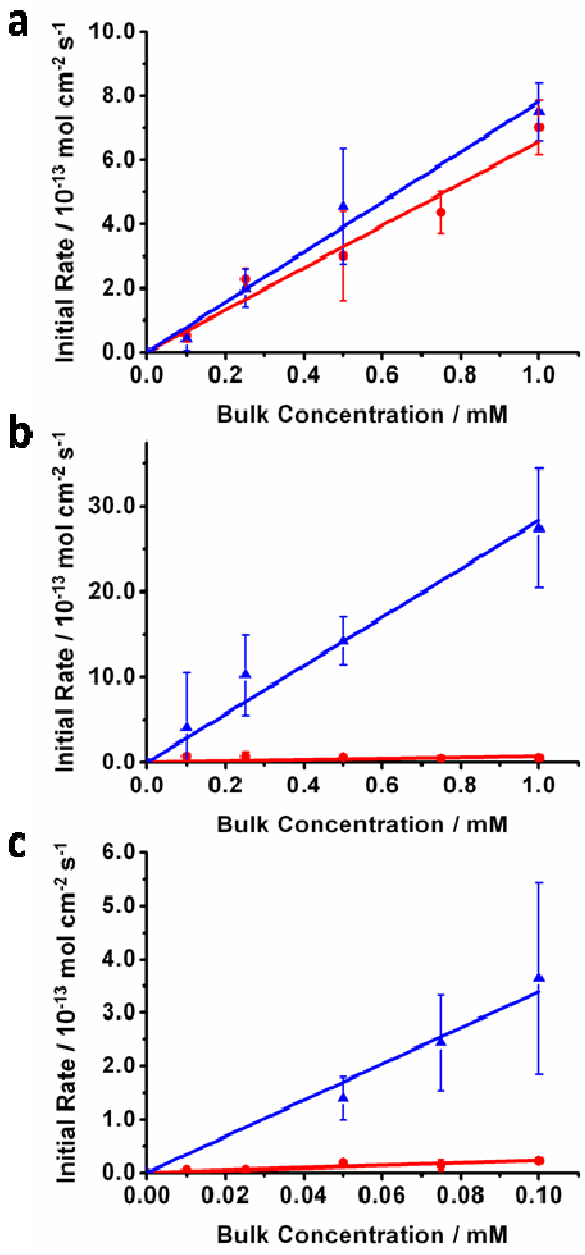

Figure 3.9. Kinetic plots of initial rate *vs*. bulk concentration for (a) I, (b) II and (c) III. The initial rate constant, k_i, is equal to the gradient of the linear fit. PGA is denoted in red and cellulose in blue.

3.3.8 SLB formation experiments

The second part of this chapter concerns the monitoring of formation of, and subsequent adhesion of species to, SLBs. As these layers are dynamic, the formation and use of these layers as mimetic surfaces is more complex than the previously-used mimetic surfaces. As such, the range of polymers was not studied. Instead a single, biologically relevant molecule, TPPS, was chosen for these proof-of-concept studies.

3.3.9 UV-visible absorption spectroscopy of SUV and TPPS

UV-visible absorption spectroscopy was used to determine the extinction coefficient at λ=405 nm, ε_{405}, as used in the EW-CRDS measurements. Spectra of 2 μM, 5 μM, 10 μM TPPS in buffer A are shown in Figure 3.10 (a). The main peak is at 413 nm for all three spectra and the absorbance is linear with concentration, indicating that the TPPS does not form aggregates at these concentrations. The inset of Figure 3.9 (a) shows the dependence of the absorbance at 405 nm on the TPPS concentration. A linear fit to the data gives $\varepsilon_{405} = 1.15 \times 10^5$ dm^3 mol^{-1} cm^{-1}.

The spectrum of 1 mg mL^{-1} DOTAP vesicle solution in buffer A (pH 7.4) is shown in Figure 3.10 (b). In this situation, the apparent optical absorbance is actually due to the combination of molecular absorbance and light scattering due to the SUVs (which dominates) and can be measured to give a combined 'extinction coefficient' which will hold providing the

SUVs remain intact. The optical extinction of a 1 mg mL^{-1} DOTAP SUV solution at 405 nm was measured to be 0.35 cm^{-1}. The combined extinction coefficient for DOTAP in SUV at 405 nm was then calculated using the Beer-Lambert law to give $\varepsilon_V^{405} = 2.45 \times 10^2$ dm^3 mol^{-1} cm^{-1}, which was considered to be reasonable for the SUV solutions of interest.

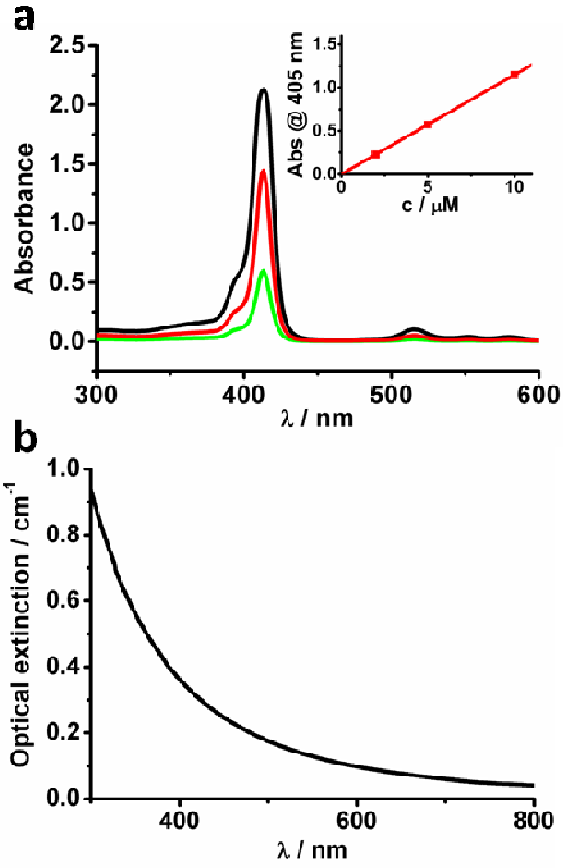

Figure 3.10. (a) UV-visible absorption spectra for 2 μM (green), 5 μM (red) and 10 μM (black) TPPS in buffer A. Inset: Optical absorbance at 405 nm plotted against TPPS concentration. The line of best fit gives $\varepsilon_{405} = 1.15 \times 10^5$ dm^3 mol^{-1} cm^{-1}. (b) UV-visible spectrum of 1 mg mL^{-1} DOTAP in buffer A (pH 7.4).

3.3.10 Probing SUV adsorption and SLB formation using EW-CRDS

Figure 3.11 shows the EW-CRDS response upon the introduction of 0.1 mg mL^{-1} DOTAP SUV solution to the prism surface. As the modification of the ringdown time is due to scattering by SUVs at the prism/aqueous interfaces, we term the modified ringdown time as an optical loss due to scattering. There was initially an increase to a value of 1.7×10^{-4} after 16 s and then a decrease to 1.5×10^{-5} after 60 s. The initial rise can be attributed to the adsorption of SUVs at the prism surface (a in Figure 3.11) which would be expected to scatter light in the evanescent field. Thereafter, the trend in the magnitude of the optical loss can be explained by the rupturing of surface-adsorbed vesicles to form a SLB (b in Figure 3.9). The low final value of the EW-CRDS response, combined with the AFM data (*vide infra*), suggests that the bilayer is uniform with few or no vesicles still intact (c in Figure 3.11).

Assuming that the critical adsorbed concentration of the lipid in the SUVs is the same as the concentration of lipids in the SLB, the molecular surface concentration can be calculated from the combined extinction coefficient to give 6.9×10^{-10} mol cm^{-2} at the peak in time-dependent EW-CRDS signal in Figure 3.11. Assuming a continuous bilayer is formed containing all the lipid molecules from the SUVs detected by EW-CRDS, this gives a surface area per molecule of 48 $Å^2$ for the lipid in the final bilayer, which is in good agreement with previous QCM-D studies (for

example, Keller *et al.* determined the area per molecule to be 55 Å^2 for an EggPC SLB[32]).

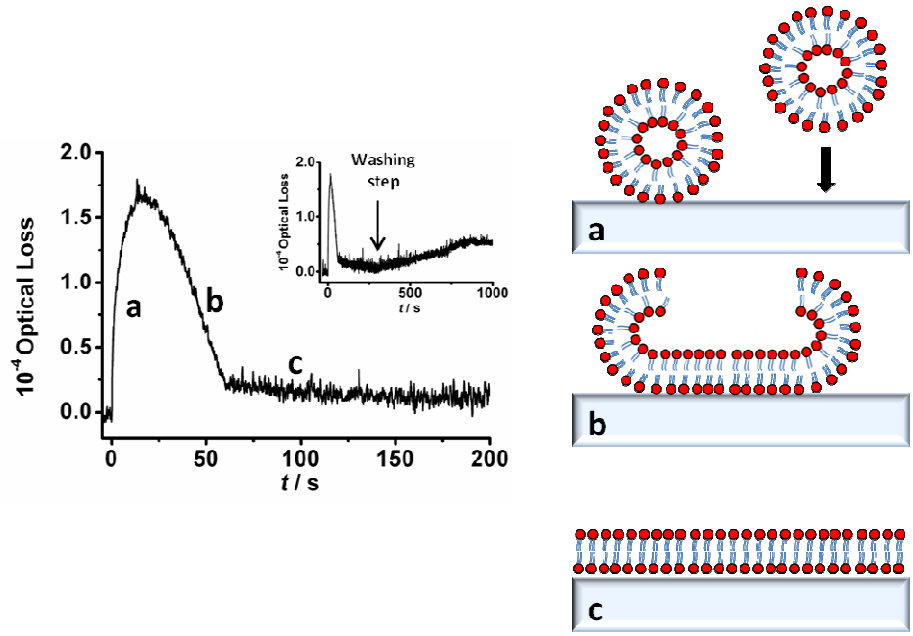

Figure 3.11. Formation of DOTAP SLBs: EW-CRDS response to the addition of 0.1 mg mL^{-1} DOTAP in buffer A (pH 7.4) to the prism surface, showing (a) accumulation of SUVs at the surface (0-16s), (b) fusion of the SUVs (16-60 s) and (c) complete bilayer formation (>60 s). The inset shows the response over a longer time during rinsing of the bilayer with buffer A using the flow cell, with rinsing commencing at *t* = 300 s. Cartoons shown not to scale.

To remove excess vesicles from the cell, 5 mL of buffer A was flowed over the surface in the impinging jet cell arrangement with a flow rate of 0.5 mL min^{-1} and a nozzle-prism separation of 500 µm. The inset of Figure 3.11 shows the optical loss obtained from EW-CRDS over a longer

time-period to show the response when buffer A was flowed over the surface, commencing at t = 300 s. There is initially no change in the optical absorbance (for *ca.* 100 s) and then a very gradual change of 3.1 × 10^{-5} over a period of 10 minutes, which could possibly be due to rearrangements or disruptions of the bilayer due to the shear force from the fluid flow. This behavior, however, takes place on a much longer timescale than the TPPS adsorption measurements reported below (which occurs over a few seconds). We thus conclude from these studies that a homogeneous and stable bilayer can be formed for EW-CRDS experiments with flow.

3.3.11 TM-AFM characterisation of SLBs

To determine the quality of the bilayer that had formed upon adsorption of DOTAP to silica, complementary *in situ* TM-AFM experiments were performed. SLBs were formed on single crystal quartz by adsorbing SUVs from 100 µl of 0.1 mg mL^{-1} DOTAP in buffer A for 15 minutes and then rinsing the surface with 3 mL of buffer A. A representative *in situ* TM-AFM image of the surface is shown in Figure 3.12 (a) which is similar to the images obtained in previous reports.[35]

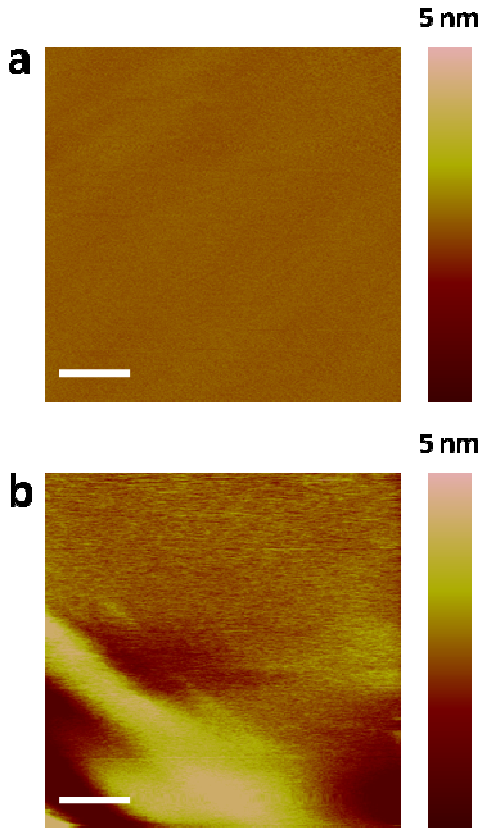

Figure 3.12. (a) Typical 1 μm × 1 μm TM-AFM image of a bilayer-covered quartz surface after the adsorption of 0.1 mg mL^{-1} DOTAP for 15 minutes. (b) TM-AFM image of the same area as shown in (a) but after the surface had been deformed using contact mode AFM. Scale bars denote 200 nm.

In all areas imaged, the surface was uniform with the exception of a few 1-2 nm pits and bulges, and there was no evidence of adsorbed vesicles. Since the surface morphology is very similar to that of the underlying silica, these images do not necessarily provide unambiguous information about SLB formation. Furthermore, the fluid nature of a SLB prevents complete and permanent removal of small areas of lipids from a

surface to measure SLB thickness. Hence considerable mechanical perturbation of the SLB is required to disrupt the SLB. CM-AFM was thus also used to cause deformation of the surface, which was subsequently imaged in tapping mode. The change in morphology after such an experiment (Figure 3.12 (b)) indicated that a deformable, thin layer was present on the surface. These observations added to the characteristic EW-CRDS response indicating that a SLB had, indeed, formed on the surface.

3.3.12 QCM-D monitoring of SLB formation

The formation of the DOTAP SLB was monitored using QCM-D to ensure and confirm that the conditions used were amenable to SLB formation. A typical QCM-D response upon flowing 0.1 mg mL^{-1} DOTAP SUV solutions over the sensor crystals at a rate of 10 µl min^{-1} is shown in Figure 3.13, with the low rate of flow necessary to maintain a stable baseline. Subsequent EW-CRDS experiments were possible at a more rapid flow rate of 0.5 mL min^{-1} allowing faster experiments.

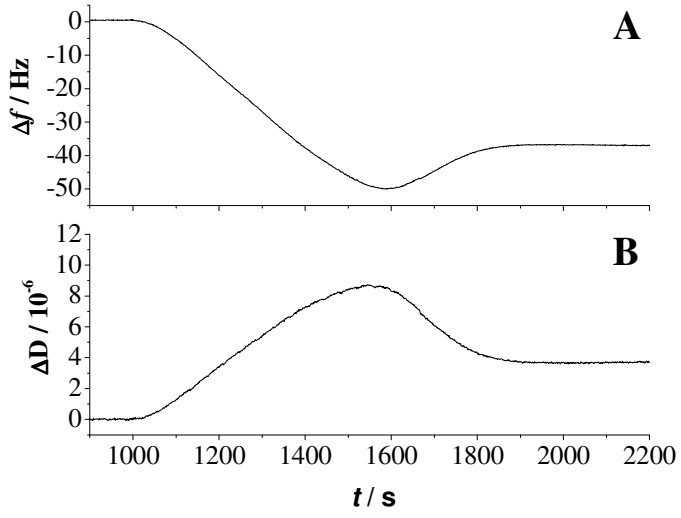

Figure 3.13. Change in frequency (A) and dissipation (B) recorded on the QCM-D upon flowing 0.1 mg mL^{-1} DOTAP in buffer A (pH 7.4) over the SiO_2 sensor chip.

The morphology of the curves was consistent with the formation of a SLB (via the critical surface concentration pathway), but the final change in frequency was slightly larger than previous results for other lipids.[32,34,38,39] At t = 2000 s, the DOTAP solution was exchanged with buffer A solution to wash the surface. There was no change in the QCM-D signal indicating that the bilayer was stable under the flow of buffer A. The corresponding dissipation initially increased with time to a maximum value and then decreased slightly before reaching a stable value, consistent with the formation of a SLB.

3.3.13 EW-CRDS of TPPS on silica and SLB-modified silica

We were first interested in observing whether there was any significant contribution from mass transport in the adsorption kinetics of TPPS at an SLB. To this end, the effect of flow rate on the adsorption rate for a bulk TPPS concentration of 0.5 μM was studied. Typical data are shown in Figure 3.14 (a), plotted as the interfacial optical absorbance due to the adsorbed TPPS vs. time. Note that when using EW-CRDS to study adsorption processes,[11,45] it is necessary to account for the contribution to the EW-CRDS signal from the optical absorbance by bulk solution (since the effective path length is ~1 μm[45]). To determine this contribution, the EW-CRDS response was monitored upon the addition of TPPS to the cell. At pH 7.4, the silica surface is negatively charged[8] meaning that the negatively-charged TPPS would not be expected to adsorb significantly to silica on electrostatic grounds. To determine the absolute absorbance by TPPS in bulk, the initial ring-down time, τ_0, with buffer A on the prism was first measured. The steady-state value of the optical absorbance with TPPS in buffer A in the EW-CRDS set-up was then measured. For example, the bulk absorbance for 5 μM TPPS was $A = 3.2 \times 10^{-4}$. The bulk absorbance scales linearly with concentration and represents a small correction. An alternative method to correct for the bulk was to recognize that the initial value of optical absorbance upon the introduction of TPPS flow is dominated by the bulk (rather than the surface) TPPS. Both methods of treating the bulk optical absorbance gave consistent data.

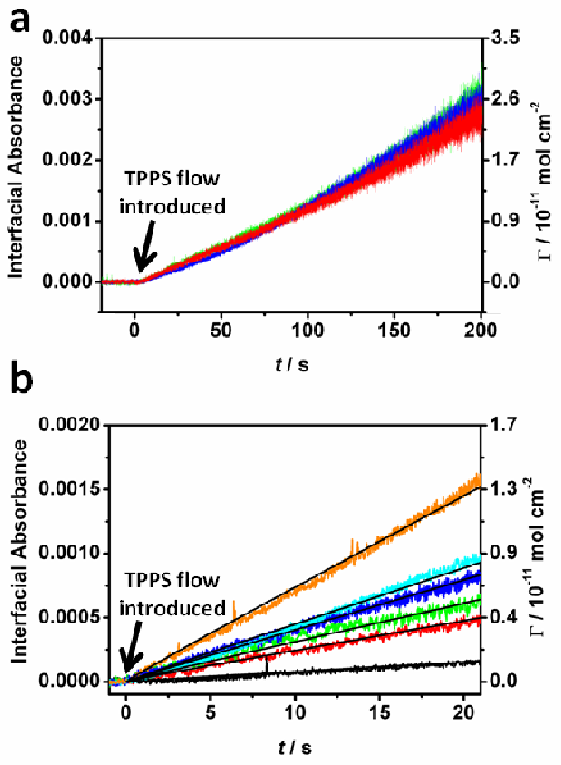

Figure 3.14. (a) Effect of flow rate on the adsorption of TPPS to the bilayer-modified prism surface. The data are shown as the optical absorbance for the interfacial excess after correction for bulk optical absorbance. Flow rates were 0.5 mL min^{-1} (red), 0.75 mL min^{-1} (green), and 1 mL min^{-1} (blue). (b) EW-CRDS response to the adsorption of TPPS to the bilayer with linear fits according to the model used (see text for values) for TPPS concentrations of 0.5 µM (black), 1 µM (red), 2 µM (green), 3 µM (blue), 4 µM (cyan), 5 µM (orange).

The EW-CRDS response in Figure 3.14 (a) shows only a small effect due to mass transport for the flow rates of 0.5 mL min^{-1}, 0.75 mL min^{-1} and 1 mL min^{-1}, indicating that the process is largely surface-controlled with these mass transport rates. The measurement of interfacial absorbance

allows direct output of surface concentration, Γ, and it can be seen that TPPS accumulates on the surface linearly with time reaching a concentration of *ca.* 2.5 x 10^{-11} mol cm^{-2} at the end of the experiment.

Figure 3.14 (b) shows the bulk-corrected EW-CRDS response as a function of time. Studies were made with TPPS concentrations of 0.5 μM, 1 μM, 2 μM, 3 μM, 4 μM and 5 μM at a rate of 0.5 mL min^{-1}. The second y-ordinate in Figure 3.14 (b) is again the concentration, of TPPS at the bilayer-solution interface calculated using the extinction coefficient, ε_{405} = 1.15×10^5 dm^3 mol^{-1} cm^{-1}, determined by UV-visible spectroscopy. The transients were again essentially linear with time for all concentrations supporting the assumption of pseudo first-order adsorption kinetics. The data were analyzed to deduce rate constants for each concentration giving 0.5 mM ($k = 1.6 \times 10^{-4}$ cm s^{-1}), 1mM ($k = 2.8 \times 10^{-4}$ cm s^{-1}), 2 mM ($k = 1.6 \times 10^{-4}$ cm s^{-1}), 3 mM ($k = 1.4 \times 10^{-4}$ cm s^{-1}), 4 mM ($k = 1.1 \times 10^{-4}$ cm s^{-1}) and 5 mM ($k = 1.5 \times 10^{-4}$ cm s^{-1}) for the binding of TPPS to the DOTAP SLB. This gives a mean rate constant of $k = 1.7 (\pm 0.6) \times 10^{-4}$ cm s^{-1}.

3.4 Conclusions

EW-CRDS has been demonstrated to be a useful tool for probing the adsorption behaviour and kinetics of macromolecules to planar surfaces. The silica surface inherent to this technique has been used as a

model substrate and the surface chemistry manipulated by alteration of pH, followed by chemical modification with polyelectrolyte and cellulose layers. Initial adsorption kinetics have been extracted, providing valuable information on binding rates.

For long time-scale experiments (1 hour) adsorption *vs*. time behaviour on silica was found to be characteristic for each polymer. Initial adsorption kinetics were elucidated for each polymer as a function of pH on silica and extended to cellulose and PGA functionalized surfaces. For two of the polymers studied, PSPMA and mannose-modified glycopolymer, the adsorption kinetics were seen to be highly surface-dependent with highest rates on cellulose-modified surfaces. PAA shows a much smaller rate dependence on the nature of the adsorption surface.

The studies herein highlight that the use of EW-CRDS for adsorption measurements at the solid-liquid interface holds much promise due to its relative simplicity and versatility. The ease of modification of the silica surface provides many opportunities across a vast range of thin films and functionalities. Aside from simply studying adsorption/desorption kinetics, the possibility to study further aspects of polymer adsorption such as exchange in polymer layers and effects under flow are also envisaged.

Secondly, EW-CRDS has been demonstrated as a powerful technique for monitoring the formation of a SLB via the method of vesicle fusion, and for the study of molecular adsorption kinetics at the resulting SLBs. Notably, the EW-CRS time signature is itself highly characteristic of the

bilayer formation process. To confirm that SLBs were formed from the DOTAP vesicles, complementary AFM experiments were performed. The *in situ* TM-AFM images showed that the resulting SLB was uniform and free from defects. Significantly, the DOTAP SLB was essentially optically transparent to allow the study of the adsorption of the anionic porphyrin, TPPS, in real-time to the SLB-modified surface. The kinetic rate constant for the adsorption of TPPS to the SLB was found to be $1.7\ (\pm\ 0.6) \times 10^{-4}$ cm s^{-1}.

The ability to form a SLB on the quartz prism inherent to EW-CRDS, and to monitor the interactions of biomolecules with the SLB *in situ* and in real time, expands the applicability of EW-CRDS to the study of biomolecules in biologically relevant environments. The studies herein demonstrate that EW-CRDS is a powerful and straightforward technique to probe physicochemical phenomena at SLBs and a wide range of processes that could be investigated are envisaged.

3.5 References

(1) Edwards, D. C. *Journal of Materials Science* **1990**, *25*, 4175.

(2) *Polymer Surface Modifications: Relevance to Adhesion*; Mittal, K. L., Ed.; VSP: Utrecht, 1996.

(3) Russel, W. B.; Saville, D. A.; Schowalter, W. R. *Colloidal Dispersions*; Cambridge University Press: Cambridge, 1989.

(4) Wicks, Z. W.; Jones, F. N.; Pappas, S. P. *Organic Coatings: Science and Technology*; 2nd ed.; Wiley-Interscience: New York, 1999.

(5) G. J. Fleer; M. A. Stuart Cohen; J. H. Scheutjens; T. Cosgrove; Vincent, B. *Polymers at Interfaces*; Chapman and Hall, 1993.

(6) Fisk, J. D.; Batten, R.; Jones, G.; O'Reilly, J. P.; Shaw, A. M. *Journal of Physical Chemistry B* **2005**, *109*, 14475.

(7) Shaw, A. M.; Hannon, T. E.; Li, F. P.; Zare, R. N. *Journal of Physical Chemistry B* **2003**, *107*, 7070.

(8) Fan, H. F.; Li, F. P.; Zare, R. N.; Lin, K. C. *Analytical Chemistry* **2007**, *79*, 3654.

(9) Ong, S. W.; Zhao, X. L.; Eisenthal, K. B. *Chemical Physics Letters* **1992**, *191*, 327.

(10) Dong, Y.; Pappu, S. V.; Xu, Z. *Analytical Chemistry* **1998**, *70*, 4730.

(11) Powell, H. V.; Schnippering, M.; Mazurenka, M.; Macpherson, J. V.; Mackenzie, S. R.; Unwin, P. R. *Langmuir* **2009**, *25*, 248.

(12) Haselberg, R.; van der Sneppen, L.; Ariese, F.; Ubachs, W.; Gooijer, C.; de Jong, G. J.; Somsen, G. W. *Analytical Chemistry* **2009**, *81*, 10172.

(13) van der Sneppen, L.; Gooijer, C.; Ubachs, W.; Ariese, F. *Sensors and Actuators B-Chemical* **2009**, *139*, 505.

(14) Kontturi, E.; Tammelin, T.; Osterberg, M. *Chemical Society Reviews* **2006**, *35*, 1287.

(15) Klemm, D.; Heublein, B.; Fink, H.-P.; Bohn, A. *Angewandte Chemie International Edition* **2005**, *44*, 3358.

(16) Rehfeldt, F.; Tanaka, M. *Langmuir* **2003**, *19*, 1467.

(17) Schaub, M.; Wenz, G.; Wegner, G.; Stein, A.; Klemm, D. *Advanced Materials* **1993**, *5*, 919.

(18) Mueller, P.; Rudin, D. O.; Tien, H. T.; Wescott, W. C. *Nature* **1962**, *194*, 979.

(19) Ottova, A. L.; Tien, H. T. *Bioelectrochemistry and Bioenergetics* **1997**, *42*, 141.

(20) Sackmann, E. *Science* **1996**, *271*, 43.

(21) Lonez, C.; Vandenbranden, M.; Ruysschaert, J.-M. *Progress in Lipid Research* **2008**, *47*, 340.

(22) Liu, J.; Stace-Naughton, A.; Jiang, X.; Brinker, C. J. *Journal of the American Chemical Society* **2009**, *131*, 1354.

(23) Generosi, J.; Piccinini, M.; Marcelli, A.; Belardinelli, S.; Pozzi, D.; Castellano, A. C. *Infrared Physics & Technology* **2007**, *50*, 14.

(24) Desigaux, L.; Sainlos, M.; Lambert, O.; Chevre, R.; Letrou-Bonneval, E.; Vigneron, J.-P.; Lehn, P.; Lehn, J.-M.; Pitard, B. *Proceedings of the National Academy of Sciences of the United States of America* **2007**, *104*, 16534.

(25) Wurpel, G. W. H.; Sovago, M.; Bonn, M. *Journal of the American Chemical Society* **2007**, *129*, 8420.

(26) McConnell, H. M.; Watts, T. H.; Weis, R. M.; Brian, A. A. *Biochimica Et Biophysica Acta* **1986**, *864*, 95.

(27) Liu, J.; Conboy, J. C. *Langmuir* **2005**, *21*, 9091.

(28) Mardilovich, A.; Kokkoli, E. *Langmuir* **2005**, *21*, 7468.

(29) Generosi, J.; Castellano, C.; Pozzi, D.; Castellano, A. C.; Felici, R.; Natali, F.; Fragneto, G. *Journal of Applied Physics* **2004**, *96*, 6839.

(30) Pompeo, G.; Girasole, M.; Cricenti, A.; Cattaruzza, F.; Flamini, A.; Prosperi, T.; Generosi, J.; Castellano, A. C. *Biochimica Et Biophysica Acta-Biomembranes* **2005**, *1712*, 29.

(31) Mager, M. D.; Melosh, N. A. *Langmuir* **2007**, *23*, 9369.

(32) Keller, C. A.; Kasemo, B. *Biophysical Journal* **1998**, *75*, 1397.

(33) Reimhult, E.; Zach, M.; Hook, F.; Kasemo, B. *Langmuir* **2006**, *22*, 3313.

(34) Seantier, B.; Kasemo, B. *Langmuir* **2009**, *25*, 5767.

(35) Richter, R.; Mukhopadhyay, A.; Brisson, A. *Biophysical Journal* **2003**, *85*, 3035.

(36) Richter, R. P.; Brisson, A. R. *Biophysical Journal* **2005**, *88*, 3422.

(37) Knoll, W.; Koeper, I.; Naumann, R.; Sinner, E.-K. *Electrochimica Acta* **2008**, *53*, 6680.

(38) Seantier, B.; Breffa, C.; Felix, O.; Decher, G. *Journal of Physical Chemistry B* **2005**, *109*, 21755.

(39) Viitala, T.; Hautala, J. T.; Vuorinen, J.; Wiedmer, S. K. *Langmuir* **2007**, *23*, 609.

(40) Egawa, H.; Furusawa, K. *Langmuir* **1999**, *15*, 1660.

(41) Reinl, H. M.; Bayerl, T. M. *Biochemistry* **1994**, *33*, 14091.

(42) Richter, R. P.; Bérat, R.; Brisson, A. R. *Langmuir* **2006**, *22*, 3497.

(43) Tanaka, M.; Kaufmann, S.; Nissen, J.; Hochrein, M. *Physical Chemistry Chemical Physics* **2001**, *3*, 4091.

(44) Bitziou, E.; Rudd, N. C.; Edwards, M. A.; Unwin, P. R. *Analytical Chemistry* **2006**, *78*, 1435.

(45) Zhang, M.; Powell, H. V.; Mackenzie, S. R.; Unwin, P. R. *Langmuir* **2010**, *26*, 4004.

Chapter 4. Particle adsorption studies using confocal laser scanning microscopy (CLSM): Adsorption rates and localised delivery for mimetic and biological systems

This chapter concerns the study of microparticle adsorption to some of the model surfaces considered in Chapter 3 and extends to the development of delivery systems to both these and biological surfaces. The initial focus here is primarily the cellulose surface compared to surfaces of differing charge. Confocal laser scanning microscopy (CLSM) is used as a visualisation tool to quantify particle adsorption rates and characteristics. Comparative studies between different surfaces are made using diffusion experiments. These studies are then extended to increase mass transport rates via incorporation of, firstly, a radial impinging jet system (as used in Chapter 3) and, secondly, a vertical flow cell based on a scanning electrochemical cell microscopy (SECCM) probe. The latter system employs migration as a mode of mass transport and also provides a convenient system to deliver particles and other species directly to a single root hair cell surface.

Adsorption of 200 nm and 1.1 μm carboxylate-modified (anionic) particles to regenerated model cellulose surfaces was studied as a function of electrolyte concentration using CLSM. Experiments under the same

conditions were extended to positively- (poly-L-lysine, PLL) and negatively- (poly-L-glutamic acid, PGA) charged polyelectrolyte surfaces for comparison. Deposition rates are found to be similar on cellulose and PGA and significantly increased on the electrostatically favorable surface, PLL. Adsorption rates are considerably lower at decreasing ionic strength, an effect which is greater for 200 nm particles than 1.1 μm particles due to longer range repulsions between particles. These experiments are then extended for the measurement of relatively fast kinetics via incorporation of an impinging jet flow cell to the CLSM set up, under which conditions the adsorption of 200 nm particles is found to be surface controlled whereas adsorption of 1.1 μm particles was found to be influenced by mass transport rate. For the surface controlled rates, kinetic rate constants were then calculated.

Following this, a microscale vertical flow cell system is designed for adsorption studies on model and biological surfaces. This system is tested on the charged PLL and PGA surfaces using the same anionic particles, showing a large effect from electrostatic attraction on adsorption rates. The adsorption sites for particles of this size are seen to be dominated by the three phase boundary, *i.e.* at the edge of the meniscus. Removal of the meniscus confinement is shown to create a much larger deposition area. Finally, the versatility of this system is demonstrated by deposition of charged particles and polymers onto an individual root hair cell surface.

4.1 Introduction

Understanding rates and mechanisms of colloidal particle adsorption at the solid/liquid interface is of wide interest to a wide range of fields in chemistry and broader science with significant experimental and theoretical study.[1-3] A range of analytical techniques are used for studies in this area including optical microscopy,[1,2] reflectometry[3-5] and atomic force microscopy (AFM),[6-8] and such techniques allow a range of particle sizes and surfaces to be studied.

Thin polymer films can be used to create highly insightful model surfaces to probe adsorption processes. Many are optically transparent, when sufficiently thin, so allow an array of optical microscopic and spectroscopic techniques to be used to probe surface phenomena through the interface, while allowing further access to the surface from above with, for example, flow cells, electrodes and capillaries. Of particular interest here is cellulose, being abundant component of plant cell walls, hereby providing relevant biological adhesion data (see Chapter 3.1 for further details).[9-12]

Herein, the initial rates of adsorption of carboxylate-modified (negatively-charged) colloidal particles to regenerated cellulose films, formed via Langmuir-Schaefer transfer, are measured using CLSM. Initial rates provide useful information at short deposition time, giving a greater understanding of competitive and rapid systems. CLSM allows the

quantification of adsorption rates of 1.1 μm and 200 nm particles to planar surfaces through both particle counting and measurement of change in fluorescent intensity. CLSM is shown to be particularly well suited to measurement of particle adsorption when compared to widefield optical techniques, as manipulation of the optical pinhole inherent to the technique allows the study of only a very shallow focal plane, thus excluding the majority of particles in bulk, and allowing for more accurate measurement of adsorption rates. Rates are measured as a function of electrolyte concentration, and referenced against positively and negatively charged polyelectrolyte surfaces formed by drop casting. Experiments are extended to enable the extraction of kinetic values for the fastest processes, by coupling to a simple impinging jet system.

Finally, a vertical delivery system based on an SECCM probe is developed, which allows measurements of adsorption to be made directly on single cells. A recent addition to the applications of scanned probe microscopies (SPMs) has been the introduction of vertically-mounted microfluidic probes to provide a well-defined and spatially-resolved flux of species to a surface without the need to immerse the entire sample in solution.[13-15] The potential uses of these types of localised microfluidic cells is broad encompassing, for example, delivery, patterning and analysis of surfaces and interfaces.

Amongst other approaches for defined surface modification, inkjet printing is well-established for depositing liquids on surfaces,[16] but involves the drying of droplets with related artifacts. Many approaches have also been used for surface modification in continuous media. Dip pen

nanolithography,[17] for example, is an atomic force microscopy (AFM) based approach for patterning on the nanometer-scale. Further techniques involve local electrochemical control, for example using scanning electrochemical microscopy (SECM)[18,19] and capillary-based systems utilising micro- and nano-pipettes, primarily scanning ion conductance microscopy (SICM).[20] SICM-related techniques employ electromigration as a means to deliver charged species to a surface of interest, and this aspect has been demonstrated using DNA and proteins[21] and for local delivery of fluorescent molecular probes to cells.[22]

An alternative approach is to work in a defined droplet formed between a pipette and surface, thus defining a 'cell' area and removing the need to immerse a sample in continuous media. The scanning micropipette contact method (SMCM)[23] represents an early configuration of this type of approach, using a micron-sized micropipette to record localized electrochemical measurements in a droplet size similar to that of the pipette terminus. Exchanging a single-barreled pipette for a dual channel 'theta' pipette, in an approach termed SECCM,[24] far increases the potential of this approach; the dual channel design allowing migration of species through the droplet cell *ie* with the two barrels acting as an inlet and outlet for the cell. The migratory flux between the barrels and to the surface has been modeled,[25] thus allowing a high level of control. Positional feedback is also based upon this migration current allowing control of the meniscus height on both conducting and insulating surfaces. So far this approach has been used on electrochemically-active systems[26] giving both a spatially-resolved electrode area and good control of mass transport rates to the surface.

There is, however, broad scope for utility in non-Faradaic processes *eg.* study of localized adsorption kinetics and controlled delivery to, and patterning of, surfaces and interfaces. Creation of probes of this type is a simple, inexpensive and flexible process. As a non-contact technique, the range of samples to which this technique is applicable is potentially broad, and pipet sizes can be tailored from tens of nanometers to tens of microns. Furthermore, when necessary, the entire probe apex can be immersed in small droplets of solution and still maintain a high level of positional control.

Herein, the use of an SECCM probe as a vertical microfluidic cell for use in adsorption and delivery experiments is demonstrated. Negatively-charged carboxylate-modifed microparticles are used to study the applicability of this configuration as they provide a simple means of quantification via particle counting. The adsorption of these particles to both electrostatically favorable and unfavorable surfaces within the meniscus is examined and transport rates are modified by variation of potential between barrels. Finite element modeling is used to quantify the transport rates to the surface as a function of potential and to confirm the nature of deposition. Adsorption characteristics are further studied via removal of the meniscus confinement, achieved by addition of droplets of salt solution to the tip apex. Finally, the flexibility of the method is demonstrated on a biological sample in the form of a root hair cell via delivery of the charged particles used earlier and also charged polymer molecules.

4.2 Experimental

4.2.1 Chemicals

1.1 μm and 200 nm diameter carboxylate–modified fluorescent polystyrene microparticles were purchased from Invitrogen (UK) at a concentration of 2% by mass particles and 2 mM NaN_3 as a stabiliser, with optical absorption maximum at 505-515 nm. All other chemicals were purchased from Sigma-Aldrich unless otherwise stated. For each experiment, suspensions of microparticles were diluted to 0.005% concentrations and 0.005 mM NaN_3 respectively, using 18.2 MΩ Milli-Q water (Millipore Corporation). Ionic concentrations of the solutions were varied by addition of NaCl, in a range from 10 μM to 10 mM concentration. Solutions were made fresh each day and pH was measured to be 6.8 ± 0.2.

4.2.2 Cellulose surface functionalisation

Thin films of cellulose were created via regeneration from trimethylsilyl cellulose (TMSC) Langmuir-Schaefer films as described in detail in Chapter 3.2.6.[27] Briefly, TMSC was synthesised by the method first described by Schaub *et al.*[11] Borosilicate glass coverslips were made hydrophobic by drop-coating with dichlorodimethylsilane and washing with copious amounts of propan-2-ol (IPA), followed by Langmuir-Schaefer transfer of TMSC (0.5 mg ml^{-1} in chloroform) monolayers (typically five) using a Langmuir trough (NIMA Technology). The TMSC

multilayers were then converted back into cellulose by exposure to concentrated HCl fumes for 30 s. A characteristic change in the hydrophobicity of the surface, shown by the change in the static contact angle of water with the surface from ~70-75˚ for TMSC to ~30-35˚ for cellulose[10,28] was used an an indicator for cellulose regeneration.

4.2.3 Polyelectrolyte surface functionalisation

Positive and negative polyelectrolyte surfaces were prepared on cleaned borosilicate glass cover slips by drop casting of poly-L-lysine (PLL, MW 40,000-70,000) or PLL followed by poly-L-glutamic acid (PGA, MW 50,000-100,000). Solutions of 1 mg ml^{-1} concentration of each were allowed to adsorb for 20 minutes followed by rinsing with 18.2 MΩ Milli-Q water (25°C) and drying under a nitrogen stream.

4.2.4 Particle adsorption experiments

Particle adsorption experiments were performed using a laser scanning confocal microscope (Leica TCS SP5 X, Leica Microsystems) equipped with a tunable white light laser (WLL) on an inverted microscope stand (DMI 6000, Leica Microsystems). Fluorescent excitation was achieved at a wavelength of 515 nm and emission was collected between 525 and 600 nm. For particle visualization, a 40x oil immersion lens was used for experiments concerning 1.1 µm particles and a 63x oil immersion lens for experiments concerning 200 nm particles, respectively. The

pinhole was adjusted to view only the surface plane and voltage to the photomultiplier tube (PMT) was optimized to provide a strong signal for each particle without saturating the detector. Particle counting was performed using commercial image analysis software (Scanning Probe Image Processor (SPIP), Image Metrology), via thresholding based upon intensity of fluorescent light from each particle.

4.2.5 Impinging jet cell kinetic experiments

For some measurements of kinetics mass transport rates were enhanced using an impinging jet flow system comprising of a Teflon pipe (inner diameter 2 mm, length 5 mm, shown schematically in Figure 4.1) at a separation of 500 μm from the polymer-coated surface as described and modelled in previous publications.[29,30] Flow rates were varied from 1 ml min^{-1} to 4 ml min^{-1}, under which conditions fully-developed laminar flow prevails at the exit to the nozzle.[31]

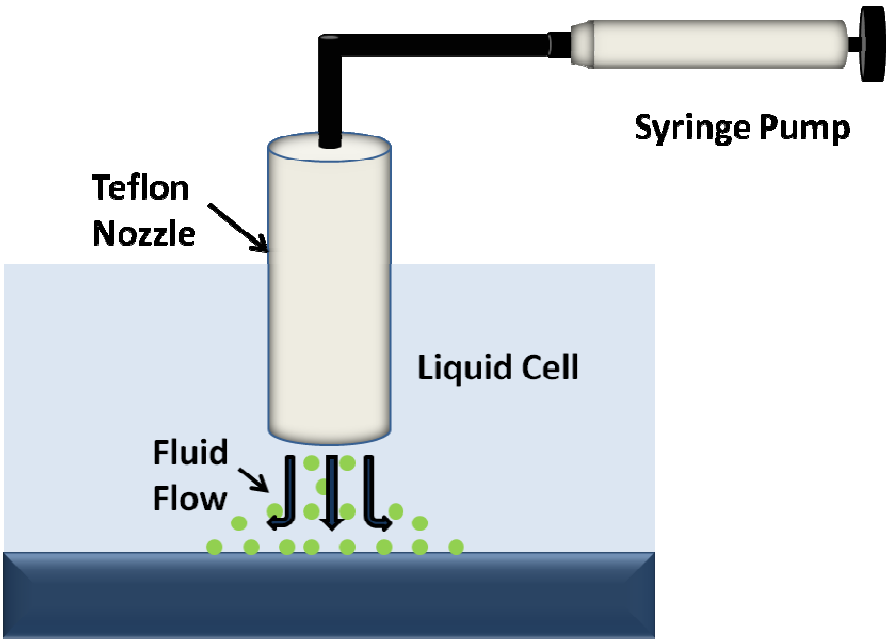

Figure 4.1. Schematic of impinging jet flow cell used for kinetic experiments.

4.2.6 Chemicals for vertical flow cell experiments

The same 1.1 µm diameter carboxylate–modified fluorescent polystyrene microparticles suspensions were diluted to 0.001% particles and 0.001 mM NaN_3 respectively, using 18.2 MΩ Milli-Q water. Ionic concentration of the solution was kept constant by addition KCl to 1 mM concentration. The zeta potential and electrophoretic mobility of the particles in this solution were measured by Escubed Ltd. (Leeds, UK) using a Zetasizer Nano ZS (Malvern, UK). Polymer adsorption experiments involved two synthetic polymers (provided by Dr. Florence Gayet and Professor David Haddleton of the Warwick polymer group) consisting of (a) 2% Rhodamine/98% Sulphonate functionalised repeat units (M_n = 1561) and (b) 4% Rhodamine/96% Sulphonate functionalised repeat units

(M_n = 1877). Solutions were made to concentrations of 1 mg mL^{-1}, corresponding to 0.64 mM and 0.53 mM respectively. The predominate sulphonate functionality gave these polymers a net negative charge, with the Rhodamine acting as an adhesive modifier.

4.2.7 SECCM probe fabrication

Dual barrel borosilicate glass theta capillaries (Harvard Apparatus, UK) were pulled to an overall size at the end of ~20 µm diameter using a laser pipette puller (Model P-2000, Sutter Instruments, UK). In order to form a stable meniscus, the outer walls of the pipettes were made hydrophobic using dimethyldichloromethane. Both barrels were then filled with the microparticle solution (~50 µL per barrel) and chlorodized silver wires (Ag/AgCl) were inserted into each barrel.

4.2.8 Adsorption experiments with incorporated vertical flow cell

SECCM probes were approached to the functionalised glass surfaces, used as the base of a petri dish (Willco Wells, Netherlands), with a 3-axis piezoelectronic positioning system (Nanocube P-611.3S, Physik Instrumente). The cell was humidified by using drops of saturated KCl solution on the inner plastic lip of the petri dish. The vertical flow cell system is shown schematically in Figure 4.2. The meniscus thickness, *h*, was 2 µm.

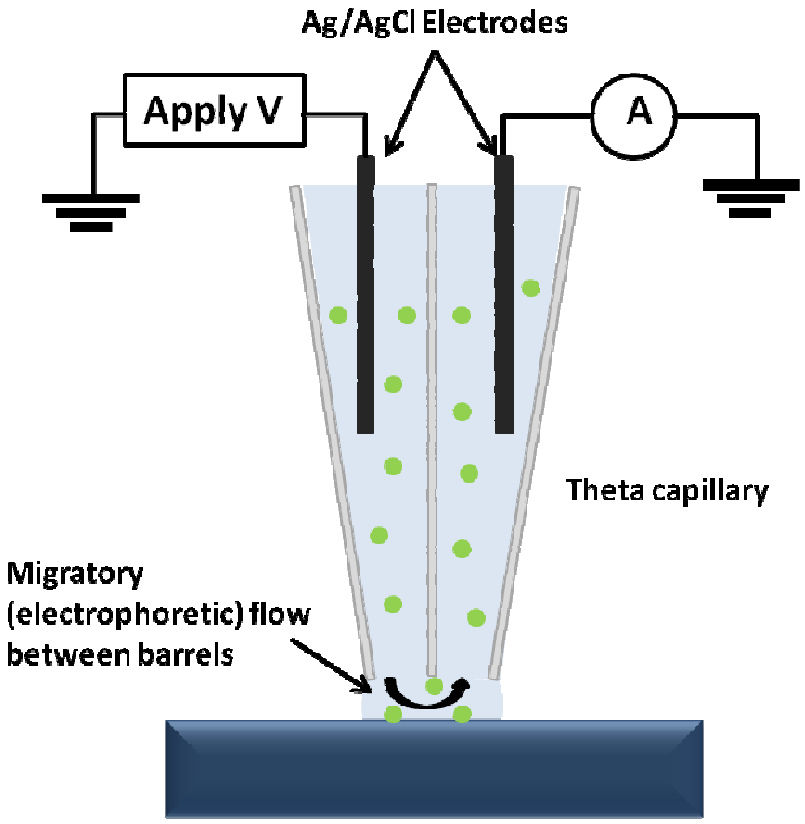

Figure 4.2. Schematic of the vertical flow cell system.

The pipette was typically oscillated at 70 Hz with a 100 nm peak-to-peak amplitude. Control of, and data acquisition from, the piezoelectric/electrochemical apparatus was performed using an FPGA card (PCIe-7852R, National Instruments) with a LabVIEW interface written in house (described in more detail in Chapter 2.4). Particle adsorption was quantified using a laser scanning confocal microscope (LSCM, Leica TCS SP5 X, Leica Microsystems). Fluorescent excitation was achieved using a tunable white light laser (WLL) at a wavelength of 515 nm and emission was collected between 525 and 600 nm. For

experiments where the meniscus confinement was removed, a 50 µl droplet of 1 mM KCl was added to the pipette tip after contact with the surface. This resulted in the droplet covering a circular area of diameter *ca*. 5 mm.

4.2.9 Simulations and modelling

The potential field within the pipette and meniscus/surrounding solution was calculated by finite element method (FEM) modelling using the Nernst-Planck equations, based on the model previously constructed by Dr Michael Snowden[25] and fully described therein. Simulations were performed using the commercial package Comsol Multiphysics v4.3 (Comsol AB, Sweden). A schematic of the generalised front face of the geometry is shown in Figure 4.3 (a), where the simulated domain represents half of a theta pipette (Figure 4.3 (b)), employing a plane of symmetry across the septum to enhance computational efficiency. To further enhance efficiency, the pipette is split into a lower part of high mesh density and an upper part of lower mesh density. The liquid domain outside the pipette can either extend into bulk solution, represented by a larger cylinder, or be confined within a limited meniscus between the pipette and the surface in a similar manner to the previous report.[25]

The relative simulated potential field for each case is shown in Figures 4.3 (c) for the bulk solution model and (d) for the meniscus-confined model. Here, the Nernst-Planck equations were solved as reported previously, for a pipette of dimensions total diameter, d_p, of 20 µm,

capillary semi angle, θ, of 8°, central segment thickness, t, of 1 µm and tip-sample separation (height), h_p, of 2 µm, filled with a solution of 1 mM KCl. The potential at the two faces E_1 and E_2 were assumed to be uniform across each face. For computational efficiency, E_1 was always set to 0 V and E_2 the effective potential of this face (as calculated from the experimental current). No flux boundary conditions were applied to the pipette walls, substrate and meniscus/bulk domain walls, whereas faces E_1 and E_2 were defined by an inflow boundary condition where

$$c_j = c_{j,\,init} \tag{4.1}$$

with c_j the concentration of species j and the subscript *'init'* indicating the initial condition (*i.e.* t=0).

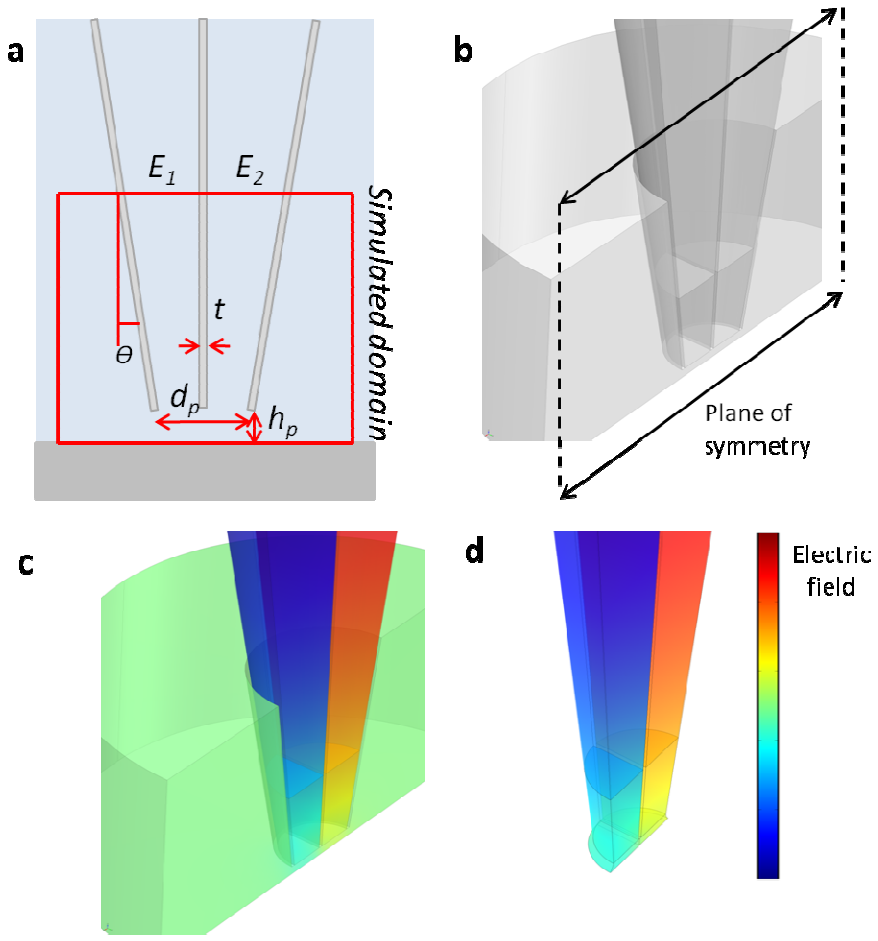

Figure 4.3. The simulated domain of the theta capillary flow cell set up showing (a) a schematic of the cross-section of the simulated domain, (b) a transparency of the simulated domain (with the plane of symmetry along the face), (c) the relative potential field for an immersed capillary and (d) the relative potential field for a capillary with a finite liquid meniscus.

4.3 Results and Discussion

4.3.1 Visualisation of surface bound particles

In order to quantify particle adsorption rates, CLSM was first used to view discrete particle adsorption. Figure 4.4 (a) shows part of a typical image of 200 nm carboxylate-modified particles on a PLL surface showing that they are clearly discernable at sparse coverage, despite approaching the optical (Rayleigh) resolution limit. The total area recordable in a single image at sufficient resolution to view these particles was measured to be *ca*. 62 x 62 µm. It is clear that the particles are highly monodisperse and show a consistent fluorescent signal. The cross section of two particles from this image, shown in (b), taken across the centre of the two particles, further indicates how the signal is similar from each particle, as well as the size.

Figure 4.3 (c) shows a similar image for 1.1 µm particles. Note here the scale bar at 20 µm compared to 5 µm for the 200 nm particles. The signal for these particles is again discrete and consistent, as confirmed in (d). The increased size of these particles allows a much larger area to be studied; for the experiments herein an area of 226 x 226 µm was studied. A small aggregate of 3 particles is also visible in the bottom right hand corner of this image.

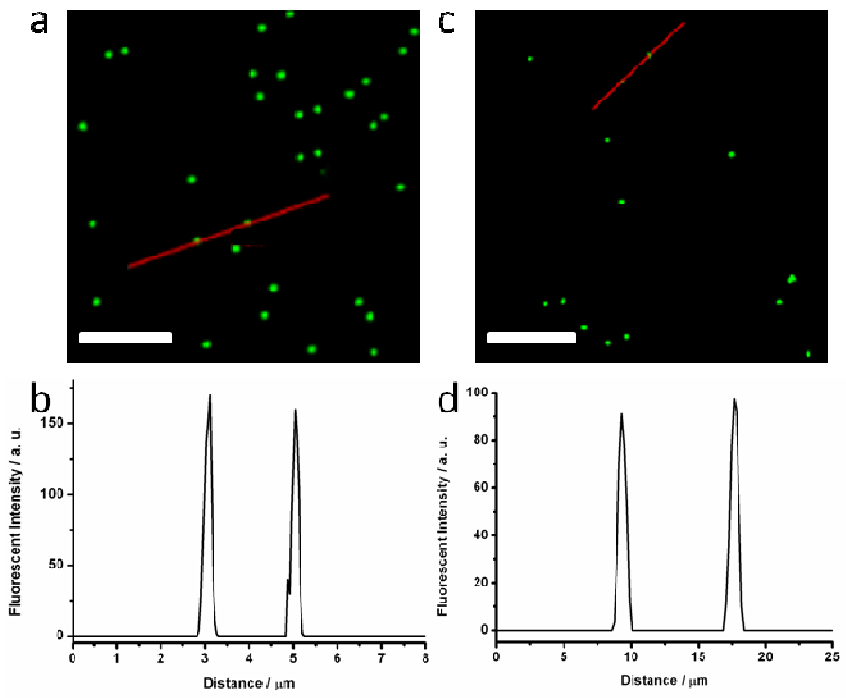

Figure 4.4. Cut-outs of typical LSCM images of adsorbed particles: (a) 200 nm particles (scale bar 5 µm), (b) cross section taken across the centre of two 200 nm particles, (c) 1.1 µm particle (scale bar 20 µm) and (d) cross section taken across the centre of two 1.1 µm particles. All images were acquired at 0.005 % by mass bulk particle concentration at 1 mM NaCl concentration on PLL-modified surface.

4.3.2 Transients of particle adsorption.

The LSCM signal provides two convenient methods to quantify particle adsorption. Particle counting is simple using commercial software to 'pick' particle signals at a certain threshold. Here we used typically 50 % of the typical maximum fluorescent intensity as the threshold limit. Alternatively the change in fluorescent intensity across the whole image

can be used and normalized against the signal for a single particle when resolving between particles is difficult. Here, we calculate this by dividing the initial fluorescent intensity by the number of particles (at very low surface coverage) on the surface at the start of each experiment, providing an average value. In addition, counting at higher surface coverage is possible, with average measured fluorescent intensity per particle found to be consistent in both cases.

Figure 4.5 shows the adsorption transients for 1.1 μm particles on PLL. It is apparent that the transients can be fitted as linear in this regime. The transient from particle counting analysis (a) gives a slightly higher rate than that for normalized fluorescence (b) in this case by ~10 %. This could be down to either some photobleaching of the particles or slight movement of the surface with respect to the focal plane. However, at this timescale it is clear both methods are in good agreement and, therefore, viable, which is useful as it allows species below the diffraction limit to be studied.

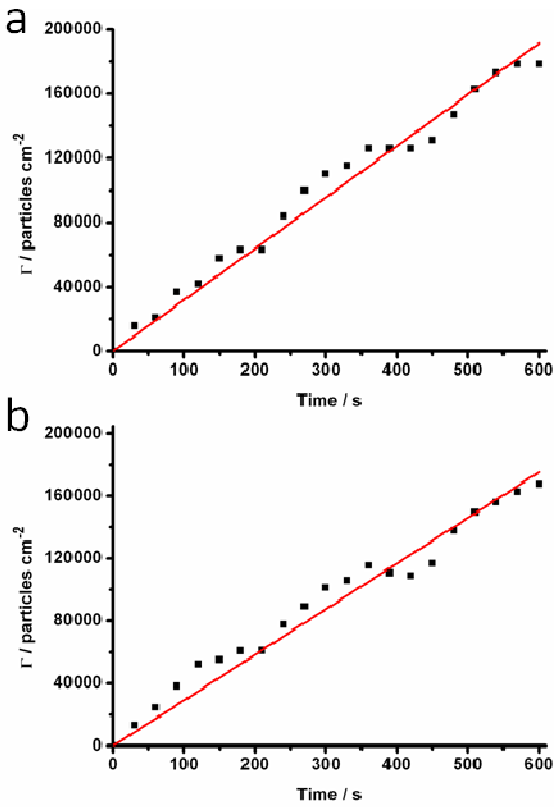

Figure 4.5. Example transients for (a) particle counting and (b) fluorescence intensity normalized with respect to the intensity from one particle. Shown here is a typical transient for 1.1 µm particles (0.005 % by mass) at 10 mM NaCl concentration on PLL.

4.3.3 Adsorption rates of 1.1 µm diameter particles to cellulose and polyelectrolyte surfaces

Adsorption rates were measured for the initial linear part of the adsorption process. Irreversible particle adsorption is often considered using the random sequential adsorption (RSA) model[32] where particles adsorb randomly on a surface with no overlap, following an initially linear rate at low surface coverage then slowing at higher surface coverage until a

final or 'jamming' surface coverage is reached. Here we are interested only in this initial linear regime, as understanding this initial rate is important for competitive and short timescale treatments.

Here the adsorption of charged particles to cellulose as a function of ionic concentration and particle size is considered and compared to the rates of adsorption to both electrostatically favorable and unfavorable surfaces. A single concentration of particles (0.005 %) is used to study the relative rate for each situation. Figure 4.6 shows an increase in the rate of adsorption of 1.1 µm carboxylate particles with increasing ionic concentration measured by particle counting.

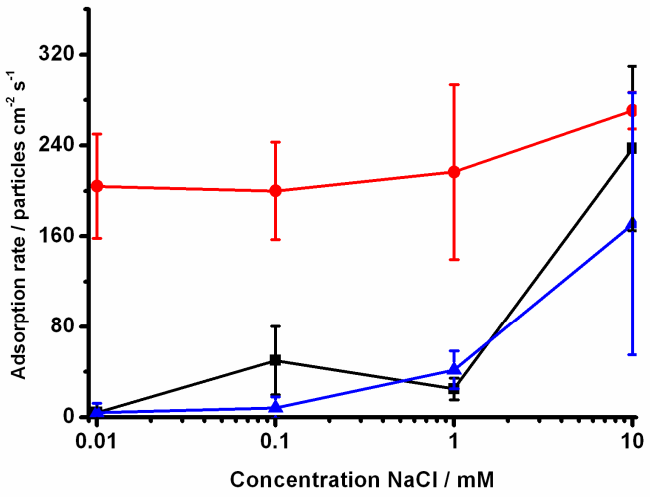

Figure 4.6. Particle adsorption rates for each surface taken from linear fits of particle adsorption transients over 10 minutes for 1.1 µm particles. Adsorption rates are quantified as function of ionic concentration (NaCl). Cellulose is shown in blue, PGA in black and PLL in red.

Adsorption rates for cellulose were very low below 1 mM NaCl concentration (negligible at 10 μM) and increase above this threshold, with rates highest at 10 mM rising to ~170 particles cm^{-2} s^{-1}. The cellulose surface is uncharged at the bulk pH (6.8) meaning a logical comparison is with positively- (attractive, PLL) and negatively- (repulsive, PGA) charged surfaces. Unsurprisingly, we see in the adsorption rate is high for the electrostatically attractive surface (PLL). This is largely constant from 0.01 to 1 mM with a small increase at 10 mM. Adsorption rates to the PGA surface can be considered to be quite similar to cellulose, though an increase is evident at 100 μM NaCl concentration for the PGA surface. Interestingly the cellulose surface is uncharged but adsorption rates are largely similar to the negatively-charged PGA.

The decreased double layer thickness (Debye length) due to the higher concentrations of NaCl reduces both the particle-particle and particle-surface electrostatic interactions. The Debye length, κ^{-1}, for a symmetrical monovalent electrolyte can be calculated using the equation

$$\kappa^{-1} = \sqrt{\left[\frac{\varepsilon_r \varepsilon_0 RT}{2F^2 C_0}\right]} \qquad (4.2)$$

where ε_r is the dielectric constant of the medium, ε_0 is the permittivity of free space, R is the gas constant, T is the absolute temperature in Kelvin, F is Faraday's constant and C_0 is the molar concentration of the electrolyte. For the concentrations used values of κ^{-1} are calculated to be 96 nm (0.01 mM), 30 nm (0.1 mM) 9.6 nm (1 mM) and 3.0 nm (10 mM) respectively. Logically, all rates are increased at the highest NaCl concentration (10

mM) which shows particularly the effect in decreasing particle-surface repulsion. This also manifests as closer packing on the surface (effectively increasing surface sites) but also increases aggregation of particles which provide a further adsorption route, as the particle-particle repulsion is smaller. The aggregation between particles did provide some difficulty in quantifiying how many particles were surface-bound. This was found to be particularly clear for the cellulose surface (accounting for the large errors between different areas) where a large amount of surface adsorbed particles were in aggregates.

4.3.4 Adsorption rates of 200 nm particles to cellulose and polyelectrolyte surfaces.

Experiments under the same conditions were performed for 200 nm particles (Figure 4.7). The concentration of particles was the same (0.005 % by mass) however this corresponds to a larger number of the smaller particles (~166.25 times).

For these smaller particles the effect of NaCl concentration is larger: There is negligible adsorption on any surface at 10 μM to 1 mM for cellulose and PGA largely due to repulsion between particles and the surface (this being clearer for the smaller particles as the ratio of the Debye radius to particle radius is higher. The adsorption rates to cellulose are again very similar to PGA with PLL much higher at both 1 mM and 10 mM. Again the electrostatically repulsive and neutral surfaces are similar

when compared to the electrostatically attractive surface. The difference in adsorption rate between the PLL and the other two surfaces is seen to be larger for the 200 nm particles compared to the 1.1 µm particles at the higher NaCl concentrations, but at the two lower concentrations adsorption rates are essentially the same (*i.e.* negligible) for 200 nm particles with much higher rates for 1.1 µm particles on PLL. This is somewhat suprising as on the electrostatically favaourable surface some adsorption would still be expected, however one explanation would be at such low electrolyte concentration it is possible that the 200 nm particles themselves are not stable.

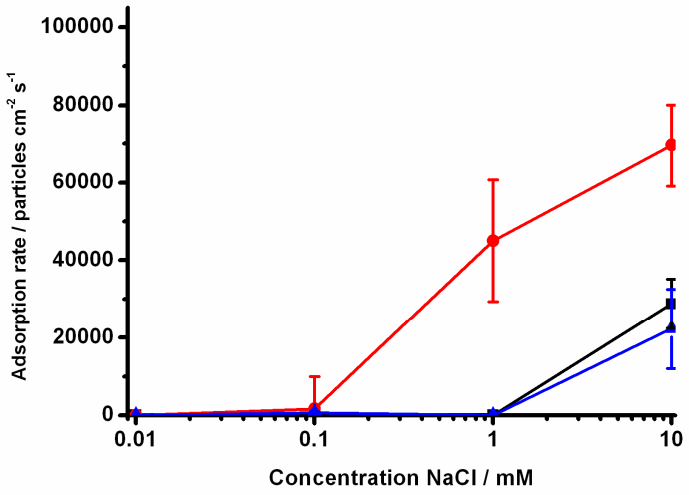

Figure 4.7. Particle adsorption rates for each surface taken from linear fits of particle adsorption transients over 1 minute for 200 nm particles. Adsorption rates are quantified by (as function of ionic concentration (NaCl). Cellulose is shown in blue, PGA in black and PLL in red.

For the previous experiments it is possible to estimate the diffusion coefficients, D, for the particles via the Stokes-Einstein equation

$$D = \frac{k_B T}{6\pi\eta r} \tag{4.3}$$

where k_B is the Boltzmann constant, T is the temperature in Kelvin, η is the dynamic viscosity of the solvent and r is the particles radius. For the particles used D is calculated as 4.4 x 10^{-9} cm^2 s^{-1} for the 1.1 µm particles and 2.5 x 10^{-8} cm^2 s^{-1} for the 200 nm particles respectively.

The mass transport (diffusional) coefficient of the particles, k_D, to a planar surface can be calculated by

$$k_D = \frac{D}{\delta} \tag{4.4}$$

where δ is the diffusion layer thickness which can be reasonably estimated as 200 µm.[33] The diffusional flux, j, can be then estimated by

$$j = k_D c^* \tag{4.5}$$

where c* is the number concentration of particles. For the concentrations used this gives j = 15 particles cm^{-2} s^{-1} for the 1.1 µm diameter particles and 1.4 x 10^4 particles cm^{-2} s^{-1} for the 200 nm diameter particles. Both of these diffusion only rates are below the maximum experimental values, indicating a contribution from other means of mass transportation, likely a combination of natural convection and some migration to the charged surface when electrostatically favourable.

4.3.5 Measurement of kinetics via accelerated mass transport rates.

To attempt to measure the initial adsorption kinetics, it was necessary to extend adsorption experiments to higher mass transport rates. This was performed by coupling with a vertical impinging jet flow cell to measure the surface-controlled (kinetic) initial adsorption rate on the fastest adsorbing system from our previous experiments (*i.e.* 200 nm particles adsorbing to PLL with 10 mM background electrolyte concentration). The mass transport rate of an impinging jet system under laminar flow conditions can be calculated by[34]

$$k_t = \frac{ShD}{d} \tag{4.6}$$

where k_t is the mass transfer coefficient, d is the nozzle diameter, D is the diffusion coeffiecient of the particles and Sh is the Sherwood number defined as

$$Sh = 1.51 Re^{1/2} Sc^{1/3} (H/d)^{-0.054} \tag{4.7}$$

where 1.51 and -0.054 are (empirical) coeffiecients and Re and Sc are defined by

$$Re = \frac{dU}{\upsilon} \tag{4.8}$$

$$Sc = \frac{\upsilon}{D} \tag{4.9}$$

υ here is the kinematic viscosity and U the average solution velocity across the nozzle.

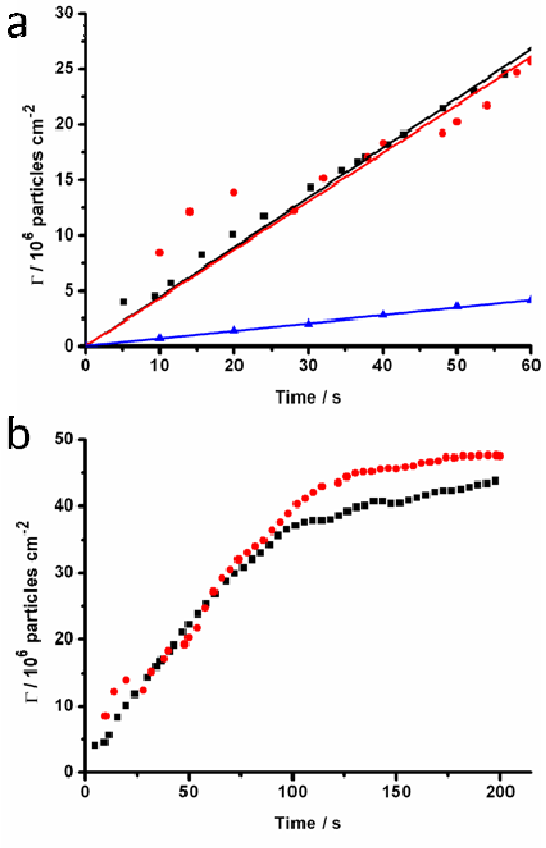

Figure 4.8. Surface concentration as a function of time for 0.005 % by mass 200 nm particles on PLL with 10 mM NaCl concentration, using impinging jet flow cell set-up. (a) Initial adsorption fitted linearly for 1 ml min^{-1} flow rate (black) and 4 ml min^{-1} flow rate (red). A typical transient of the static adsorption is shown in blue for reference. (b) The same data shown over an extended time period.

Figure 4.8 (a) shows the initial part of the adsorption transient (*i.e.* the first 60 s) for these conditions at 1 ml min^{-1} and 4 ml min^{-1} flow rates. As can be seen here the linear fits to this initial part of the adsorption are

very similar giving an initial rate of 4.5 (±0.1) x 10^5 particles cm^{-2} s^{-1} for 1 ml min^{-1} and 4.4 (±0.2) x 10^5 particles cm^{-2} s^{-1} for 4 ml min^{-1} respectively, compared to 7.0 (±0.1) x 10^4 particles cm^{-2} s^{-1} for the static solution. The values of k_t for the two elevated flow rates are calculated to be 6.8 x 10^{-5} cm s^{-1} (1 mL min^{-1}) and 1.4 x 10^{-4} cm s^{-1} (4 mL min^{-1}) giving fluxes of 7.8 x 10^5 particles cm^{-2} s^{-1} and and 1.5 x 10^6 particles cm^{-2} s^{-1}, respectively (assuming a similar first order relationship), both of which are higher than the adsorption rate seen, indicating the process is surface controlled. In this regime we therefore assume a first-order process defined by the following rate law

$$\left[\frac{d\Gamma}{dt}\right] = k_i c \tag{4.10}$$

where k_i is an initial (kinetic) rate constant, which is reasonable as surface coverage is low and adsorption is irreversible. This kinetic rate constant can then be calculated based upon the number of particles in solution: for a 0.005 % by mass solution of 200 nm particles we calculate a concentration of 1.14 x 10^{10} particles cm^{-3} (assuming a density of 1.05 g cm^{-3} as for polystyrene particles). These gives k_i values of 3.9 (±0.1) x 10^{-5} cm s^{-1} for 1 ml min^{-1} and 3.8 (±0.2) x 10^{-5} cm s^{-1} for 4 ml min^{-1} respectively. The transient for 4 ml min^{-1} flow rate appears considerably less smooth than for 1 ml min^{-1}, possibly due to the increased flow rate against cover slip thickness (170 μm) glass causing slight instabilities in the z position, exacerbated by the limiting of the pinhole to a very thin surface plane so as to view only surface adsorption. However, from the similarity in the fitted

flow rate this can be considered unimportant in calculation of k_i. In Figure 4.7 (b) we see the transients over a longer timescale: it is apparent the initial (linear) portion continues up to ~100 s rates after which the rate reduces towards jamming coverage as surface sites are occupied.

Figure 4.9 shows similar experiments performed for the 1.1 μm particles with the same concentration (in terms of % by mass) for flow rates of 1 ml min^{-1} flow rate, 2 ml min^{-1} flow rate and 4 ml min^{-1}. It is clear that the adsorption rates here are strongly influenced by the mass transport rates, with adsorption rates of 5.7 ± 1.3 x 10^2 particles cm^{-2} s^{-1} (1 ml min^{-1}), 1.4 ± 0.3 x 10^3 particles cm^{-2} s^{-1} (2 ml min^{-1}) and 2.3 ± 0.6 x 10^3 particles cm^{-2} s^{-1} (4 ml min^{-1}). The values of k_t are calculated to be 2.1 x 10^{-5} cm s^{-1} (1 mL min^{-1}), 3.0 x 10^{-5} cm s^{-1} (2 mL min^{-1}) and 4.3 x 10^{-5} cm s^{-1} (4 mL min^{-1}) giving fluxes of particles to the surface of 1.5 x 10^3 particles cm^{-2} s^{-1}, 2.1 x 10^3 particles cm^{-2} s^{-1} and 2.9 x 10^3 particles cm^{-2} s^{-1}. The measured adsorption rates and calculated fluxes are generally in good agreement here, indicating a primarily mass transport controlled process. At this timescale all of the adsorption rates are approximately linear, indicative of a low surface coverage regime due to the much lower number of particles in the suspension, compared to the 200 nm particles.

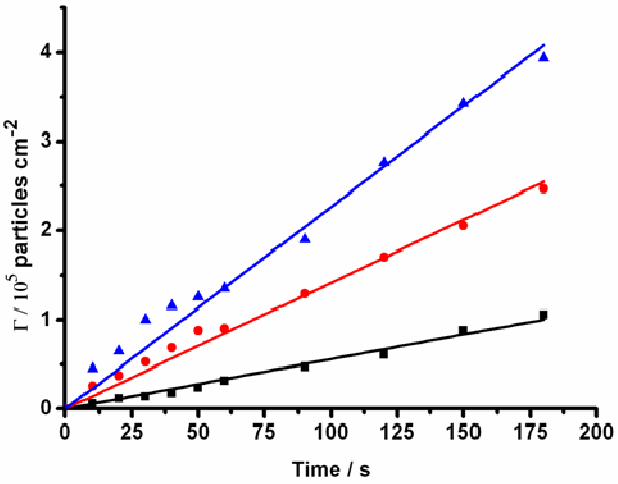

Figure 4.9. Surface concentration as a function of time for 0.005 % by mass 1.1 µm particles on PLL with 10 mM NaCl concentration, using impinging jet flow cell set-up. Initial adsorption fitted linearly for 1 ml min^{-1} flow rate (black), 2 ml min^{-1} flow rate (red) and 4 ml min^{-1} flow rate (blue).

4.3.6 Development of a vertical flow cell based on a SECCM probe.

In order to reduce the scale of measurements to that of a single cell, it is necessary to miniaturise the microfluidic delivery system. Here we propose the use of a theta capillary, in a scanning electrochemical cell microscopy configuration. The means of mass transport in this system differs to the impinging jet configuration used above. Here, the introduction of a bias between these electrodes allows migration of charged species in a controlled manner, *i.e.* relative to the bias applied, rather than using the flow of solvent, as in the earlier system.

It was first necessary to trial this system on model surfaces. The same carboxylate-modified (negatively-charged) particles were used and

electrostatically favourable (positively-charged, PLL) and unfavourable (negatively-charged, PGA) surfaces prepared as above. The size of the theta capillary aperture can be easily tailored via manipulation of parameters on the laser pipette puller, for 1.1 µm particles on these model surfaces an overall diameter of ~20 µm was chosen, giving two identical barrels of ~10 µm acting as inlet and outlet. Figure 4.9 shows the adsorption *vs.* time behaviour of these particles on the two surfaces as a function of potential between barrels. It is clear that the electrostatically-favourable surface has a much higher adsorption rate than the electrostatically-unfavourable surface, as expected. On PLL (Figure 4.10 (a)) the adsorption is essentially linear with respect to time, as would be expected in a low coverage regime. There is an increase in adsorption rate with increasing potential between barrels, corresponding to a higher flux of particles to the surface. The adsorption rates for each bias were calculated to be, on PLL, 1.2 ± 0.1 particles per minute (100 mV), 2.8 ± 0.2 particles per minute (200 mV) and 4.8 ± 0.2 particles per minute (500 mV). The observed increase in adsorption rate with barrel bias does not appear to be quite linear; with a large increase (approximately two times) from 100 mV to 200 mV, but a slightly more modest increase from 200 mV to 500 mV. However, for the narrow range of potentials studied, the relationship between adsoprtion and barrel bias can be considered to be approximately linear.

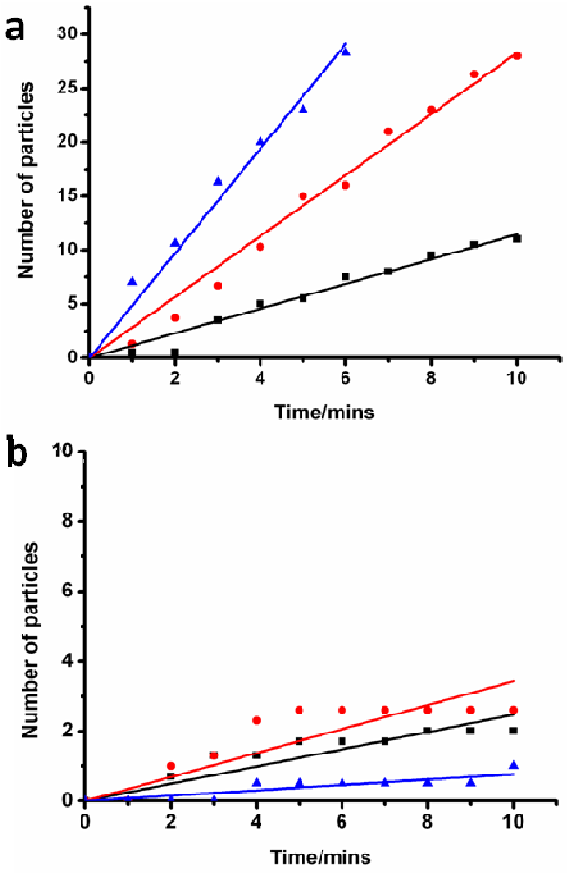

Figure 4.10. Adsorption *vs*. time plots for 1.1 µm carboxylate-modified particles on a) PLL- and b) PGA-modified surfaces. Solution used contained 0.001% particles and 1 mM KCl as background electrolyte. Biases between barrels were 100 mV (black), 200 mV (red) and 500 mV (blue). Values are shown as an average of multiple readings with the same probe.

For the PGA surface (Figure 4.10 (b)) the rates were calculated to be 0.2 ± 0.2 particles per minute (100 mV), 0.3 ± 0.2 particles per minute (200 mV) and 0.2 ± 0.1 particles per minute (500 mV). It is striking that these are much lower than for PLL with no real dependence on flux to the surface. The electrostatic interaction here is clearly very important, proving

this configuration is feasible for use as a flow cell in adsorption experiments. In these experiments the adsorption rate is very low when compared to the PLL surface and there is little difference between the flow rates.

In order to calculate the ratio of particles adsorbing to the surface of those which are delivered, the average flux of particles was approximated from the modelled potential field at the end of the tip (as described in section 4.2.9). Here one barrel was considered the outlet and the potential gradient across this point was used to calculate the average velocity of each particle and hence the flux to the surface. The average electrophoretic mobility, μ_e, of each particle was measured to be 2.98 x 10^{-8} m^2 s^{-1} V^{-1}. The average flux of particles was calculated to be 0.9 ± 0.4 particles per minute (100 mV), 1.9 ± 0.9 particles per minute (200 mV) and 4.6 ± 2.2 particles per minute (500 mV), with the errors based on the range of experimental currents measured. These values are very similar to those measured on PLL, indicating that the majority of particles delivered to the surface adsorb to the electrostatically favourable surface.

The nature of this adsorption is also important however: Figure 4.11 shows a CLSM image of the adsorbed particles in both the meniscus and following withdrawal of the capillary. It is apparent that the particles preferentially adsorb at the 3-phase boundary between the fluid, solid and air. However, from Figure 4.9 it is clear the nature of the surface has a large effect on this adsorption. When the probe is withdrawn it is clear the

particles have some (small) degree of mobility as the droplet is withdrawn and tend to aggregate together more.

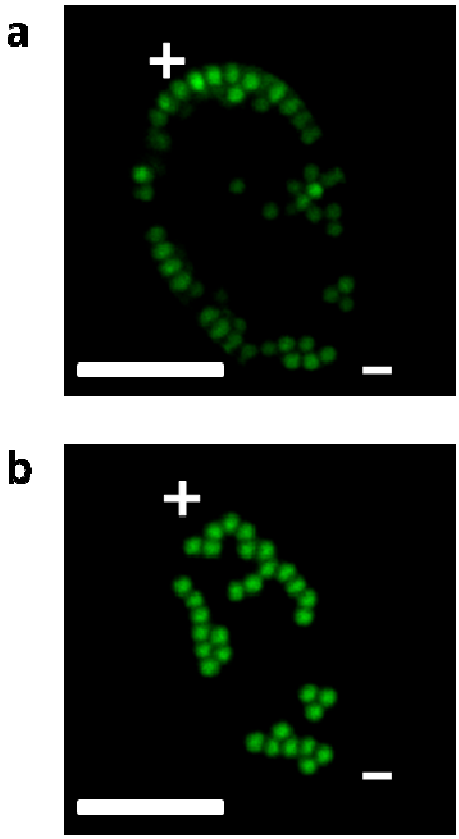

Figure 4.11. The nature of adsorption of the 1.1 µm carboxylate-modified particles to a PLL surface at 200 mV after 10 minutes with a) in the meniscus and b) following withdrawal of the probe. It is clear adsorption is preferential at the edge of the meniscus, at the phase boundary between the fluid, solid and air. Scale bars denote 10 µm.

The reason for the preferential adsorption at the 3-phase boundary is likely to be partly due to the lowest potential field gradient (*i.e.* the slowest movement of the particles). This is shown in the simulation in Figure 4.12 showing a strong correlation to this behaviour with the lowest

potential field gradient (and, hence, the slowest particle velocity) corresponding to the areas of highest adsorption. There is likely also an effect from the greater stabilization at the three-phase boundary.

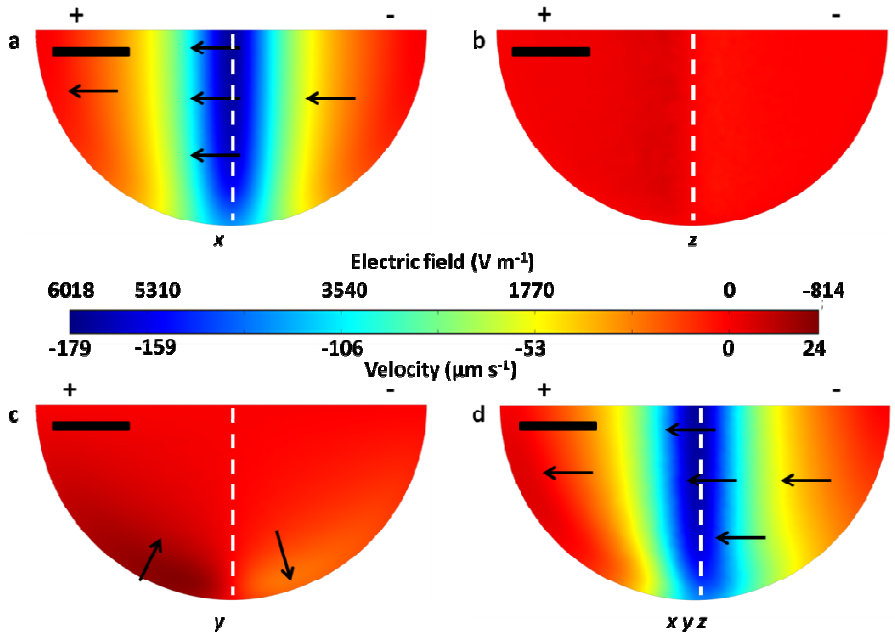

Figure 4.12. The simulated potential field gradient and particle velocity at the surface/meniscus boundary shown for a 200 mV bias (corresponding to an average current of 4.09 ± 1.96 nA). Showing (a) the *x* component, (b) the *y* component, (c) the *z* component and (d) the net velocity. The arrows indicate the direction of the particle movement and the dotted lines indicate the direction of the septum. Scale bars denote 4 µm.

It is also important to examine the effect of removal of the meniscus confinement on the adsorption. Figure 4.13 shows the same experiment performed in Figure 4.11 but into a much larger droplet (effectively bulk solution). Two observations are immediately apparent; the particles spread out considerably from the tip and the particle deposition is,

to some extent, directional. It should be noted here that the total deposition field extends over a much greater range (100s of µm), however resolution of the particles is difficult at this larger scale. This behavior can be explained by modeling the potential field around the probe apex in solution (Figure 4.14). Here it is apparent the major migratory flux is outwards from the negatively charged barrel into bulk solution, with 7 out of 10 particles visible in this direction.

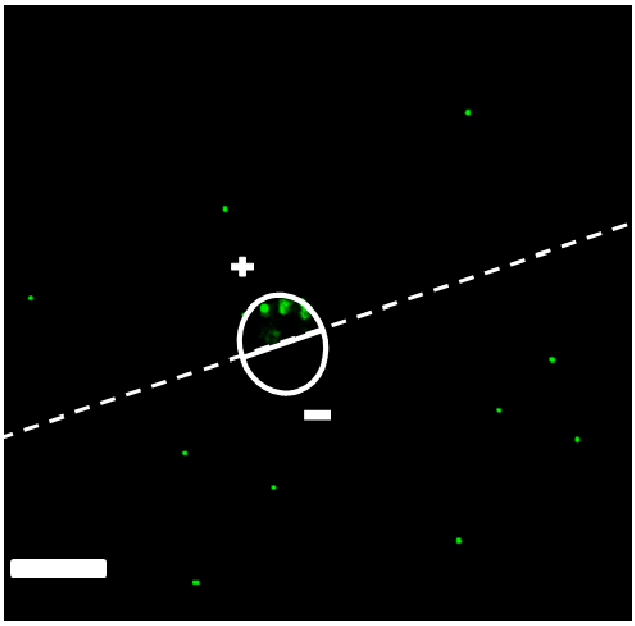

Figure 4.13. The effect of removing the meniscus confinement on particle adsorption. Scale bar denotes 100 µm. Conditions identical to Figure 4.11, *i.e.* 200 mV bias for 10 minutes. The dotted line indicates the direction of the septum. Note that the particles on the tip are adhered to the tip itself not the surface.

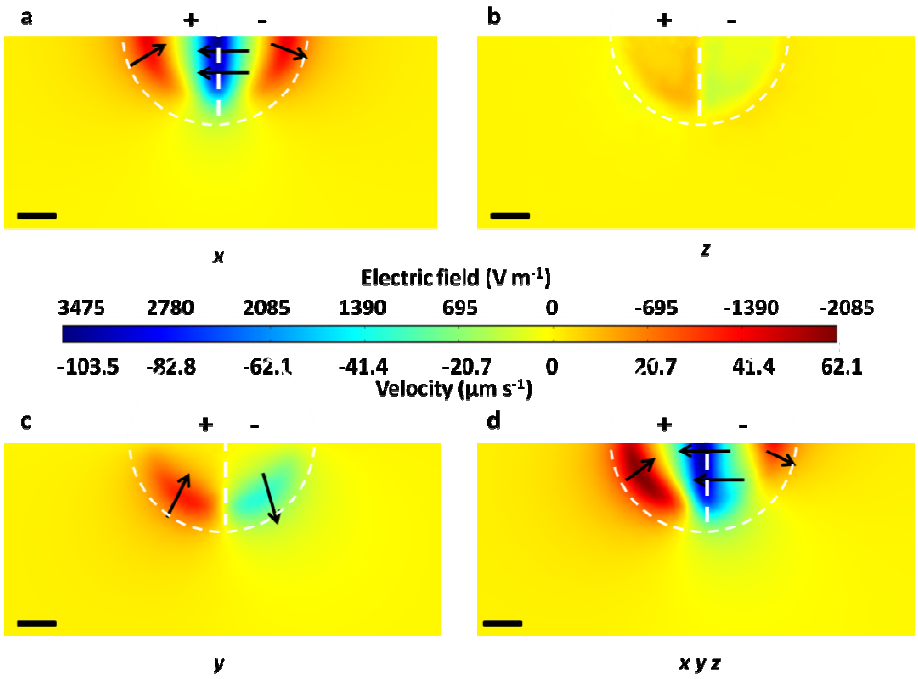

Figure 4.14. The simulated potential field gradient and particle velocity at the substrate surface shown in bulk experiments for a 200 mV bias (corresponding to an average current of 4.09 nA). Showing (a) the *x* component, (b) the *y* component, (c) the *z* component and (d) the net velocity. The arrows indicate the direction of the particle movement and dotted lines indicate position of the capillary walls and septum. Scale bars denote 4 microns.

4.3.7 Using the vertical flow cell to deliver species to biological interfaces.

Having investigated the use of a SECCM-type probe as a particle delivery system, it was then necessary to apply it to an actual individual cell. Here it was necessary to tailor the size of the probe to that of the cell in question. The *Zea mays* root hair cells in question are approximately 10-

15 µm in width, and so a 10 µm probe diameter was chosen. Figure 4.15 shows the resulting root hair cell following delivery of particles in three areas using a 0.0005% particle solution in 1 mM KCl for 10 minutes at 200 mV barrel bias. It is clear that these particles show some adhesion to the root hair cell, with the number of particles adsorbing increasing towards the tip of the cell. The average deposition rate was found to be 0.47 ± 0.2 particles per minute. Unfortunately, the reduced size of the probe restricted the channel size. The 1.1 µm particles tended to block the smaller channels making quantitative analysis difficult. Also, reducing the size of the particles provided further problems; the contrast in a small meniscus made it difficult to resolve smaller particles. However, it is clear that the root surface provides an adhesive surface for such particles more akin to the PLL than the PGA surface.

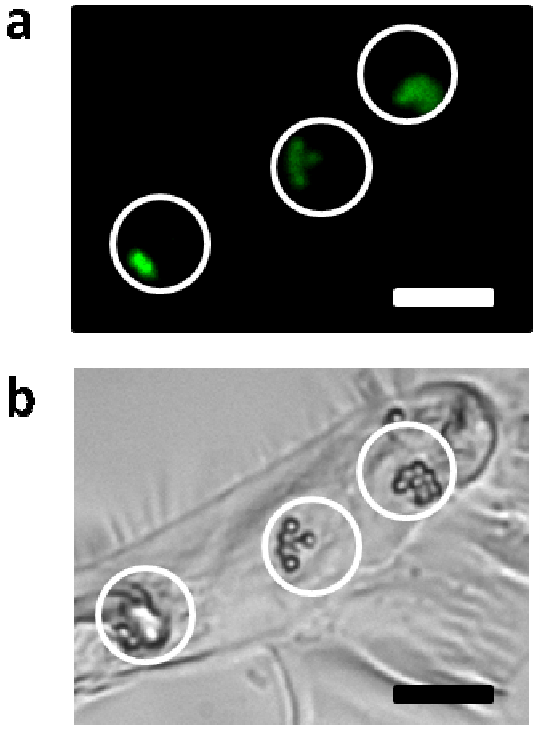

Figure 4.15. Root hair cell following delivery of 1.1 µm carboxylate-modified particles to three separate areas. a) CLSM image and b) brightfield microscopy image. Deposition conditions of 0.0005% particle solution in 1 mM KCl for 10 minutes at 200 mV barrel bias. The approximate position of the capillary is denoted by the white circles. Scale bars denote 10 µm.

In addition to particles, this delivery system was also trialled for other species. Here negatively-charged polymer molecules were chosen to test the viability of this delivery system combined with fluorescence measurement using CLSM. Figure 4.16 shows the adsorption rates, measured by normalised fluorescence, of two polymer molecules consisting of (a) copolymerized 2% rhodamine functionality/98% sulphonate functionality and (b) copolymerised 4% rhodamine functionality/96% sulphonate functionality respectively. The rhodamine

here is considered as a potential root adhesive (from unpublished work). Here the fluorescent intensity is normalised to the intensity of the droplet of solution at the apex of the probe, giving a qualitative assessment of the relative adsorption of the two polymers. It is clear that there is a much increased rate of adsorption of (b) with respect to (a). The average increase in normalised fluorescent intensity was found to be 3.1 ± 1.5 times for (a) and 7.8 ± 1.8 times for (b). Based upon the fluorescent intensity related to the concentration of the bulk solution, it is possible to estimate the concentration on the surface. Here the accumulation of polymer on the surface (and in the cell wall) relates to an effective concentration of 1.98 mM for (a) and 4.13 mM for (b).

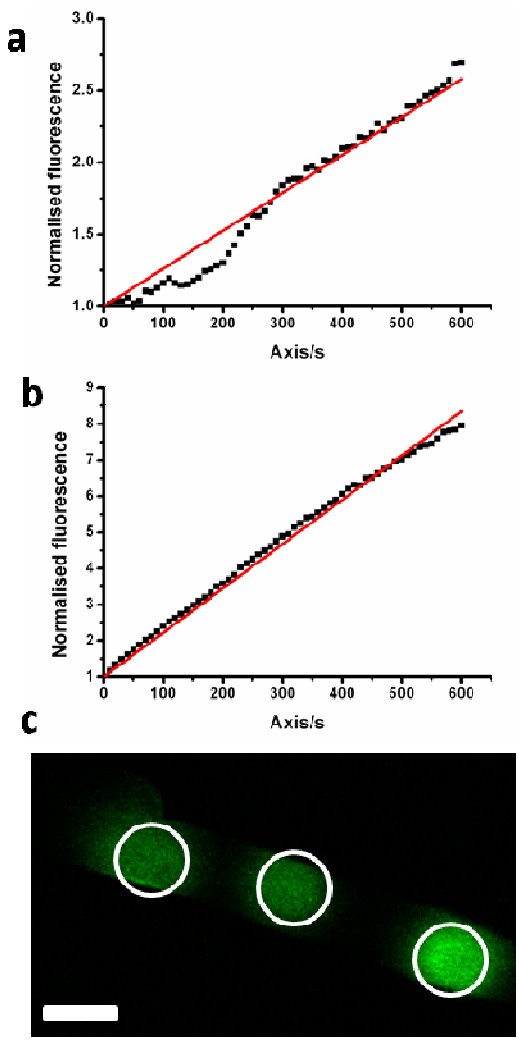

Figure 4.16. Adsorption rates measured by normalised fluorescent intensity for polymers containing a) 2% Rhodamine functionality/98% sulphonate functionality and b) 4% Rhodamine functionality/98% sulphonate functionality respectively at 500 mV barrel bias for 10 minutes at 1 mg mL^{-1} concentration (giving bulk concentrations of 0.64 mM and 0.53 mM respectively). c) shows the resulting CLSM image of a root hair cell following delivery of polymer (b) to three separate areas. The approximate position of the capillary is denoted by the white circles. Scale bar denotes 10 µm.

4.4 Conclusions

CLSM has been used to probe initial adsorption rates of negatively-charged particles to cellulose surfaces as a function of bulk ionic concentration, showing the adsorption rates are similar to those for an electrostatically repulsive surface (PGA) and lower than for an electrostatically attractive surface (PLL) for both 1.1 μm and 200 nm particles. The cellulose surface is readily formed on glass and is optically transparent allowing CLSM to be used to probe these adsorption rates. CLSM allows measurement of adsorption rates by both particle counting and changes in fluorescent intensity, coupled to the ability to view only a very shallow focal plane. These studies are then extended to the study of adsorption kinetics of the fastest measured adsorption rate (*ie* the PLL surface) via incorporation of an impinging jet flow cell to the CLSM set-up. From this a surface-controlled rate can be measured and an initial kinetic rate constant, k_i, for 200 nm particles extracted. Experiments performed under the same conditions for 1.1 μm particles were found to be mass transport controlled.

Finally, a microscale vertical flow cell was trialled with the target of local delivery to parts of an individual cell. Initial experiments on model surfaces confirmed the viability of this method on surfaces of attractive and repulsive charge. Finite element modeling was used to explain the nature of adsorption, with good correlation to the experimental data both in terms of

rates and location of adsorption. The system was then shown to be able to deliver controllably both particles and polymers to individual root hair cells.

4.5 References

(1) Adamczyk, Z.; Siwek, B.; Zembala, M. *Journal of Colloid and Interface Science* **1992**, *151*, 351.

(2) Adamczyk, Z.; Warszynski, P. *Advances in Colloid and Interface Science* **1996**, *63*, 41.

(3) Bohmer, M. R.; van der Zeeuw, E. A.; Koper, G. J. M. *Journal of Colloid and Interface Science* **1998**, *197*, 242.

(4) Kleimann, J.; Lecoultre, G.; Papastavrou, G.; Jeanneret, S.; Galletto, P.; Koper, G. J. M.; Borkovec, M. *Journal of Colloid and Interface Science* **2006**, *303*, 460.

(5) Goransson, A.; Tragardh, C. *Journal of Colloid and Interface Science* **2000**, *231*, 228.

(6) Johnson, C. A.; Lenhoff, A. M. *Journal of Colloid and Interface Science* **1996**, *179*, 587.

(7) Dokou, E.; Barteau, M. A.; Wagner, N. J.; Lenhoff, A. M. *Journal of Colloid and Interface Science* **2001**, *240*, 9.

(8) Wasilewska, M.; Adamczyk, Z. *Langmuir* **2011**, *27*, 686.

(9) Klemm, D.; Heublein, B.; Fink, H.-P.; Bohn, A. *Angewandte Chemie International Edition* **2005**, *44*, 3358.

(10) Rehfeldt, F.; Tanaka, M. *Langmuir* **2003**, *19*, 1467.

(11) Schaub, M.; Wenz, G.; Wegner, G.; Stein, A.; Klemm, D. *Advanced Materials* **1993**, *5*, 919.

(12) Kontturi, E.; Tammelin, T.; Osterberg, M. *Chemical Society Reviews* **2006**, *35*, 1287.

(13) Kaigala, G. V.; Lovchik, R. D.; Drechsler, U.; Delamarche, E. *Langmuir* **2011**, *27*, 5686.

(14) Cortes-Salazar, F.; Lesch, A.; Momotenko, D.; Busnel, J. M.; Wittstock, G.; Girault, H. H. *Anal. Methods* **2010**, *2*, 817.

(15) Momotenko, D.; Cortes-Salazar, F.; Lesch, A.; Wittstock, G.; Girault, H. H. *Analytical Chemistry* **2011**, *83*, 5275.

(16) Le, H. P. *J. Imaging Sci. Technol.* **1998**, *42*, 49.

(17) Piner, R. D.; Zhu, J.; Xu, F.; Hong, S. H.; Mirkin, C. A. *Science* **1999**, *283*, 661.

(18) Bard, A. J.; Fan, F. R. F.; Kwak, J.; Lev, O. *Analytical Chemistry* **1989**, *61*, 132.

(19) Amemiya, S.; Bard, A. J.; Fan, F.-R. F.; Mirkin, M. V.; Unwin, P. R. In *Annual Review of Analytical Chemistry* 2008; Vol. 1, p 95.

(20) Hansma, P. K.; Drake, B.; Marti, O.; Gould, S. A. C.; Prater, C. B. *Science* **1989**, *243*, 641.

(21) Bruckbauer, A.; Ying, L.; Rothery, A. M.; Zhou, D.; Shevchuk, A. I.; Abell, C.; Korchev, Y. E.; Klenerman, D. *Journal of the American Chemical Society* **2002**, *124*, 8810.

(22) Bruckbauer, A.; James, P.; Zhou, D.; Yoon, J. W.; Excell, D.; Korchev, Y.; Jones, R.; Klenerman, D. *Biophysical Journal* **2007**, *93*, 3120.

(23) Williams, C. G.; Edwards, M. A.; Colley, A. L.; Macpherson, J. V.; Unwin, P. R. *Analytical Chemistry* **2009**, *81*, 2486.

(24) Ebejer, N.; Schnippering, M.; Colburn, A. W.; Edwards, M. A.; Unwin, P. R. *Analytical Chemistry* **2010**, *82*, 9141.

(25) Snowden, M. E.; Guell, A. G.; Lai, S. C. S.; McKelvey, K.; Ebejer, N.; O'Connell, M. A.; Colburn, A. W.; Unwin, P. R. *Analytical Chemistry* **2012**.

(26) Lai, S. C. S.; Dudin, P. V.; Macpherson, J. V.; Unwin, P. R. *Journal of the American Chemical Society* **2011**, *133*, 10744.

(27) O'Connell, M. A.; de Cuendias, A.; Gayet, F.; Shirley, I. M.; Mackenzie, S. R.; Haddleton, D. M.; Unwin, P. R. *Langmuir* **2012**, *28*, 6902.

(28) Tanaka, M.; Kaufmann, S.; Nissen, J.; Hochrein, M. *Physical Chemistry Chemical Physics* **2001**, *3*, 4091.

(29) Powell, H. V.; O'Connell, M. A.; Zhang, M.; Mackenzie, S. R.; Unwin, P. R. *Analytical Chemistry* **2012**.

(30) Zhang, M.; Powell, H. V.; Mackenzie, S. R.; Unwin, P. R. *Langmuir* **2010**, *26*, 4004.

(31) Bitziou, E.; Rudd, N. C.; Edwards, M. A.; Unwin, P. R. *Analytical Chemistry* **2006**, *78*, 1435.

(32) Evans, J. W. *Reviews of Modern Physics* **1993**, *65*, 1281.

(33) Amatore, C.; Szunerits, S.; Thouin, L.; Warkocz, J. S. *Journal of Electroanalytical Chemistry* **2001**, *500*, 62.

(34) Macpherson, J. V.; Marcar, S.; Unwin, P. R. *Analytical Chemistry* **1994**, *66*, 2175.

Chapter 5. Use of high resolution electrochemical scanned probe microscopy (EC-SPM) methods for study of *Zea mays* root hair cell structure and activity

This chapter concerns the application of cutting edge EC-SPM technologies to the study of plant cells, primarily the root hair cells of the *Zea mays* (common corn) plant. A number of techniques are used which are considered for the different chemical and physical information they can provide and their applicability to living, delicate systems.

Firstly, this chapter considers the preparation of viable live samples for study via SPM. Here, it is vital that the sample is surface bound to allow such investigation. Also, the cells in question need to be viable, *i.e.* living and undamaged. Detached cells are used for high-resolution structural analysis via AFM, and, later root hair cells still connected to the entire root system are prepared for analysis via non-contact EC-SPM techniques. These cells are shown to be living via 'vital staining' experiments using fluorescein diacetate, a commonly-used cytoplasmic enzymatic indicator.

Various EC-SPM techniques are trialled for imaging experiments. Initially, intermittent contact-scanning electrochemical microscopy (IC-SECM) is used to detect intracellular activity via the ferricyanide/ferrocyanide redox

couple over large sections of the root surface. Though spatial variations are detected, two main drawbacks are noted; limited spatial resolution inherent to the probes used and interaction and damage to the plant caused by this technique. Secondly, scanning electrochemical cell microscopy (SECCM) is used which overcomes these issues via smaller probes and contact via only an aqueous meniscus. However, here the ionic behaviour is dominated via the exchange between a dry system and the solution filled capillary, meaning transient changes during scanning and difficulty in interpretation.

Finally, scanning ion conductance microscopy (SICM) is used to study localised ionic fluxes to and from root hair cells as a function of ionic strength of bathing solution. This technique combines high resolution and non-contact imaging. Combined SECM-SICM probes are then used to complement SICM-only data by the additional measurement of Faradiac currents associated with cellular activity using the ferricyanide/ferrocyanide redox couple.

5.1 Introduction

The use of electrochemical scanned probe techniques is becoming increasingly widespread in the biological sciences.[1-11] Studies can generally be grouped into two categories. The first category involves the detection of redox-active species, generally by SECM. The second involves primarily non redox-active species to provide topographical and ion content information, generally by SICM.

SECM has been particularly prevalent in the study of biological samples, with a diverse range of systems studied. These vary from mimetic systems, where supported lipid bilayers (SLBs) have been studied in some detail with, for example, topography,[12] permeation of ions through the SLB[13] and transport of ions through individual ion channels.[14] Dental samples are another possibility; local permeability measurements have been performed on dentine, for example,[15-18] with resolution sufficient to study individual microtubules (~2 μm).[15,19] Immobilised enzymes have been the subject of multiple studies, a few examples include glucose oxidase,[20-24] horse radish peroxidase[25,26] and diaphorase.[25,27] Amperometric oxygen detection is another common system studied, with oxygen evolution as a result of photosynthesis in plant leaf cells being one example.[28-34] Other cellular processes can also be studied. For example, respiration can either be detected by local oxygen concentrations,[34,35] or via redox species capable of participating in the electron transport chain.[35-38] Examples of cells studied include cultivated cancer cells[35] and bacteria such as *Esherichia Coli*,[36,38] *Staphylococcus aureus*[39] and *Paracoccus denitrificans*.[40]

SICM can also be used for biological study. The two main areas of interest are (mainly) in non-contact topographical imaging, for both static and dynamic systems, and, occasionally, stimulated cellular processes. Volumetric imaging of cells is possible,[8] while many studies characterise cell surfaces at higher resolution.[41-44] Real time and dynamic imaging is also possible with cells of interest including cardiac myocytes,[6,45-48] kidney cells[7,49] and spermatozoa.[50] Examples of cellular stimulation in these studies include exposure of cardiac myocytes to extracellular Ca^{2+} ions[45] and combining with patch clamp apparatus to isolate single ion channels.[51]

More recent studies have combined techniques in order to elucidate more information or to improve control of tip-sample interactions so as to perform higher resolution measurements. SECM-SICM is a particularly promising technique, combining the benefits of both. To date, only a few studies have been conducted but have considered diverse samples, such as immobilised enzymes (glucose oxidase (GOD) and horse radish peroxidise (HRP))[52] and a variety of live cells, including cardiac myocytes, superior cervical ganglion (SCG) [52] and sensory neurons.[53]

One use of these EC-SPM techniques is for the measurement of ionic fluxes, which is an essential aspect of many fields across the physical and biological sciences, one of particular interest being cell biology.[54-57] When studying fluxes from small structures, such as cells, it is vital to utilize technologies providing microscale and nanoscale information, in order to probe localised heterogeneities, for example to probe uptake rates or mass transport effects.

Whereas the most popular method is SECM, this technique requires a redox active species to be present for electrochemical detection. Note that although ion selective electrodes can also be used in SECM, they have not found widespread use due to difficulties in positioning SECM tips without an independent feedback control. An alternative approach is to employ SICM. As this is used to measure purely ionic (migrational) currents between a single microscale or nanoscale pipet and a reference electrode in bulk solution, a measurable signal can potentially be measured for any charged species. Though this technique is often used for non-contact topographical imaging, the ability to probe varying ion currents, such as from ion channels in cells, can be utilized.[58]

Also, as a non-contact technique performed in a bathing solution this technique is particularly suitable for biological measurements.

The accurate measurement of ionic fluxes using a scanning technique is, however, not trivial. The measured ion current is also used as the imaging (feedback) set point, resulting in a convoluted signal between the local ionic flux from the surface and the hindering of the migration current from bulk solution. Often a vertically oscillating probe is used with the first harmonic (alternating current) component used as the imaging set point, however, as this magnitude is also based essentially on the shape of the approach curve, it cannot solve the issue of convolution between the two competing processes. Clearly, the raw current measured cannot provide true topography from constant tip-sample separation (and subsequently an ion current deconvoluted from topography) on surface of heterogenous activity.

A more recent implementation of the SICM is that of 'hopping mode' a technique that performs an approach curve at every imaging point. One advantage of this method is it allows topographical imaging of very large features but far more information can potentially be gleaned from analysing each approach curve. There have been various theoretical approaches to understand current measurement inside micro- and nano-pipets[59,60] but modeling of realistic SICM conditions is more limited.[61] This work models approach curves, with respect to the tip geometry and sample topography, but hitherto has only considered purely inert surfaces.

As mentioned above, ion fluxes are of interest in a number of fields. In biology, both active and passive mechanisms exist for ion influx and efflux from individual cells.[62-66] Certain cells are specialized for their role in the uptake of

species from their outer environment. One example of such is the root hair cell (see Chapter 1.1), a specialized cell present in plant root systems with a tubular geometry giving a high surface area for uptake from the local soil environment. These cells have the function of absorbing almost all nutrients the plant needs and such provide an insightful system for ion flux studies.

Herein, individual root hair cells are studied using a range of SPM techniques. Firstly, AFM is used for topographical and structural information, followed by a range of EC-SPM techniques which are then evaluated for their applicability. The viability of the root hair cells is ensured via vital staining experiments using fluorescein diactetate. IC-SECM and SECCM are used for initial EC-SPM studies on *Zea mays* root cells. Later, SICM is employed to study localized ion fluxes from *Zea mays* root hair cells. Hopping mode is employed to capture approach curves at every imaging point using the alternating current (AC) component of an oscillating tip as the imaging set point as a function of bathing solution concentration to probe changes in local solution conductivity as a means of probing ion fluxes associated with individual root hair cells.

5.2 Experimental

5.2.1 Chemicals

All chemicals were purchased from Sigma-Aldrich at the highest purity available. Salt solutions consisting of KCl, NaCl and $CaCl_2$ were variously used as imaging solutions and supporting electrolytes at concentrations ranging from 1

mM to 100 mM. For IC-SECM experiments potassium ferricyanide, $K_3Fe(CN)_6$, was used at a concentration of 5 mM.

5.2.2 Probe fabrication.

Probes were prepared variously from borosilicate glass single barrelled and theta capillaries (Harvard Apparatus, UK) and quartz single barrelled and theta capillaries (Sutter Instruments). They were pulled to an overall size of ~1 µm using a laser pipette puller (Model P-2000, Sutter Instruments, UK). For IC-SECM experiments 2 µm diameter platinum UME formed via sealing an etched Pt Wollaston wire in borosilicate glass and polishing back to expose the wire disk, were used. In order to form a stable meniscus for SECCM experiments, the outer walls of the pipettes were made hydrophobic using dimethyldichloromethane. Both barrels were then filled with the salt solution (~50 µL per barrel) and chlorodised silver wires (Ag/AgCl quasi reference electrode) were inserted into each barrel. For the SICM probes a single barrelled pipette was used in a similar way (without the need to silanise), also at ~1 µm overall diameter.

5.2.3 AFM Experiments

AFM imaging was performed using a Bruker-Nano Bioscope Catalyst operated in contact mode using NP-type standard silicon nitride probes. Imaging was undertaken in salt solutions of typically 10 mM NaCl. For such experiments it was necessary to detach the root hair cells from the plant and mount on a

collagen film formed on the base of a glass petri dish (Willco Wells, Netherlands) to ensure sufficient stability for structural imaging.

5.2.4. Fluorescent microscopy 'vital staining' experiments

Fluorescent imaging was performed using a combined fluorescence/laser scanning confocal microscope (Leica TCS SP5 X, Leica Microsystems) on an inverted microscope stand (DMI 6000, Leica Microsystems). Fluorescein diacetate (FDA) was dissolved in acetone (5mg mL^{-1}) which was further diluted with MillQ water at a ratio of 1 part FDA/acetone solution to 99 parts water. Imaging was performed using an I3 filter set with excitation between 450 and 490 nm and collection above 515 nm.

5.2.5 Root preparation

Zea mays seeds were germinated between two layers of damp paper at 25 °C for three days. This provided a root of approximately 10-20 mm in length with a dense layer of root hair cells (shown in Figure 5.1). Plants were then used at this stage to ensure consistency, with all nutrients for growth still provided by the seed. For EC-SPM imaging experiments, the roots were mounted on SPM adhesive tabs (Agar Scientific) which both secured the root sufficiently under fluid and supported individual root hair cells sufficiently for the EC-SPM techniques used.

Figure 5.1 *Zea Mays* seedling at three days old. The cap of the root and densely-packed root hair cells are visible. Scale bar denotes 5 mm.

5.2.6. IC-SECM Experiments

IC-SECM experiments were perfomed using a scanning system based on 100 µm *x*,*y* Physik Instrumente P-621.CL and 38 µm *z* P-753 LISA mounted on an inverted microscope for alignment (Zeiss Axiovert 25). Images were taken using a 2 µm Platinum UME in a solution consisting of 3 mM potassium ferricyanide in 100 mM potassium chloride supporting electrolyte.

5.2.7 SECCM Experiments

SECCM imaging experiments were performed on the scanning system described above. Transient experiments were performed on the 'newer' equipment described in Chapter 2.4. Here a scanning system based on 300 µm *x,y* piezo (Mad City Labs Nano-Bio 300) and a decoupled 38 µm *z* piezo (Physik Instrumente P-753 LISA) was used with the faster FPGA architecture. This system was mounted on a Zeiss Axiovert 40CFL fluorescence microscope for

alignment. Imaging was performed in 10 mM KCl and transient experiments were performed in 10 mM KCl.

5.2.8 SICM Experiments

SICM experiments were performed using the same configuration as described above. Scanning was performed in 'hopping mode' (*i.e.* a vertical approach at each point to an AC setpoint, followed by a retraction of 5 μm) in KCl solutions varying from 1 mM to 100 mM.

5.3 Results and Discussion

5.3.1 AFM characterisation of root hair cell surfaces

Firstly, the root hair cell surfaces were characterised using AFM. Due to the high contact forces related to AFM imaging, it was necessary to detach root hair cells from the greater root structure before imaging. Securing the cells on functionalised glass surfaces was found to be difficult, but this was overcome by mounting on a thin layer of collagen on top of the glass. Figure 5.2 shows three-dimensional representations of the root hair cell cap (the end of the cell representing a highly active area) and further back up the cell (representing the vast majority of the structure).

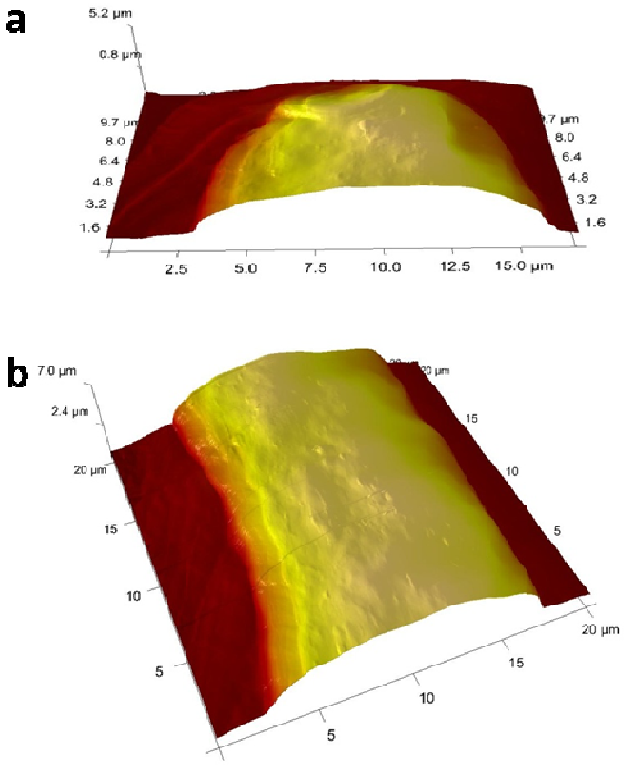

Figure 5.2 Contact mode AFM images of a detached root hair cell taken in 10 mM NaCl showing (a) the cap of the cell and (b) the surface of the cell between the cap and the body of the plant.

Here the 3-D structure of the root is obvious; despite being mounted on a flat surface the cells maintain a predominately tubular structure due to support from the external cell wall and internal sap vacuole. It can be seen that the surface is not completely smooth on the top of the cell; this roughness is shown in more detail in Figure 5.3.

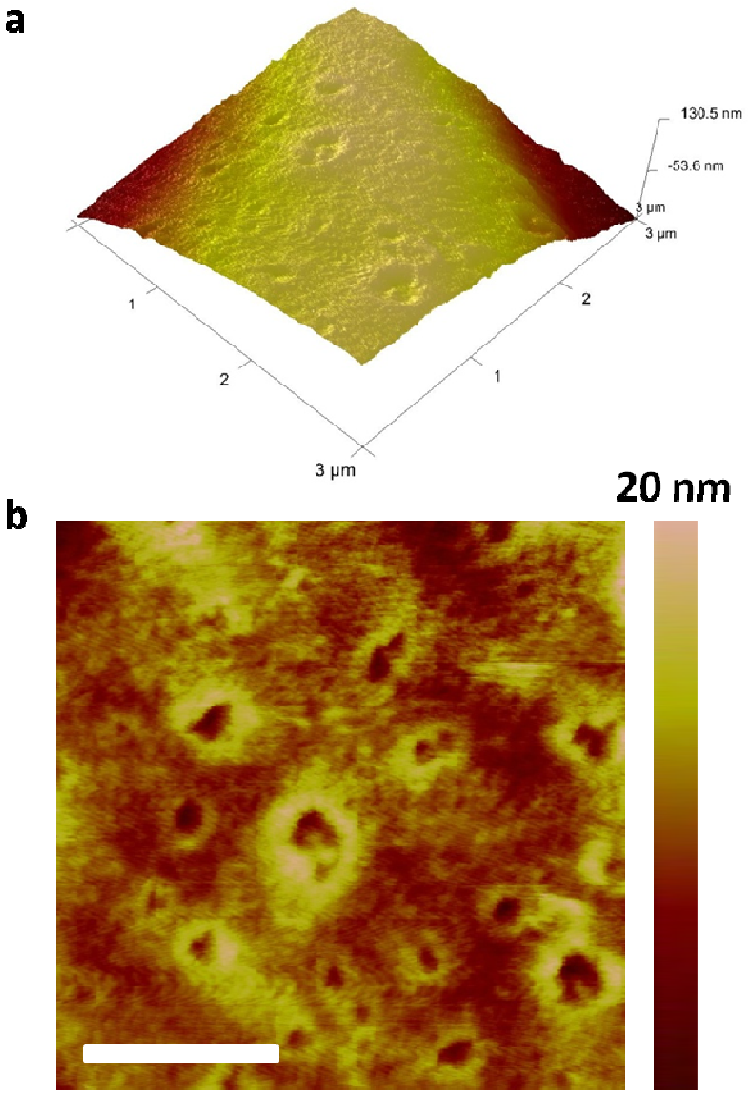

Figure 5.3. High resolution AFM images of the root hair cell surface taken in 10 mM NaCl, with (a) 3-D projection showing the curvature of the root with small pitting features and (b) plane fitted image of the same area. Scale bar denotes 1 µm.

From Figure 5.3 it is clear that small features are present on the surface of the root. From the contact mode AFM images these appear as shallow pits with diameters of 10s to 100s of nm. It is difficult to draw definitive conclusions due to both the large interaction force of the AFM probe on the soft cell surface and

the fact these cells need to be removed form the plant in order to support them for AFM imaging. However, it is clear that on the small scale there are heterogeneities on the cell surface, providing interesting possibilities for imaging with non-contact functional imaging techniques.

5.3.2 Root hair cell viability experiments

For EC-SPM imaging experiments it was advantageous to mount an entire root system to prevent any possible damage. Here, it was found to be possible to mount the entire root on just an adhesive tab, providing sufficient stability for the lower force EC-SPM imaging techniques. Firstly, for any uptake or activity measurements it is essential to ensure that the cells are living. A common means of this is by 'vital staining', using stains that will only fluoresce on interaction with living matter. In plant biology a commonly used stain is fluorescein diacetate.[67] Here the acetate functionalised fluorescein molecule is fluorescently inactive but is membrane mobile. On diffusion into the cell the acetate group is cleaved via cytoplasmic enzymes, leaving the free form of fluorescein which is fluorescent. Figure 5.4 shows the mounted root system imaged via fluorescent microscopy after treatment with fluorescein diacetate. The surface bound root hair cells can be clearly seen on this image, showing that they are viable for study.

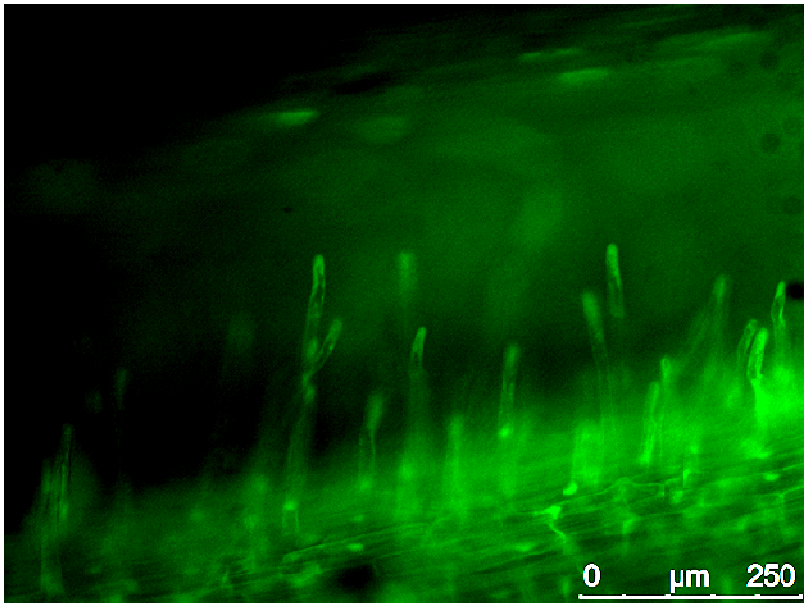

Figure 5.4. Surface bound root hair cells after treatment with 'vital stain' fluorescein diacetate. The cells can be seen emitting fluorescent light indicating that they are alive and viable for experiments.

5.3.3 IC-SECM experiments

For preliminary EC-SPM experiments, IC-SECM was chosen as a simple technique to determine whether such techniques can provide useful information from root cells. A simple cellular activity probe was chosen, that of ferricyanide reduction via intracellular NADH (a co-enzyme) activity. Here the ferricyanide (oxidised form of the redox couple) diffuses into the cell, is reduced to ferrocyanide which in turn diffuses out of the cell. The SECM probe is then held at the relevant potential in order to oxidise the ferrocyanide, which is then measured as a current. The IC-SECM technique involves physical contact with a surface and, as such, is unlikely to provide unambiguous information about cellular systems. However, it does provide a simple means of deconvoluting

topography from activity. As a technique with high tip-sample interaction force, individual cells were found to be too fragile. However, the top surface of the root provides a more robust surface. Figure 5.5 shows the current (activity) map from the top surface of the root. From this image there are clear heterogeneities in the activity of the root cells and justifies the use of more delicate and higher resolution EC-SPM techniques.

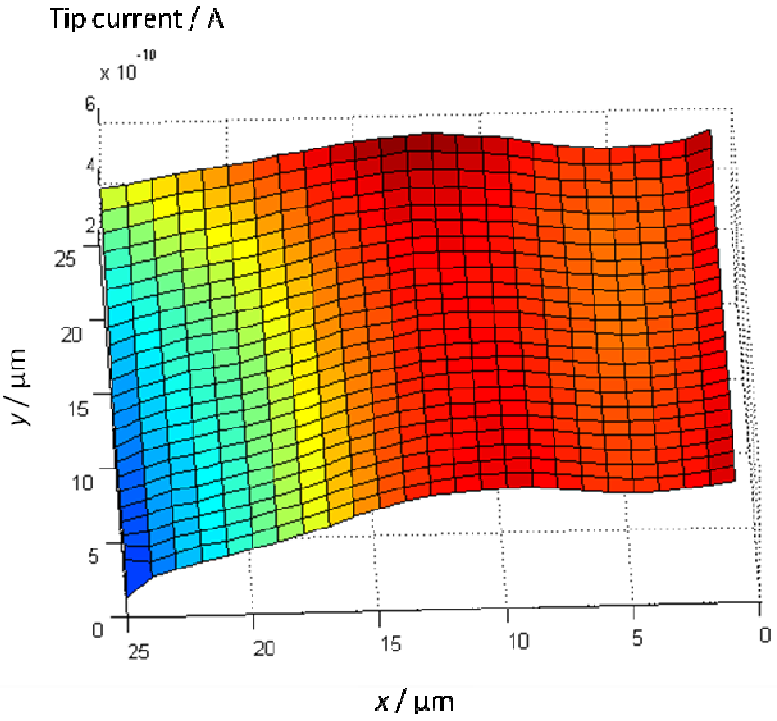

Figure 5.5. Activity map of localised ferrocyanide oxidation at a root surface.

5.3.4 SECCM studies on individual root hair cells

The next EC-SPM technique trialled was SECCM. In this configuration a migration current between the two barrels of a theta capillary is measured. This current is a function of solution conductivity (ion content) and separation between the probe (primarily the septum) and the surface. Exchange of ions (or water) between the root hair cell and the solution will change the conductivity of the solution and, thus, affect the migration current. Figure 5.6 shows an SECCM scan of a single root hair cell. In (a) there is a clear increase in migration current over the cell, which indicates higher solution conductivity when the tip is over the root. This is likely a combination of an efflux of ions from the cell and an influx of water into the cell. It is also clear there are areas of varying exchange across the root cell. Part (b) shows the topography of the sample. The small height changes here are clearly unrealistic when compared to the AFM images (Figure 5.2). This is perhaps unsurprising though as the wetting properties of the root surface will vary greatly from that of the support and also the feedback signal (Figure 5.6 (c)), which is based up the AC component of the migration current, shows a small change on and off the root.

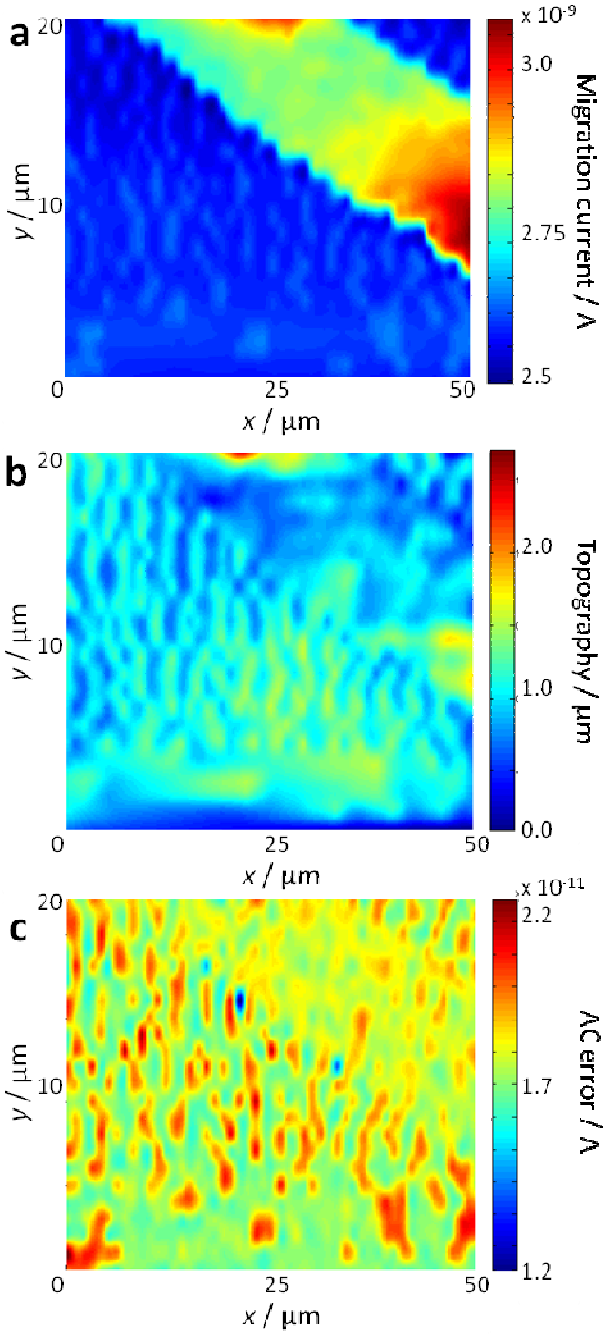

Figure 5.6. SECCM scans of a root hair cell showing (a) migration current, (b) topography and (c) alternating component of the migration current (feedback parameter). Tip filling solution consists of 10 mM KCl.

The transient current response on probe landing on the cell is shown in Figure 5.7. Two observations can be noted: Firstly, the migration current takes a significant amount of time to stabilise (part (a)), with the current rising for over 20 s and, secondly, much of the change is rapid (part (b)), with a change of over 0.5 nA in the first 10 ms on landing. As mentioned earlier the current response is the result of a combination of factors which can affect the ionic content (*i.e.* the conductivity) of the solution. This can be affected by ion (and water) flow into and out of the cell, and also any ions on the surface, dissolution of any materials dried onto the surface and ion rearrangement (*eg* double-layer formation) on landing. This is clearly the major drawback with this technique. It is an unrealistic environment for the vast majority of cells and it is likely that actual wetting characteristics will dominate any measured values. This issue could potentially be overcome in future with careful environmental control (especially humidity and temperature), which if properly resolved would create a wealth of information.

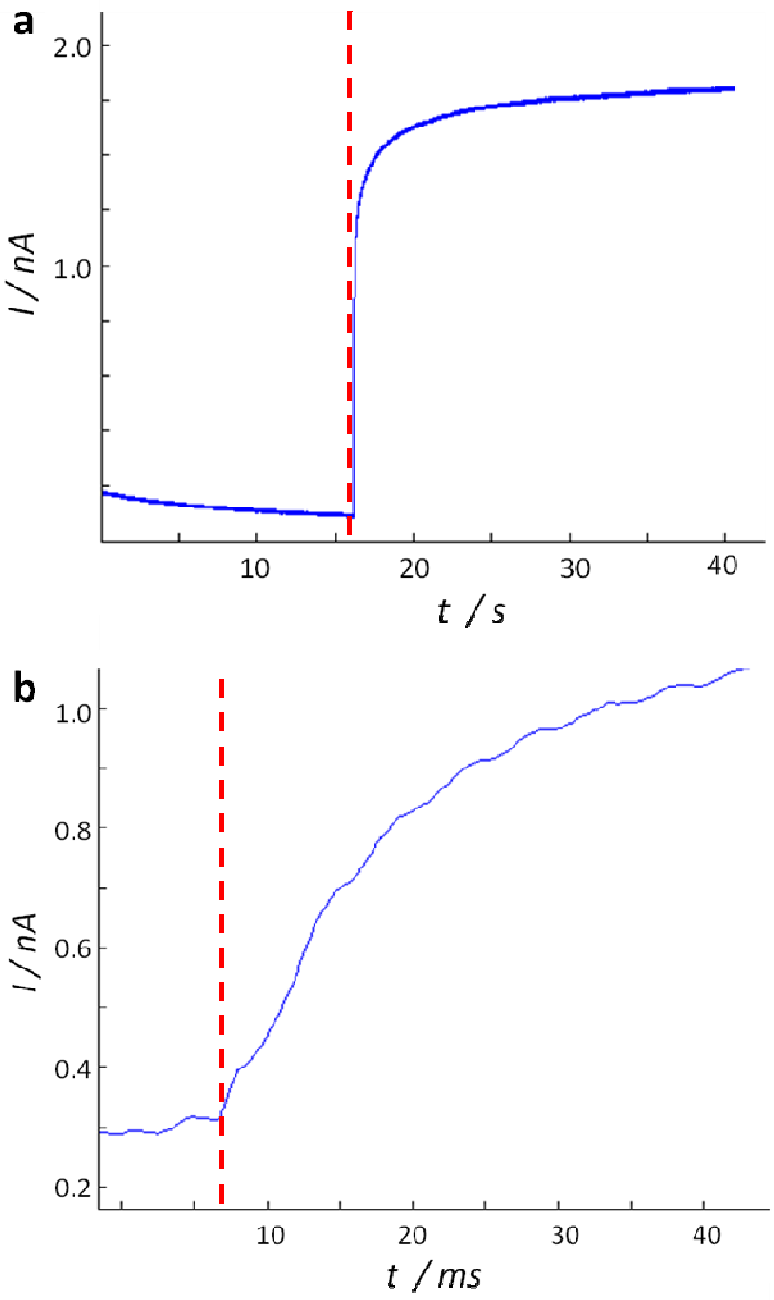

Figure 5.7. The migration current response on tip landing onto a root hair cell surface. (a) the current response on landing and (b) the initial change in current on landing. Pipette solution consists of 10 mM KCl. Landing indicated by dotted line.

5.3.5 SICM as a probe of ion fluxes at root surfaces

SICM is also used to measure local ion migration currents, generally as a feedback setpoint for topographical imaging. Clearly, in dynamic systems however, there will be variations in local ionic content which may affect this setpoint. This technique is particularly suited to biological measurements when compared to the previous techniques used, as imaging is non-contact and samples are completely immersed in bathing solution. Aside from topographical imaging, probing of local ion concentration (conductivity) is possible. The current measured is a combination of the solution conductivity and the additional resistance associated with the pipette aperture, both from the tip geometry and the separation from a surface. This current measured is consequently very sensitive to changes in conductivity at the pipette tip. The root hair cells, due to their vital role in ion uptake, are logically a good match for a technique that can probe this local conductivity (ionic concentration changes). The main concern here is care must be taken in interpretation, in particular in distinguishing between topography and conductivity.

Firstly, a root hair cell was imaged in a 10 mM KCl solution using a 'hopping' mode protocol, consisting of a series of 5 µm approaches of a vertically oscillating probe to an AC setpoint (generally of ~1 % of the total (DC) migration current). Figure 5.8 (a) shows the topography of the root, focussing on the very tip of the root hair cell. Part (b) shows the measured current, plotted as the difference between the start and end point of each 'hop' (approach curve). This current is particularly informative as it both provides a means of normalising against the bulk current measurement and also shows the how the

conductivity of the solution changes locally (*vide infra*). Parts (c) and (d) show two further measured components, namely the AC current (feedback setpoint) and (d) the phase shift of this component. Here it is apparent that the AC component is constant (as would be expected) and that there is a phase shift on and off the cell, and also some shift around the edges of the cell.

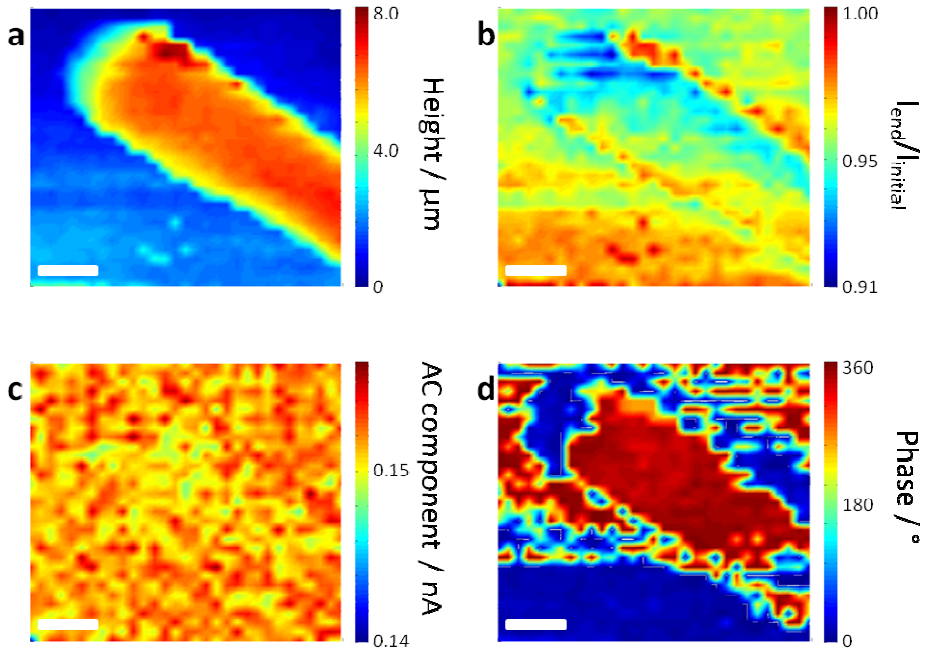

Figure 5.8. SICM imaging of a root hair cell in 10 mM KCl solution showing (a) topography, (b) the change in DC current between the start and end of the approach, (c) the AC component of the current (feedback setpoint) and (d) the phase of the AC component of the measured current. Scale bars denote 5 µm.

Figure 5.9 and 5.10 consider the same experiments at concentrations an order of magnitude higher and lower; *i.e.* with bathing solution concentrations of 1 mM KCl and 100 mM KCl, respectively. The topography is generally similar

for all three concentrations (parts (a)), however the change in the migration current on the cell compared to the surface is clear (parts (b)). As the ionic concentration of the bathing solution increases the change in the measured current decreases, to the point of a modest increase in measured current on the cell for the 100 mM KCl bathing solution compared to the surface around it. The AC component (parts (c)) for each image invariably shows little change, as would be expected for a hopping mode but nevertheless showing stable imaging. Finally the phase shows the clearest shift for the 1 mM concentration which becomes less obvious with increasing ionic concentration.

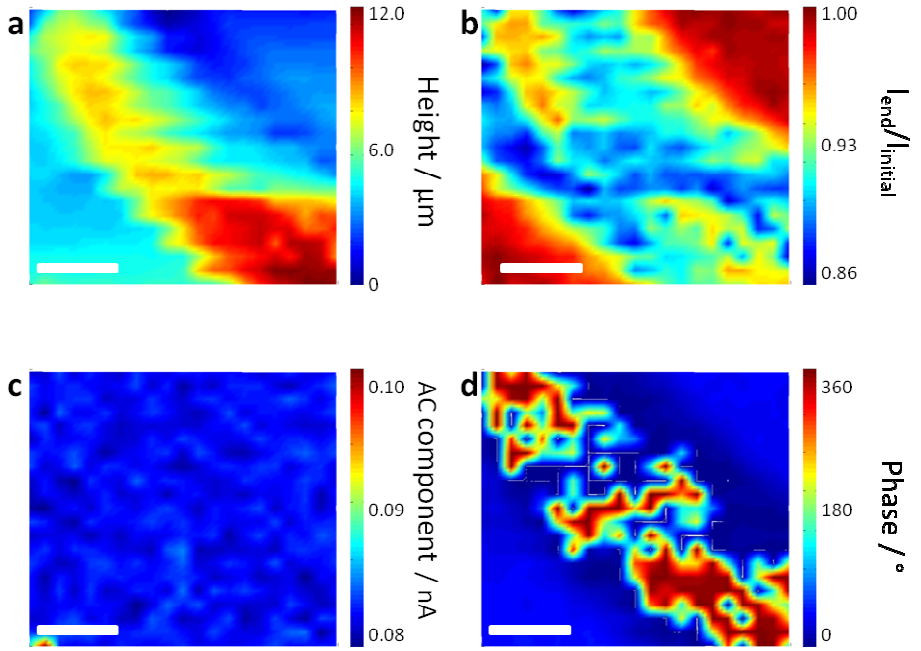

Figure 5.9. SICM imaging of a root hair cell in 1 mM KCl solution showing (a) topography, (b) the change in DC current between the start and end of the approach, (c) the AC component of the current (feedback setpoint) and (d) the phase of the AC component of the measured current. Scale bars denote 5 µm.

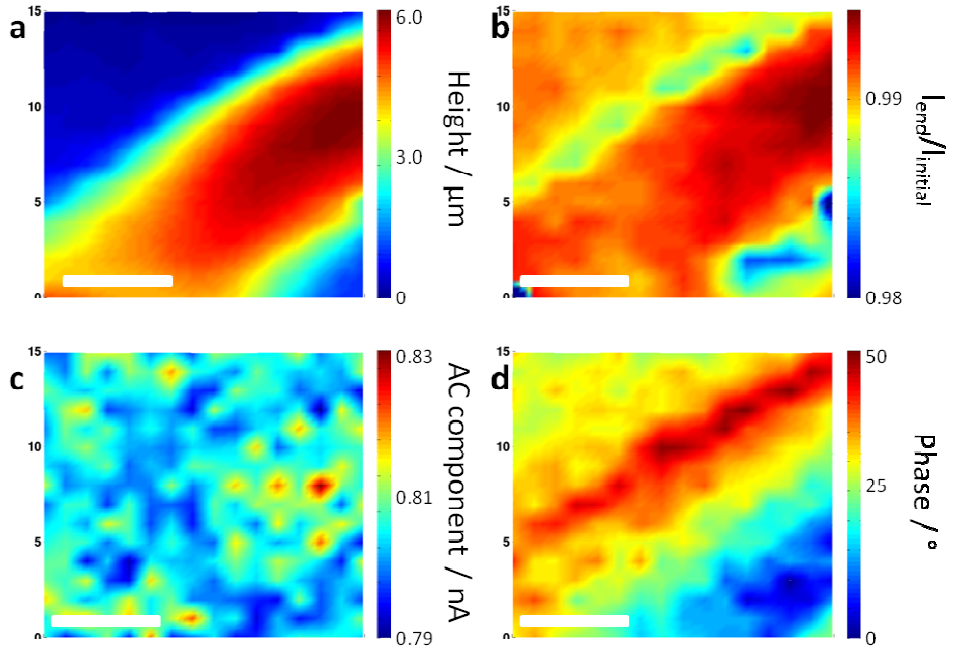

Figure 5.10. SICM imaging of a root hair cell in 100 mM KCl solution showing (a) topography, (b) the change in DC current between the start and end of the approach, (c) the AC component of the current (feedback setpoint) and (d) the phase of the AC component of the measured current. Scale bars denote 5 µm.

Understanding this change is, however, less trivial. Here, the setpoint is the AC component of the migration current, *i.e.* the gradient of the drop in current with separation from the surface. For an SICM approach curve to an inert surface only hindered migration affects the ion current, but changes in local conductivity will affect the shape of this curve. Simply put, lower conductivity close to a surface will make this approach curve steeper and higher conductivity close to a surface will make this curve shallower (unless the increase in local conductivity is sufficiently high to increase the overall current near the surface,

which is unlikely for this system). This will dictate the magnitude of the AC component as function of tip-sample separation.

Figure 5.11 shows two approach curves on (a) the root surface and (b) the support surface in a 10 mM KCl bathing solution. Several observationsare apparent; the current drop to reach the same AC setpoint is considerably larger on the root surface, but this approach curve is less steep and also has a more linear nature. Here, it is clear on the root that the drop in current is much slower than in purely hindered migration, indicating a higher local conductivity near the cell surface. The approach curves for 1 mM KCl and 100 mM KCl are shown in Figures 5.12 and 5.13, respectively. These show a larger drop in the DC component over the root than the surrounding area for 1 mM KCl and a slightly smaller drop over the root for 100 mM, indicating an increase in local conductivity near the root surface at the lower bulk concentration and a (very small) decrease in the loal conductivity near the root surface for the higher concentration.

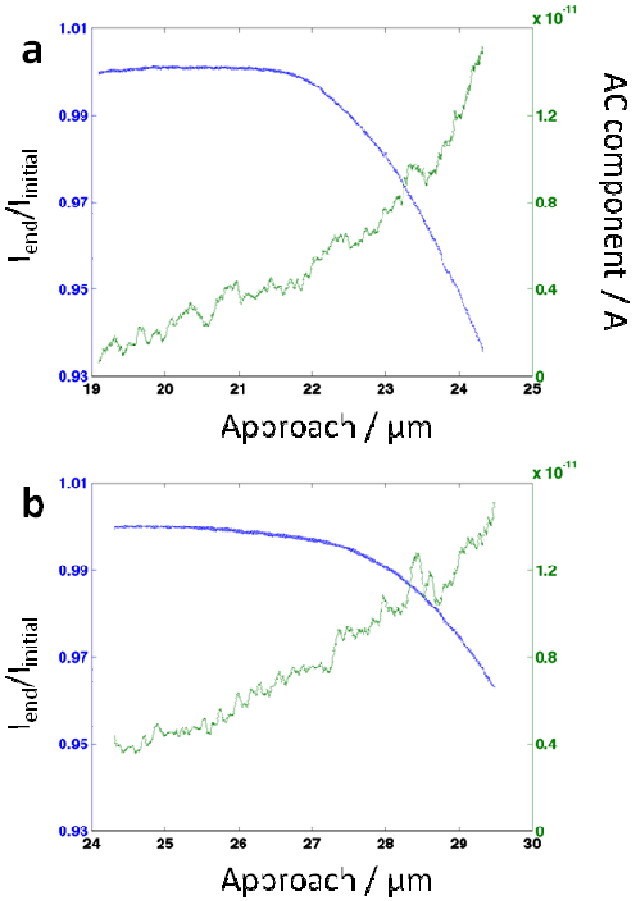

Figure 5.11. Measured migration current as a pipette is approached to the AC setpoint (~1% over a ~100 nm oscillation) towards (a) the root hair cell surface and (b) the support surface. Bathing solution contains 10 mM KCl.

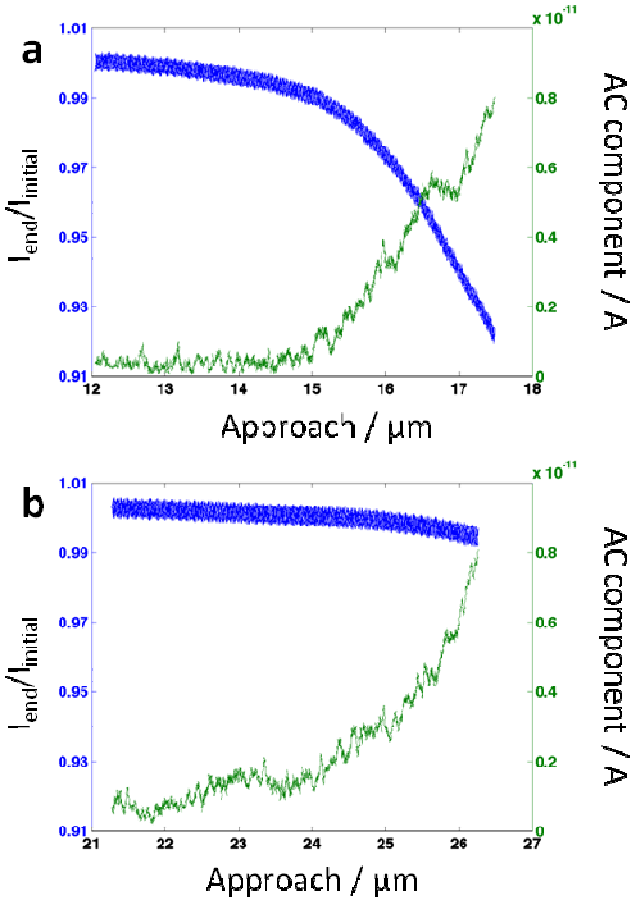

Figure 5.12. Measured migration current as a pipette is approached to the AC setpoint (~1% over a ~100 nm oscillation) towards (a) the root hair cell surface and (b) the support surface. Bathing solution contains 1 mM KCl.

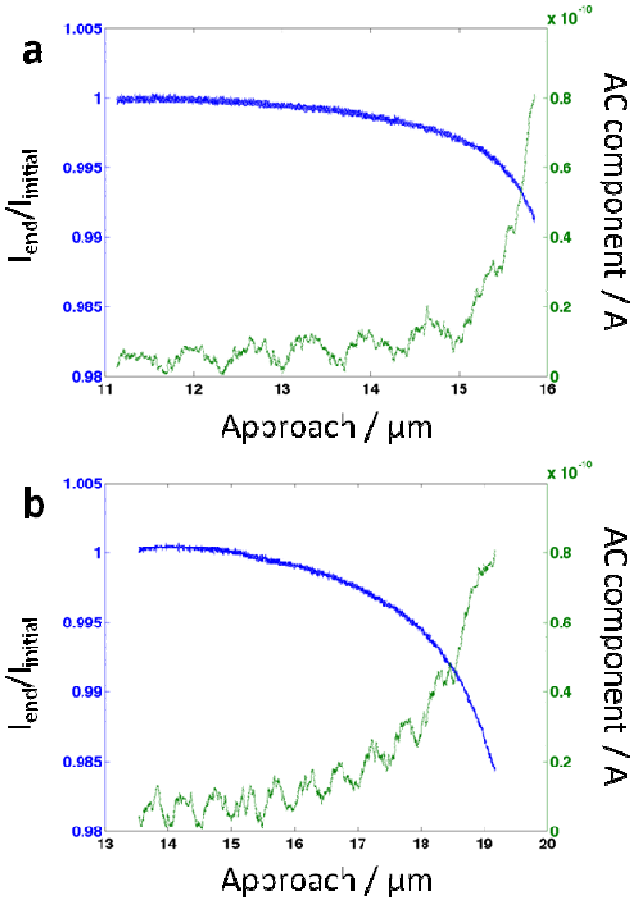

Figure 5.11. Measured migration current as a pipette is approached to the AC setpoint (~1% over a ~100 nm oscillation) towards (a) the root hair cell surface and (b) the support surface. Bathing solution contains 100 mM KCl.

This logically raises the question of whether the AC or a DC setpoint is more appropriate for SICM imaging. The DC component would also be affected by a change in local conductivity, though so there is a change in measured topography between methods (neither of which would be absolutely faithful). It would be possible to do the reverse, maintain a DC setpoint and measure AC

current. Here the magnitude of the AC component would be lower for higher local conductivty near a surface. Future work will involve modelling the apporach curve shapes, together with the cell behaviour, in order to obtain information on both ion fluxes and topography.

This thorough analysis of the technique allows an understanding of the results. The local ion concentration near the root hair cell surface increases in 1 and 10 mM KCl solution, but decreases (slightly) near to the cell surface in 100 mM KCl bathing solution. Though the exact ion content is complex to calculate, it is clear there is an ion efflux from the root at the lower bulk concentrations (1 and 10 mM KCl) and an influx at the higher concentration (100 mM KCl). With further analysis and the development of appropriate models, the solution conductivity, and consequently the ion content, can be determined.

5.4 Conclusions

This chapter has examined the use of various forms of SPM to probe processes related to root cell activity. Initial high resolution root surface analysis was performed using AFM showing localised changes in topography over the root surface. A variety of EC-SPM techniques have been used for the study of processes at root cells and the merits of each method examined. IC-SECM has been used to locally measure enzymatic activity inside the plant root by the

detection of the redox-active species ferrocyanide, formed via reduction of the oxidised from (ferricyanide) inside the plant cells. This technique, however, had limited applicability to such systems due to, firstly, relatively low resolution and, secondly, the large tip-sample interaction force used as an imaging setpoint (which is inherent to this technique). However, it did provide further confirmation that the cells are viable. Secondly, SECCM was used, where a migration (ion) current was measured. It was found to be possible to image individual root hair cells with this technique, however topographical data was unconvincing. Individual approach curves show an extended timescale (>20 s) for the migration current to reach equilibrium on wetting the cell, albeit with an initial very rapid change. The major drawback of this technique being the need for a dry sample, meaning wetting is always a significant factor in conductivity measurements.

The final technique used was SICM, which had the advantage of being both non-contact and performed in a bathing solution, allowing relatively realistic conditions to be used. Here, the root hair cells were imaged in 'hopping' mode using the derivative (AC component) of the ion current as an imaging setpoint with varying bulk KCl concentration. Measured ion currents were dependent on the bulk concentration of the bathing solution, with lower relative currents measured at lower concentrations. Though this may ostensibly suggest a lower local conductivity near the root cell surface, the changing shape of the current / tip-sample separation approach curve affects the measured derivative current. From this a higher relative conductivity near to the root cell was found for bathing concentrations of 1 and 10 mM KCl and a lower relative conductivity near to the cell for the 100 mM KCl bathing solution. Such conclusions indicate

the wealth of information accessible from the SICM technique for such systems but also the non-trivial analysis required in order to further the field.

5.5 References

(1) Amemiya, S.; Guo, J.; Xiong, H.; Gross, D. A. *Analytical and Bioanalytical Chemistry* **2006**, *386*, 458.

(2) Edwards, M. A.; Martin, S.; Whitworth, A. L.; Macpherson, J. V.; Unwin, P. R. *Physiological Measurement* **2006**, *27*, R63.

(3) Roberts, W. S.; Lonsdale, D. J.; Griffiths, J.; Higson, S. P. J. *Biosensors & Bioelectronics* **2007**, *23*, 301.

(4) Stoica, L.; Neugebauer, S.; Schuhmann, W. In *Biosensing for the 21st Century*; Renneberg, R. L. F., Ed. 2008; Vol. 109, p 455.

(5) Anariba, F.; Anh, J. H.; Jung, G.-E.; Cho, N.-J.; Cho, S.-J. *Modern Physics Letters B* **2012**, *26*.

(6) Miragoli, M.; Moshkov, A.; Novak, P.; Shevchuk, A.; Nikolaev, V. O.; El-Hamamsy, I.; Potter, C. M. F.; Wright, P.; Kadir, S. H. S. A.; Lyon, A. R.; Mitchell, J. A.; Chester, A. H.; Klenerman, D.; Lab, M. J.; Korchev, Y. E.; Harding, S. E.; Gorelik, J. *Journal of the Royal Society Interface* **2011**, *8*, 913.

(7) Gorelik, J.; Zhang, Y. J.; Shevchuk, A. I.; Frolenkov, G. I.; Sanchez, D.; Lab, M. J.; Vodyanoy, I.; Edwards, C. R. W.; Klenerman, D.; Korchev, Y. E. *Molecular and Cellular Endocrinology* **2004**, *217*, 101.

(8) Korchev, Y. E.; Gorelik, J.; Lab, M. J.; Sviderskaya, E. V.; Johnston, C. L.; Coombes, C. R.; Vodyanoy, I.; Edwards, C. R. W. *Biophysical Journal* **2000**, *78*, 451.

(9) Korchev, Y. E.; Milovanovic, M.; Bashford, C. L.; Bennett, D. C.; Sviderskaya, E. V.; Vodyanoy, I.; Lab, M. J. *Journal of Microscopy-Oxford* **1997**, *188*, 17.

(10) Zhang, Y. J.; Gorelik, J.; Sanchez, D.; Shevchuk, A.; Lab, M.; Vodyanoy, I.; Klenerman, D.; Edwards, C.; Korchev, Y. *Kidney International* **2005**, *68*, 1071.

(11) Mann, S. A.; Hoffmann, G.; Hengstenberg, A.; Schuhmann, W.; Dietzel, I. D. *Journal of Neuroscience Methods* **2002**, *116*, 113.

(12) Tsionsky, M.; Zhou, J. F.; Amemiya, S.; Fan, F. R. F.; Bard, A. J.; Dryfe, R. A. W. *Analytical Chemistry* **1999**, *71*, 4300.

(13) Yamada, H.; Matsue, T.; Uchida, I. *Biochemical and Biophysical Research Communications* **1991**, *180*, 1330.

(14) Matsue, T.; Shiku, H.; Yamada, H.; Uchida, I. *Journal of Physical Chemistry* **1994**, *98*, 11001.

(15) Macpherson, J. V.; Beeston, M. A.; Unwin, P. R.; Hughes, N. P.; Littlewood, D. *Journal of the Chemical Society-Faraday Transactions* **1995**, *91*, 1407.

(16) Macpherson, J. V.; Beeston, M. A.; Unwin, P. R.; Hughes, N. P.; Littlewood, D. *Langmuir* **1995**, *11*, 3959.

(17) Macpherson, J. V.; Unwin, P. R. *Electroanalysis* **2005**, *17*, 197.

(18) Unwin, P. R.; Macpherson, J. V.; Beeston, M. A.; Evans, N. J.; Littlewood, D.; Hughes, N. P. *Advances in dental research* **1997**, *11*, 548.

(19) McKelvey, K.; Snowden, M. E.; Peruffo, M.; Unwin, P. R. *Analytical Chemistry* **2011**, *83*, 6447.

(20) Pierce, D. T.; Bard, A. J. *Analytical Chemistry* **1993**, *65*, 3598.

(21) Pierce, D. T.; Unwin, P. R.; Bard, A. J. *Analytical Chemistry* **1992**, *64*, 1795.

(22) Kranz, C.; Lotzbeyer, T.; Schmidt, H. L.; Schuhmann, W. *Biosensors & Bioelectronics* **1997**, *12*, 257.

(23) Wittstock, G.; Schuhmann, W. *Analytical Chemistry* **1997**, *69*, 5059.

(24) Wijayawardhana, C. A.; Wittstock, G.; Halsall, H. B.; Heineman, W. R. *Analytical Chemistry* **2000**, *72*, 333.

(25) Shiku, H.; Takeda, T.; Yamada, H.; Matsue, T.; Uchida, I. *Analytical Chemistry* **1995**, *67*, 312.

(26) Zhou, H. F.; Kasai, S.; Yasukawa, T.; Matsue, T. *Electrochemistry* **1999**, *67*, 1135.

(27) Yasukawa, T.; Kanaya, N.; Mandler, D.; Matsue, T. *Chemistry Letters* **2000**, 458.

(28) Lee, C. M.; Kwak, J. Y.; Bard, A. J. *Proceedings of the National Academy of Sciences of the United States of America* **1990**, *87*, 1740.

(29) Tsionsky, M.; Cardon, Z. G.; Bard, A. J.; Jackson, R. B. *Plant Physiology* **1997**, *113*, 895.

(30) Zhu, R. K.; Macfie, S. M.; Ding, Z. F. *Journal of Experimental Botany* **2005**, *56*, 2831.

(31) Kaya, T.; Nishizawa, M.; Yasukawa, T.; Nishiguchi, M.; Onouchi, T.; Matsue, T. *Biotechnology and Bioengineering* **2001**, *76*, 391.

(32) Yasukawa, T.; Kaya, T.; Matsue, T. *Analytical Chemistry* **1999**, *71*, 4637.

(33) Yasukawa, T.; Kaya, T.; Matsue, T. *Electroanalysis* **2000**, *12*, 653.

(34) Yasukawa, T.; Kaya, T.; Matsue, T. *Chemistry Letters* **1999**, 975.

(35) Kaya, T.; Torisawa, Y. S.; Oyamatsu, D.; Nishizawa, M.; Matsue, T. *Biosensors & Bioelectronics* **2003**, *18*, 1379.

(36) Kaya, T.; Numai, D.; Nagamine, K.; Aoyagi, S.; Shiku, H.; Matsue, T. *Analyst* **2004**, *129*, 529.

(37) Torisawa, Y. S.; Kaya, T.; Takii, Y.; Oyamatsu, D.; Nishizawa, M.; Matsue, T. *Analytical Chemistry* **2003**, *75*, 2154.

(38) Holt, K. B.; Bard, A. J. *Biochemistry* **2005**, *44*, 13214.

(39) Nagamine, K.; Kaya, T.; Yasukawa, T.; Shiku, H.; Matsue, T. *Sensors and Actuators B-Chemical* **2005**, *108*, 676.

(40) Nagamine, K.; Matsui, N.; Kaya, T.; Yasukawa, T.; Shiku, H.; Nakayama, T.; Nishino, T.; Matsue, T. *Biosensors & Bioelectronics* **2005**, *21*, 145.

(41) Novak, P.; Li, C.; Shevchuk, A. I.; Stepanyan, R.; Caldwell, M.; Hughes, S.; Smart, T. G.; Gorelik, J.; Ostanin, V. P.; Lab, M. J.; Moss, G. W. J.; Frolenkov, G. I.; Klenerman, D.; Korchev, Y. E. *Nature Methods* **2009**, *6*, 279.

(42) Adler, J.; Shevchuk, A. I.; Novak, P.; Korchev, Y. E.; Parmryd, I. *Nature Methods* **2010**, *7*, 170.

(43) Takahashi, Y.; Murakami, Y.; Nagamine, K.; Shiku, H.; Aoyagi, S.; Yasukawa, T.; Kanzaki, M.; Matsue, T. *Physical Chemistry Chemical Physics* **2010**, *12*, 10012.

(44) Liu, X.; Yang, X.; Zhang, B.; Zhang, X.; Lu, H.; Zhang, J.; Zhang, Y. *Brain Research* **2011**, *1386*, 35.

(45) Shevchuk, A. I.; Gorelik, J.; Harding, S. E.; Lab, M. J.; Klenerman, D.; Korchev, Y. E. *Biophysical Journal* **2001**, *81*, 1759.

(46) Lyon, A. R.; MacLeod, K. T.; Zhang, Y.; Garcia, E.; Kanda, G. K.; Lab, M. J.; Korchev, Y. E.; Harding, S. E.; Gorelik, J. *Proceedings of the National Academy of Sciences of the United States of America* **2009**, *106*, 6854.

(47) Gorelik, J.; Ali, N. N.; Shevchuk, A. I.; Lab, M.; Williamson, C.; Harding, S. E.; Korchev, Y. E. *Tissue Engineering* **2006**, *12*, 657.

(48) Gorelik, J.; Yang, L. Q.; Zhang, Y.; Lab, M.; Korchev, Y.; Harding, S. E. *Cardiovascular Research* **2006**, *72*, 422.

(49) Li, C.; Johnson, N.; Ostanin, V.; Shevchuk, A.; Ying, L.; Korchev, Y.; Klenerman, D. *Progress in Natural Science-Materials International* **2008**, *18*, 671.

(50) Shevchuk, A. I.; Frolenkov, G. I.; Sanchez, D.; James, P. S.; Freedman, N.; Lab, M. J.; Jones, R.; Klenerman, D.; Korchev, Y. E. *Angewandte Chemie-International Edition* **2006**, *45*, 2212.

(51) Korchev, Y. E.; Negulyaev, Y. A.; Edwards, C. R. W.; Vodyanoy, I.; Lab, M. J. *Nature Cell Biology* **2000**, *2*, 616.

(52) Takahashi, Y.; Shevchuk, A. I.; Novak, P.; Murakami, Y.; Shiku, H.; Korchev, Y. E.; Matsue, T. *Journal of the American Chemical Society* **2010**, *132*, 10118.

(53) Takahashi, Y.; Shevchuk, A. I.; Novak, P.; Zhang, Y.; Ebejer, N.; Macpherson, J. V.; Unwin, P. R.; Pollard, A. J.; Roy, D.; Clifford, C. A.; Shiku,

H.; Matsue, T.; Klenerman, D.; Korchev, Y. E. *Angewandte Chemie (International ed. in English)* **2011**, *50*, 9638.

(54) Levin, M. *Trends in Cell Biology* **2007**, *17*, 261.

(55) Magistretti, P. J.; Pellerin, L. *Philosophical Transactions of the Royal Society of London Series B-Biological Sciences* **1999**, *354*, 1155.

(56) Newman, I. A. *Plant Cell and Environment* **2001**, *24*, 1.

(57) Sather, W. A.; McCleskey, E. W. *Annual Review of Physiology* **2003**, *65*, 133.

(58) Gorelik, J.; Gu, Y. C.; Spohr, H. A.; Shevchuk, A. I.; Lab, M. J.; Harding, S. E.; Edwards, C. R. W.; Whitaker, M.; Moss, G. W. J.; Benton, D. C. H.; Sanchez, D.; Darszon, A.; Vodyanoy, I.; Klenerman, D.; Korchev, Y. E. *Biophysical Journal* **2002**, *83*, 3296.

(59) Wei, C.; Bard, A. J.; Nagy, G.; Toth, K. *Analytical Chemistry* **1995**, *67*, 1346.

(60) Ying, L. M.; White, S. S.; Bruckbauer, A.; Meadows, L.; Korchev, Y. E.; Klenerman, D. *Biophysical Journal* **2004**, *86*, 1018.

(61) Edwards, M. A.; Williams, C. G.; Whitworth, A. L.; Unwin, P. R. *Analytical Chemistry* **2009**, *81*, 4482.

(62) Hepler, P. K.; Vidali, L.; Cheung, A. Y. *Annual Review of Cell and Developmental Biology* **2001**, *17*, 159.

(63) Kaplan, J. H. *Annual Review of Biochemistry* **2002**, *71*, 511.

(64) Luo, C. H.; Rudy, Y. *Circulation Research* **1994**, *74*, 1071.

(65) Pena, M. M. O.; Lee, J.; Thiele, D. J. *Journal of Nutrition* **1999**, *129*, 1251.

(66) Tani, M.; Neely, J. R. *Circulation Research* **1989**, *65*, 1045.

(67) Widholm, J. M. *Stain Technology* **1972**, *47*, 189.

6. Conclusions

This thesis concerned the development and application of modern and expanding technologies to processes related to the agrochemical industry, *i.e.* the study of physicochemical processes involving plants and their environment. The focus has been to study these processes both locally at high resolution and at appropriate timescales for the various systems studied. Both mimetic and live biological systems have been studied. One particular focus has been that of bioadhesion, measurement of rates and mechanisms of binding to both plant matter and that of the immediate environment. Further to this, high resolution characterisation methods for the plant cell surface have been employed towards the study of dynamic cellular processes.

Chapter 3 concerned the application of a modern high-resolution condensed phase spectroscopic technique, evanescent wave-cavity ringdown spectroscopy (EW-CRDS), to measure adsorption kinetics of chemically-functionalised polymeric molecules to a range of functionalised surfaces. The surfaces studied were functionalised to represent the outer plant cell surface and the inorganic and organic fractions of soil using cellulose, silica and poly-L-glutamic acid respectively. Adsorption was found to be characteristic for each polymer, and kinetic rate constants were extracted for the initial part of the adsorption processes allowing a relative assessment of the adhesion rates between each macromolecule and surface.

To further examine EW-CRDS as a probe of biomimetic surfaces, a system was developed for the following of formation and adhesion to supported lipid bilayers (SLBs), used commonly as a model for cell membranes. The system consisted of an impinging jet flow cell coupled to the EW-CRD spectrometer allowing both easy change of solution and delivery in a controlled manner. A cationic lipid (DOTAP) was chosen for SLB formation on the silica prism surface and the adsorption kinetics of a anionic porphyrin molecule (TPPS) measured, underlining the applicability of the EW-CRDS technique to such studies.

Chapter 4 extended these adsorption studies to involve charged microparticles. For particles of this size, confocal laser scanning microscopy (CLSM) was selected as an appropriate tool to quantify adsorption rates of particles of this size. Rates of adsorption of anionic particles were measured to a range of mimetic surface, including cellulose and positively and negatively charged surfaces, formed by deposition of poly-L-lysine and poly-L-glutamic acid thin films onto glass surfaces. These studies were extended via coupling with a similar impinging jet system to previous studies with the CLSM, allowing elucidation of a kinetic rate constant for the smaller particles. In order to reduce the scale of studies to that of a single root hair cell, a microscale vertical flow cell was developed, based upon a theta capillary and utilising the migration of charged species as a means of delivery. This delivery system was initially trialled on charged surfaces and the system modelled using finite element method modelling to explain adsorption rates and manner. Finally this

system was used to deliver charged particles and polymer molecules to individual root hair cell surfaces.

In chapter 5, electrochemical scanned probe microscopy (EC-SPM) techniques were employed to study the root cell surface, primarily the surface of the root hair cells of the *Zea mays* plant. Following AFM imaging of detached root hair cell surfaces, a range of EC-SPM techniques were used. Intermittent contact-scanning electrochemical microscopy (IC-SECM) was used for detection of ferrocyanide generated inside the plant cells. Here, due to the large tip-sample interaction forces inherent to the technique, the upper surface of the entire plant root was imaged showing localised heterogeneities. This technique was, however, too destructive for single cell, high resolution imaging. The second technique used was scanning electrochemical cell microscopy (SECCM). This technique showed changes in conductivity over individual root hair cells but artefacts due to wetting were seen to dominate the measured current. The final and most successful technique employed was scanning ion conductance microscopy (SICM). This technique is non-contact and immerses the entire sample in a bathing solution. Careful interpretation of approach curve data enabled analysis of changes in local conductivity at the cell surface as a function of bathing solution ion concentration. This technique was found to be the most useful for future study of dynamic processes at similar cell surfaces.

In summary, this thesis applied a number of new and developing techniques to processes related to the agrochemical industry. EW-CRDS

provided a fast and accurate method to study adsorption kinetics of various species to a wide range of model surfaces, encompassing the first studies on polymer molecule adsorption with this technique and the *in situ* study of adsorption to dynamic SLBs. The next studies involved measurement of particle adsorption to similar surfaces, evolving to combination with various delivery systems, including the development of a new migratory flow cell technique. Finally, cutting-edge EC-SPM techniques were used for the study of root cell surfaces, with SICM found to be the most useful of these. With careful analysis of approach curve data when operated in a 'hopping' mode, it was possible to both image cell surfaces and extract localised conductivity information related to ion exchange between the cell and surrounding environment.